SCATTERING AND NONLINEAR TRANSFORMATIONS OF INTERNAL TIDE BEAMS

A DISSERTATION SUBMITTED TO THE GRADUATE DIVISION OF THE UNIVERSITY OF HAWAIʻI AT MĀNOA IN PARTIAL FULFILLMENT OF THE REQUIREMENTS FOR THE DEGREE OF

DOCTOR OF PHILOSOPHY

IN

OCEANOGRAPHY

MAY 2020

By

Sherry H. Chou

Dissertation Committee:

Glenn S. Carter, Chairperson
Douglas S. Luther
Mark A. Merrifield
Brian S. Powell
Chantal Staquet
Eva-Marie Nosal

© 2020

Sherry H. Chou

This work is licensed under a Creative Commons BY-NC-SA License.

"The cure for anything is salt water – sweat, tears, or the sea." – Isak Dinesen (via Readers Digest 1934)

0.1 Acknowledgements

This work was partially funded by the National Science Foundation (grant #1538427), the Chateaubriand Fellowship, and the Denise B. Evans Fellowship in Oceanographic Research.

I would like to thank my entire committee for their continual encouragement and support. I would like to especially thank Glenn for his patient and thoughtful guidance, and for demonstrating the open mindedness, persistence, and curiosity that represent to me the most admirable scientific spirit.

I would also like to thank Eric Firing and Nicolas Grisouard for their invaluable contributions to this work. Mahalo nui loa to the entire Oceanography office staff, especially Catalpa Kong and Kristin Uyemura, who have always gone above and beyond to be helpful and supportive. Many thanks to Margaret McManus and Niklas Schneider for their understanding, assistance, and encouragement.

Special thanks to Barb Bruno for being an amazing mentor - for supporting and encouraging me in so many ways.

Last but not least, thank you to all the friends and family who have made everything possible, and who make everything worthwhile.

0.2 Abstract

The fate of internal tides as they propagate in non-uniform stratification is studied using two different numerical models, a linear and inviscid modes model (LIMM) and the nonlinear Massachusetts Institute of Technology general circulation model (MITgcm). As an internal tide beam propagates through varying density stratification, wave energy can be scattered through linear processes such as internal reflection and refraction. Scattering can lead to the splitting of beams so that the energy density of individual beams is decreased. Beam scattering can also cause horizontal ducting, or partial vertical confinement, of internal tide energy in the pycnocline and mixed layer. Two different beam scattering regimes are identified through LIMM experiments, and a non-dimensional parameter predicting the amount of internal reflection that occurs due to changing stratification is proposed.

Kinetic energy from internal tide beams can also be transferred to non-tidal frequencies and vertical scales through the nonlinear generation of internal solitary waves, higher harmonics, and, depending on latitude, triadic resonant interactions. We find that interfacial waves in the pycnocline can be generated for a range of latitudes with stratification representative of the Bay of Biscay, but not with a profile representative of Hawaii. The Bay of Biscay experiments also show more horizontal ducting of energy in the pycnocline, for all frequencies. Both sets of experiments show transfers of energy to subharmonic frequencies and small vertical scales that suggest the presence of triadic resonant interactions. At latitudes where triadic resonant interactions are most active, energy transferred to subharmonic secondary waves can grow with time until it becomes greater than the energy remaining at the forcing frequency. For the Bay of Biscay experiments, degradation of the tidal beam due to triadic resonant interactions can interfere with the generation of interfacial waves in the pycnocline.

Table of Contents

0.1 Acknowledgements v

0.2 Abstract vii

List of Tables . . . . . **x**

List of Figures . . . . . **xii**

1 Introduction **1**

1.1 Background 2

1.2 Summary 4

2 Scattering of internal tide beam energy due to non-uniform density stratification **5**

2.1 Introduction 5

2.2 Methods 7

2.3 Scattering due to piece-wise N^2 profile 11

2.4 Scattering due to Gaussian N^2 profiles 14

2.5 Summary and Discussion 38

3 Latitude dependence of the fate of internal tide beams **41**

3.1 Introduction 41

3.2 Methods 45

3.3 Bay of Biscay stratification experiments 49

3.4 Hawaii stratification (HOT) experiments 63

3.5 Quantifying nonlinear energy transfers 67

3.6 Summary and Discussion 73

4 Conclusion **78**

Bibliography **83**

List of Tables

2.1 Information about the piece-wise N^2 profile experiments, for comparison with Gerkema (2001). Ducting refers to partial vertical confinement of energy. The regime $\mathscr{R}_j$ is related to the PS_1 and ε parameters. 13

2.2 Information about Gaussian N^2 profile experiments, for comparison with experiments from Table 2.1. The regime $\mathscr{R}_j$ is related to the PS_2 and σ parameters. 21

2.3 Behavior of internal tide beams passing through non-uniform stratification can be categorized into four different regimes, based on the PS_2 and σ parameters. 21

2.4 Parameters for Gaussian stratification experiments are listed. The type of scattering (Regimes $\mathscr{R}_2$ or $\mathscr{R}_4$) is related to $PS_2 = 2A_N\sigma$, but not to z_{pyc}. The transition between Regimes $\mathscr{R}_2$ and $\mathscr{R}_4$ occurs roughly around $PS_2 = 0.01\,\mathrm{m\,s^{-2}}$, with smaller values indicating Regime $\mathscr{R}_2$ and larger values indicating Regime $\mathscr{R}_4$. 25

2.5 Parameters for Gaussian stratification experiments in Regime $\mathscr{R}_4$ are listed. The number of modes used in calculations range from 125 (for $b_{scale} = 400$) to 300 (for $b_{scale} = 150$). PR stands for percent reflection. Q is the parameter described in the text, rounded to 2 significant digits; it has the strongest predictive power for percent reflection when compared to other parameters listed in the table. $N_{min} = 2\times10^{-3}s^{-1}$ except for the v2* experiments where $N_{min} = 1\times10^{-3}s^{-1}$. 36

3.1 Experiments are named by the stratification profile used (BB for Bay of Biscay, and HOT for Station ALOHA) and their approximate latitude; f is the Coriolis frequency, and t_s is the time it takes the forcing beam to reach the surface, in units of $T_0 = 2\pi/\omega_0$, the wave period of M_2. Two time intervals are specified, R_1: $3t_s$ to $3t_s + 10\,T_0$, and R_2: $3t_s + 15\,T_0$ to $3t_s + 25\,T_0$ (times are rounded down to the nearest integer multiple of T_0). 47

3.2 The ratio of M_2 subharmonic energy to M_2 energy (SER) during R_1 and R_2 (two rightmost columns). The first column lists the approximate latitude of the experiment, the second lists the local inertial frequency f normalized by ω_0, the third lists the frequency that has the highest PSD during R_2 (sometimes it is different during R_1), and the fourth lists the stratification profile that is used. 75

List of Figures

2.1 Stratification of Experiment E6 (a) is shown with the u-velocity profile of the beam (b) and the associated vertical mode amplitudes A_m (c). The beam velocity is projected onto modes that are based on the stratification profile to get the mode amplitudes. The analytical form of the beam is plotted in black, and the reconstructed beam as a sum of (20) modes is plotted in red (the two are almost identical here). 10

2.2 Figure 2 from Gerkema (2001) shows the set-up of his analytical *2c-layer model*. The stratification consists of an unstratified top layer of thickness d ($N^2 = 0$), a pycnocline layer of thickness ε and $N^2 = g'/\varepsilon$, and a lower layer with constant stratification ($N_c^2 = 4\times10^{-6}\,\mathrm{s}^{-2}$). H is the total water depth. 12

2.3 Horizontal u-velocity (full domain) for piece-wise N^2 experiments: E1 - the absent pycnocline case (Regime $\mathscr{R}_1$), E2 - the strong pycnocline case (Regime $\mathscr{R}_3$), and E3 - the moderate pycnocline case (Regime $\mathscr{R}_2$). 15

2.4 Horizontal u-velocity (upper 1 km) for piece-wise N^2 experiments: E2 - the strong pycnocline case (Regime $\mathscr{R}_3$), E3 - moderate pycnocline case (Regime $\mathscr{R}_2$), and E5 - the pycnocline ducting case (Regime $\mathscr{R}_4$). 16

2.5 Stratification profiles for experiments E6 and hE6 (a) are plotted together for comparison. The first three vertical modes calculated with the E6 and hE6 profiles are shown in b) and c), respectively. The vertical axis of a) is for the top 20-120 m while the axes for b) and c) are for the full depth of 4 km. Green dashed lines at $z_{pyc} \pm \sigma$ indicate the boundaries for the vertical integral represented by PS_2, where σ is a defining parameter for the Gaussian stratification profile. 18

2.6 Horizontal u-velocity (full domain) for Gaussian N^2 experiments: hE1 - the absent pycnocline case (Regime $\mathscr{R}_1$), hE2 - the strong pycnocline case (Regime $\mathscr{R}_3$), and hE3 - the moderate pycnocline case (Regime $\mathscr{R}_2$). 19

2.7 Horizontal u-velocity (upper 1 km) for Gaussian N^2 experiments: hE2 - the strong pycnocline case (Regime $\mathscr{R}_3$), hE3 - moderate pycnocline case (Regime $\mathscr{R}_2$), and hE5 - the pycnocline ducting case (Regime $\mathscr{R}_4$). 20

2.8 The u-velocity (top) and $HIF_n(x, z_i = 1.5\,\text{km})$ (bottom) for the HOT profile experiment. The internal tide beam propagates though the pycnocline and reflects off the top and bottom boundaries without losing much energy to scattering. The HIF curve shows that almost all of the upward energy flux is balanced by downward energy flux between $x = 0$ and 125 km. 23

2.9 Stratification N^2 profiles for various experiments are shown together for comparison of their vertical integrals (areas under the N^2 curve). The PS_2 parameter is an (under)estimate of the area under the N^2 curve, and is related to the type and amount of scattering. 24

2.10 Two experiments are run with the G1 stratification profile for different sized domains: a) H = 4 km and b) H = 40 km. In the deep domain simulation, bottom reflection occurs far from the surface reflection and the upward and downward beams do not meet in the region shown. 26

2.11 Stratification information (left panel), u-velocity (top and bottom right panels), and associated HIF curve (middle right panel) for Experiment G1. The N^2 profile G (blue) and its second derivative G_{zz} (red, not to scale) are shown in the left panel with horizontal dashed lines indicating z_{pyc} (black), +/- σ distance from z_{pyc} (green), and +/- $\sqrt{3}\sigma$ from z_{pyc} (magenta). The distance σ is shown since it is a key parameter describing the shape of the Gaussian function. The $HIF_n(x, z_i)$ plot can be used to estimate the amount of energy flux passing a certain depth z_i (2 km in this case) - the red dashed line indicates the amount of energy (normalized so that the maximum is 1) remaining above z_i after 600 km. 28

2.12 Same as Figure 2.11 except it is for Experiment G2. 29

2.13 Same as Figure 2.11 except it is for Experiment G4. 30

2.14 Same as Figure 2.11 except it is for Experiment G7. 31

2.15 Same as Figure 2.11 except it is for Experiment G12. 32

2.16 Same as Figure 2.11 except it is for Experiment G11. 34

2.17 Same as Figure 2.11 except it is for Experiment G20. 37

2.18 Snapshots of horizontal velocity [ms^{-1}] for two MITgcm experiments which are identical except for vertical resolution. Upper panel shows spurious scattering of a reflected beam due to insufficient vertical resolution ($dz = 20$ m), and the lower panel shows a simulation with $dz = 5$ m which agrees with output from an analytical model with $dz = 2$ m. 40

3.1 Wave vector diagram for TRI. The red vector represents the primary wave, and the green and blue vectors represent the secondary waves. The vertical wavenumber is m, and the horizontal wavenumber is k_x. 43

3.2 Buoyancy frequency $N(z)$ for the experiments in this study are based on density stratification profiles that are representative of a) the Bay of Biscay at 45°N and b) Hawaii at 22.75°N. Inset shows both stratification profiles down to 500 m depth. 45

3.3 Snapshots of isopycnals and u-velocity (the color scale ranges from -0.12 to 0.12 m s^{-1}) are shown for two different times: $5\,t_s$ (left column) and $10\,t_s$ (right column), and three different latitudes: 45°N (top two rows), 29°N (middle two rows), and 15°N (bottom two rows). 50

3.4 Same as Figure 3.3 except data is for latitudes 50°N (top two rows), 55°N (middle two rows), and 60°N (bottom two rows). 51

3.5 Displacement of the pycnocline for six different latitudes. The color scale ranges from -20 m to 20 m (blue is negative, red is positive). Note that the time axis for the different latitudes do not all start at the same value (with respect to T_0) but they all span a duration of 25 T_0. Time ranges from $3t_s$ to $3t_s$ + 25 T_0. The green boxes each span a duration of 10 T_0 (R_1 and R_2), and are separated by 5 T_0 (see Table 3.1 for details about t_s, R_1 and R_2). 53

3.6 Isopycnals at the pycnocline are plotted as a function of distance and time for 3 different latitudes. Left panels show the first 3 wave periods of R_1, and right panels show the first 3 wave periods of R_2. The blue and red lines trace example waves associated with the ITB impinging on the pycnocline from below and with higher-frequency interfacial waves, respectively. 55

3.7 Same as Figure 3.6 except data is for latitudes 50°N, 55°N, and 60°N. There are no lines for the interfacial waves at 60°N because they are not identifiable in this plot. . 56

3.8 The PSD of u-velocity (averaged from 46-70 m depth) for 4 different latitudes (5-29°N) are shown for time periods R_1 and R_2. The color scale is the same for all plots, and the frequencies range from 0 to 10 ω_0. The small vertical arrows indicate the x-locations of the ITB surface reflection. Horizontal green dashed lines indicate the Coriolis frequency $\omega = f$, and the blue lines indicate $\omega = \omega_0$-f. 57

3.9 Same as Figure 3.8 except data is for latitudes 35-55°N. 58

3.10 The PSD of u-velocities for the time periods R_1 (left panels) and R_2 (right panels). At each latitude the PSDs are normalized by the maximum PSD at ω_0 for R_1. The frequencies are noted in the lower left corner. Note that the color scale is not the same for all plots. Internal wave characteristics are plotted in green. 60

3.11 The PSD of u-velocity for R_2 at four discrete frequencies. At each latitude the PSD is normalized by the maximum PSD (of any frequency) for R_2 (the maximum for 35°N occurs for ω_0, not shown). The frequencies are noted in the lower left corner. Note that the color scale is not the same for all plots. Internal wave characteristics are plotted in green. 61

3.12 Left column: u-velocity (WKB stretched) averaged from 20-25 km in the x direction as a function of time. Right column: associated vertical wavenumber spectra as a function of time. The small black arrows point to the wavenumber of the forcing beam. 62

3.13 Same as Figure 3.3 except the stratification is from HOT (pycnocline is at 72 m depth). 64

3.14 Same as Figure 3.5 except the stratification is from HOT, and 55°N is replaced by 50°N. 65

3.15 Same as Figure 3.6 except the stratification is from HOT and the density is for 74 m depth. Here the red lines trace example waves associated with the ITB impinging on the pycnocline from below. There are no indications of propagating interfacial waves. 66

3.16 Same as Figure 3.8 except here the stratification is from HOT, and 5°N is replaced by 20°N. Velocity is averaged from 62-82 m depth. 68

3.17 Same as Figure 3.9 except here the stratification is from HOT, and 55°N is replaced by 40°N. 69

3.18 Same as Figure 3.10 except here the stratification is from HOT. 70

3.19 Same as Figure 3.11 except here the stratification is from HOT. 71

3.20 Same as Figure 3.12 except here the stratification is from HOT and the u-velocity is averaged from 40-45 km. 72

3.21 Indices representing energy in different frequency bands, for $\boldsymbol{R}_1$ and $\boldsymbol{R}_2$ and different latitudes (top three rows). Details about these indices are given in the text. The fourth row shows the Subharmonic Energy Ratio (SER). Note that there are no data at 55°N and 60°N for HOT experiments. 74

CHAPTER 1

Introduction

Internal waves are ubiquitous in the ocean and their breaking can lead to the turbulent mixing of water of different densities. It is thought that the strength and location of this diapycnal mixing has an important impact on the meridional overturning circulation (Munk & Wunsch, 1998, Wunsch & Ferrari, 2004, Ferrari et al., 2016), which in turn affects regional and global climate. Munk (1966) used a simple diffusion-advection model to estimate that a uniform diapycnal diffusivity value of $\kappa = 10^{-4}\,\mathrm{m^2s^{-1}}$ associated with mixing could balance deep water formation of $30 \times 10^6\,\mathrm{m^3s^{-1}}$ at high latitudes to maintain global stratification, which is essential for the meridional overturning circulation. However, observations have shown that diffusivity values of $10^{-5}\,\mathrm{m^2s^{-1}}$ were most common in the open ocean away from topography (Gregg, 1987, Ledwell et al., 1993). A revised theory is that the uniform value of diffusivity is equivalent to a generally weak average value and some locations of strong diffusivity (Munk & Wunsch, 1998).

It is estimated that approximately 2 terawatts (TW) are needed to power the meridional overturning circulation (Munk & Wunsch, 1998) and up to 1 TW can be supplied by internal waves at tidal frequencies, or internal tides (Egbert & Ray, 2000, 2001). Internal tides are believed to be the strongest contributor to the internal wave spectrum and the most important process for deep-ocean mixing (MacKinnon et al., 2017). A large set of observations studied by Waterhouse et al. (2014)

shows that turbulent dissipation rates are bottom intensified over rough topography and mid-ocean ridges, and the correlation between integrated dissipation rates and internal tide sources dominate over wind power sources in all but one dataset (MacKinnon et al., 2017). While the mechanism and location of the generation of internal tides are well understood and there is a growing dataset of mixing estimates, it is still not clear where internal tides dissipate most of their energy (MacKinnon et al., 2013b, Zhao et al., 2016). Ultimately, it is important to know how much internal tide energy makes it down to the deep ocean in order to estimate how much of their energy is available for abyssal mixing.

1.1 Background

Internal waves in the ocean are studied for many reasons. They represent a large portion of observed variability in the ocean and they are important for applied problems (such as the dispersion of chemical tracers and the transmission of sound) as well as for dynamical understanding of energetics and circulation in the ocean (Müller et al., 1986). Internal tides are internal waves generated in stratified waters by the flow of barotropic tides over variable topography (Garrett & Kunze, 2007). The resulting internal tide energy is initally confined in vertically limited structures, or beams, that can be described as a superposition of vertical modes. Well away from the generation site the internal tide energy has been observed to be primarily in low modes (Dushaw et al., 1995, Ray & Mitchum, 1996, Rainville et al., 2010). As internal tide beams propagate through regions of non-uniform stratification in the upper ocean, wave energy can be scattered through multiple reflections and refractions, horizontally ducted, or transferred to non-tidal frequencies and smaller vertical scales through nonlinear processes. The decay and dissipation of internal tides can lead to diapycnal mixing (of heat, momentum, gasses, and nutrients) which plays a key role in biogeochemical, ecological, and physical oceanic processes as well as the coupled ocean-atmosphere climate system (Wunsch & Ferrari, 2004).

At the Mendocino Escarpment (located west of Cape Mendocino in California), radiated internal

tide energy flux is reduced by more than 50% after the surface reflection (Althaus et al., 2003), but it is not clear what is responsible for this rapid decrease. A number of processes can lead to the transfer of internal tide beam energy in wavenumber and frequency space. Energy can be lost from M_2 internal tide beams in the pycnocline due to the local generation of solitary waves (Xie et al., 2013b), wave-wave interactions with subharmonics or higher harmonics (Xie et al., 2013a), or to induced mean flows (Cole et al., 2009). Observations indicate increased nonlinearity in the pycnocline (Lee et al., 2006) and correlation between turbulent kinetic energy dissipation and internal solitary waves (Carter et al., 2005, Xie et al., 2013b).

In general, direct field observations of internal tide beams are rare (Gerkema & van Haren, 2012). The Kauai Channel in Hawaii is unique in that it has been a site for extensive field observations for the Hawaii Ocean Mixing Experiment (Pinkel & Rudnick, 2006) and various other field programs such as the Hawaii Ocean Time-series (Karl & Lukas, 1996). One of the most spatially comprehensive views of internal tide beams, from generation to surface reflection and beyond, comes from Shipboard Acoustic Doppler Current Profiler (SADCP) observations over Kaena ridge (Pickering & Alford, 2012). These observations show internal tide beam decay (i.e., disintegration of beam structure) "downstream" of surface reflection and suggest that kinetic energy of internal tide beams is being transferred to other motions and possibly partly dissipated. Little is currently known about the processes that cause internal tide beams to lose their structure after surface reflection or about the energetics associated with these processes, which impedes estimating the amount of energy available for abyssal diapycnal mixing.

An evaluation of the tidal energy budget around Hawaii (Zaron & Egbert, 2014) reveals a gap of 7-11 gigawatts (GW) between the production of internal tides by the barotropic tide (18-25 GW) and the sum of near-field dissipation (as measured by microstructure profilers) and far-field radiation (as estimated by satellite observations of coherent tides). More than 50% of internal tide energy could be unaccounted for by this estimate, suggesting that there are important energy pathways that are not being considered. A better quantitative understanding of how much energy can be re-distributed or lost from internal tide beams as they reflect from the surface of the ocean and how the strength

of these energy transfers depends on varying environmental conditions is needed.

1.2 Summary

Observational evidence (Althaus et al., 2003, Martin et al., 2006, Pickering & Alford, 2012) indicates that internal tide beams weaken after reflection near the ocean surface, raising many questions about the energy pathways of internal tides in the upper ocean. Laboratory (Mathur & Peacock, 2009, Mercier et al., 2012) and idealized numerical model (Gerkema, 2001, Gerkema & van Haren, 2012) studies have suggested that internal tide beams may lose energy in the upper (< 1 km) ocean due to a variety of processes. Using two numerical models, the Massachusetts Institute of Technology general circulation model (MITgcm) (Marshall et al., 1997) and a linear vertical modes model (LIMM) developed at the University of Hawaii by Eric Firing, the following work examines beam scattering via linear processes and the nonlinear transfers of internal tide energy to other frequencies and vertical scales.

In Chapter 2, the scattering of internal tide beams for Gaussian shaped stratification profiles is discussed. Two different beam scattering regimes are identified through LIMM experiments and a non-dimensional parameter predicting the amount of internal reflection that occurs due to changing stratification is proposed. The effects of rotation and stratification on nonlinear processes affecting internal tide beams are discussed in Chapter 3. Two-dimensional, nonlinear and nonhydrostatic numerical simulations of an M_2 internal tide beam with two realistic and vertically non-uniform stratification profiles are performed with the MITgcm. Interfacial waves in the pycnocline are generated for a range of latitudes with stratification representative of the Bay of Biscay, but not with a profile representative of Hawaii. Both sets of experiments show evidence of triadic resonant interactions.

CHAPTER 2

Scattering of internal tide beam energy due to non-uniform density stratification

2.1 Introduction

Tidal forcing from the Sun and Moon generates 3.7 terawatts (TWs) of mechanical power, of which 3.5 TWs are dissipated in the ocean (Munk & Wunsch, 1998). Numerical tide models that assimilate satellite altimeter data indicate that approximately 1 TW of barotropic tide power is lost away from coasts and shallow seas (Egbert & Ray, 2000, 2001), possibly contributing up to half of the energy needed for diapycnal mixing in the open ocean (Munk & Wunsch, 1998). Energy is transferred into the internal wave field when barotropic tides pass over underwater topography and generate internal tides (internal waves at tidal frequencies). Although the mechanism of internal tide generation has become better understood over the last decade, the principal locations and pathways of internal tide dissipation are still unknown (Garrett & Kunze, 2007, MacKinnon et al., 2013b). Consequently, the contribution of internal tides to global diapycnal mixing is not adequately quantified or parameterized in ocean models. In particular, it is not clear how much energy is available for mixing in and below the permanent thermocline.

Near the generation site, internal tide energy is confined in vertically limited structures, or beams, which propagate up towards the sea surface or down to the sea floor where reflection occurs. Observations indicate that after internal tide beams reflect off the sea surface they become nearly undetectable in horizontal kinetic energy (Martin et al., 2006, Cole et al., 2009, Johnston et al., 2011, Pickering & Alford, 2012), and depth-integrated energy fluxes can drop from 2 kW/m to almost 0 within 50 km of surface reflection (Althaus et al., 2003). Besides dissipation, a number of linear and nonlinear processes can contribute to the observed degradation of internal tide beams. Linear processes include beam scattering through multiple reflections and refractions due to non-uniform stratification (Gerkema, 2001, Gerkema & van Haren, 2012), geometric spreading (Rainville et al., 2010), and dephasing of the beam because modal wavelengths are not integer multiples in non-uniform stratification (Johnston et al., 2011). Nonlinear transformations can redistribute internal tide energy in frequency and wavenumber space (Polzin, 2004).

Numerical and laboratory studies suggest that as internal tide beams propagate up through varying stratification of the upper ocean, wave energy can be scattered through linear processes and lead to internal solitary waves (Gerkema, 2001, Akylas et al., 2007, Mercier et al., 2012, Gerkema & van Haren, 2012), or result in disintegration of the beam structure (Mathur & Peacock, 2009). Mathur & Peacock (2009) show that tidal beams can be significantly disrupted, resulting in multiple reflections and energy being horizontally ducted (possibly explaining the post-reflection disappearance of internal tide beams in observations). A modeling study by Gayen & Sarkar (2014) showed that only 30% of internal tide beam energy is reflected back down after surface reflection due to ducting and nonlinear transfer to other frequencies.

In this study beam scattering refers to the linear processes of refraction and internal reflection that can lead to the splitting of beams, the spreading and defocusing of beam energy, and the decrease of beam density. It is important to differentiate this from other definitions in the oceanography literature. In general scattering can refer to the process of reflection in contrast to absorption (Ferrari & Wunsch, 2009), to elastic scattering, to one of three triad classes put forth by McComas & Bretherton (1977), and most commonly, to interactions with topography that redistribute energy between modes and in

wavenumber space (St. Laurent & Garrett, 2002, Garrett & Kunze, 2007, Johnston et al., 2003, Johnston & Merrifield, 2003).

The numerical model and set-up are described in Section 2, along with the introduction of a metric to quantify scattering. Results from a previous study of scattering due to a simple piece-wise stratification profile (Gerkema, 2001) are reproduced and extended in Section 3, and additional experiments based on Gaussian stratification profiles are presented in Section 4. A summary and discussion of the results, open questions, and limitations of the study are presented in Section 5.

2.2 Methods

Numerical experiments are carried out using the Linear Inviscid Mode Model (LIMM), which solves the fluid dynamics equations of motion using vertical normal modes. It was developed by Eric Firing at the University of Hawaii. We start with a set of linearized and inviscid equations under the Boussineq approximation (Vallis, 2006) for a non-rotating two-dimensional (x,z) domain:

$$\frac{\partial u}{\partial t} = -\frac{1}{\rho_0}\frac{\partial p'}{\partial x}, \tag{2.1}$$

$$\frac{\partial w}{\partial t} = -\frac{1}{\rho_0}\left(\frac{\partial p'}{\partial z} + \rho' g\right), \tag{2.2}$$

$$\frac{\partial u}{\partial x} + \frac{\partial w}{\partial z} = 0, \tag{2.3}$$

where u and w are the horizontal and vertical velocities, respectively, pressure is

$$p = p_0(z) + p'(x,z,t),$$

density is

$$\rho = \rho_0 + \rho'(x,z,t),$$

$g = 9.81\,\mathrm{ms}^{-2}$ is the acceleration due to gravity, and

$$\frac{dp_0(z)}{dz} \equiv -g\rho_0.$$

Given a stratification (or buoyancy frequency) profile

$$N(z) = \sqrt{-\frac{g}{\rho_0}\frac{\partial \rho(z)}{\partial z}}, \tag{2.4}$$

linear baroclinic normal modes $U_m(z)$ and their wave speeds c_m are calculated for a continuously stratified flow with constant depth H. $U_m(z)$ and c_m are calculated as the eigenfuction and eigenvalue solutions to the Taylor-Goldstein equation (Sutherland, 2010), and solved numerically using python code developed by Eric Firing. LIMM is capable of including nonhydrostatic pressure terms, but the hydrostatic approximation is adequate for the experiments in this study. Note that the modes are not coupled in LIMM and energy can not be transferred between them.

The u-velocity field of a lunar semi-diurnal M_2 internal tide beam propagating to the right can be expressed as

$$u(x,z,t) = Re\left(\sum_m A_m U_m(z)\, exp(i\phi_m)\right), \tag{2.5}$$

where Re denotes taking the real part, A_m are the mode amplitudes,

$$\phi_m = \omega(t - x/c_m),$$

and ω is $1.41\times10^{-4}\,\mathrm{s}^{-1}$. In general A_m would be complex, but if $x = 0$ is chosen as the location where a beam is reflected from the bottom, the situation is simplified. At the point of reflection, the superposition of the downward beam from the left and the upward beam on the right forms a standing wave pattern, oscillating at the beam frequency ω but with no vertical propagation. In this case each A_m is real and can be calculated by projecting a given $u(z)$ profile onto the orthonormal modes U_m

so that

$$u(x=0,z,t=0)=\sum_m A_m U_m(z). \tag{2.6}$$

Now only the exponential in equation 2.5 is complex, and taking the real part changes the exponential to a cosine. The general wave expression then becomes

$$u(x,z,t)=\sum_m A_m U_m(z)\cos(\phi_m). \tag{2.7}$$

In the following experiments, the u-velocity of an internal tide beam at $x=0$, $t=0$ has the form of a second derivative of a Gaussian function

$$B(z)=B_0\left(1-\frac{(z+H)^2}{b_{scale}^2}\right)exp\left(-\frac{(z+H)^2}{2\,b_{scale}^2}\right), \tag{2.8}$$

where B_0 is the amplitude of the beam, b_{scale} is the width parameter, and z is positive upwards and varies from $-H$ to zero. $B(z)$ with $B_0 = 1\,\mathrm{m\,s^{-1}}$ and $b_{scale} = 400\,\mathrm{m}$ is shown with a piece-wise stratification N^2 profile and the associated vertical mode amplitudes A_m in Figure 2.1 (for Experiment E6 in Table 2.1).

With $U_m(z)$, c_m, and A_m calculated for specific $N(z)$ and $u(z)$ profiles, the fields p', w, and ρ' can be calculated from the Boussinesq equations given earlier. The zonal momentum balance (2.1) is used to solve for p', the vertical momentum balance (2.2) is used to solve for ρ', and the continuity equation (2.3) is used to solve for w:

$$p'(x,z,t)=\rho_0\sum_m c_m A_m U_m(z)\cos\phi_m, \tag{2.9}$$

$$\rho'(x,z,t)=\frac{-\rho_0}{g}\left(\sum_m c_m A_m\frac{dU_m(z)}{dz}\cos\phi_m-\omega^2\sum_m\frac{A_m}{c_m}\int_{-H}^{z}U_m(z')\,dz'\cos\phi_m\right), \tag{2.10}$$

$$w(x,z,t) = -\omega \sum_m \frac{A_m}{c_m} \int_{-H}^{z} U_m(z')\, dz' \sin\phi_m. \tag{2.11}$$

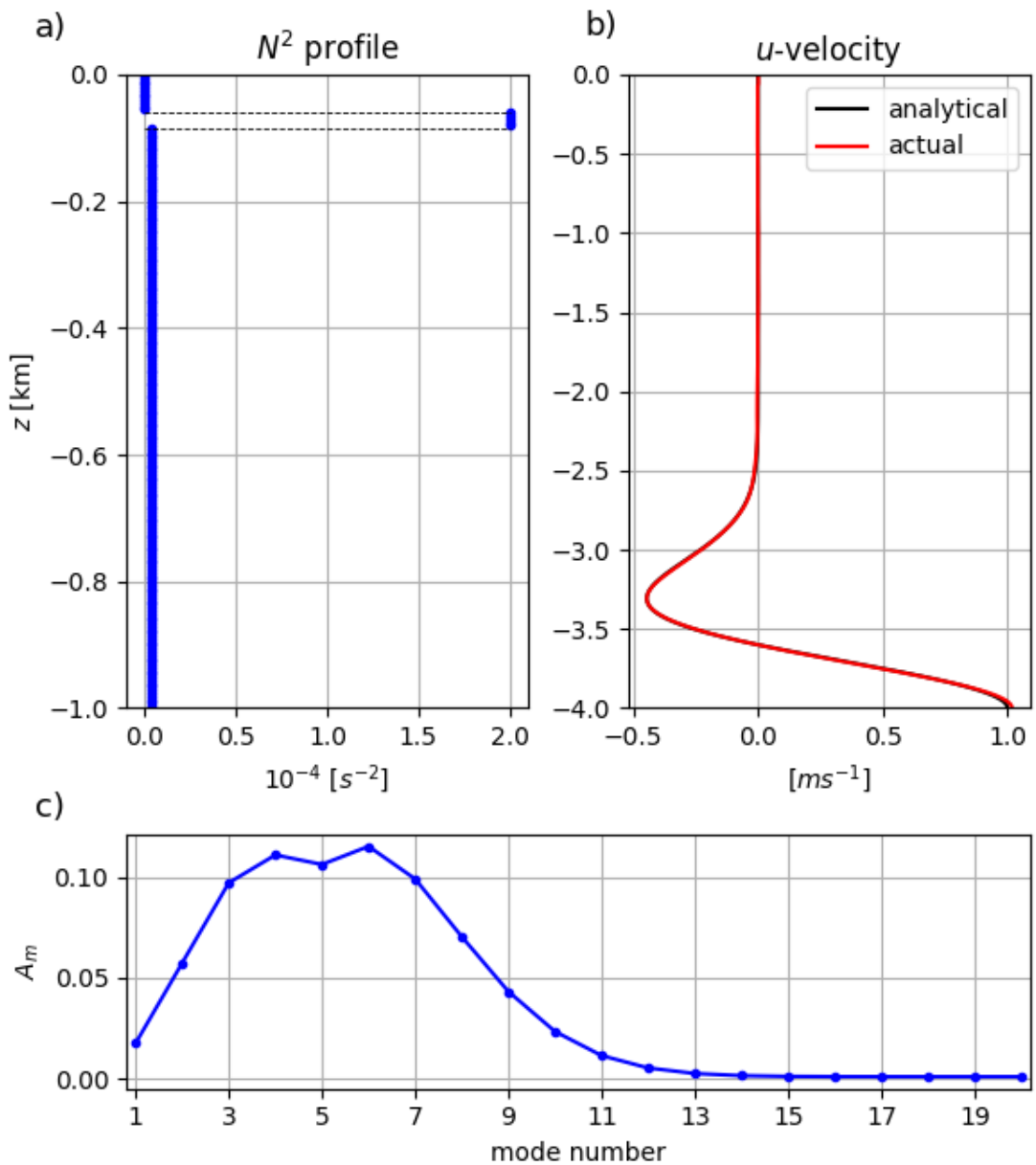

Figure 2.1: Stratification of Experiment E6 (a) is shown with the u-velocity profile of the beam (b) and the associated vertical mode amplitudes A_m (c). The beam velocity is projected onto modes that are based on the stratification profile to get the mode amplitudes. The analytical form of the beam is plotted in black, and the reconstructed beam as a sum of (20) modes is plotted in red (the two are almost identical here).

In an uniformly stratified and non-rotating medium, internal waves propagate according to the characteristic equation (Gill, 1982)

$$\frac{\lambda_z}{\lambda_x} = \sqrt{\frac{\omega^2}{N^2 - \omega^2}}, \tag{2.12}$$

where λ_z and λ_x are the vertical and horizontal wavelengths, respectively. The higher the frequency of a wave, the steeper its slope. According to the Liouville-Green (or WKB) approximation, if the properties of the medium (e.g., N) vary "slowly enough" such that the changes over the vertical scale of a wave are small, then the wave will refract but not reflect (Gill, 1982). Under this approximation, wave properties (such as the vertical wavelength) depend on the local properties of N as if N were uniform and on z only as far as N depends on z. When the WKB approximation breaks down due to rapidly changing stratification, internal reflection will occur and wave energy will not be fully transmitted.

As a way to quantify the amount of energy transmitted and reflected due to changing stratification, the vertical component of the perturbation energy flux $p'w$ (Gill, 1982) is calculated at a fixed depth z_i and integrated in the x direction. This will be referred to as the Horizontal Integrated Flux (HIF):

$$HIF(x, z_i) = \int_0^x p'(x, z_i, t) w(x, z_i, t)\, dx, \tag{2.13}$$

which depends on the fixed depth z_i and varies with x. HIF is a cumulative sum of net energy flux passing through z_i, from 0 to x. When $HIF(x, z_i)$ is zero it means that the amount of upward energy flux passing through z_i from 0 to x is balanced by downward energy flux. This interpretation depends on the assumption that there is no energy dissipation, which is true for LIMM.

2.3 Scattering due to piece-wise N^2 profile

Scattering as a function of pycnocline strength was studied by Gerkema (2001) using an analytical model. His model solves for the structure of the internal tide field resulting from an internal tide

beam propagating in a domain with a three-layer piece-wise stratification profile, with each layer having a constant N^2 value (Figure 2.2). The top layer was unstratified and had depth d, the bottom layer had $N^2 = 4 \times 10^{-6}\,\mathrm{s}^{-2}$, and the pycnocline layer had thickness ε and $N^2 = PS_1/\varepsilon$. Prior to numerically solving over the domain, he takes the limit as the pycnocline thickness ε goes to zero, reducing the pycnocline to an interface (he refers to this as the *2-c layer model*).

The pycnocline strength parameter[1], PS_1, is equal to the area under the N^2 curve in the pycnocline layer, a fact noted by Gerkema (2001) as useful for comparison with realistic profiles. He found that scattering of an internal tide beam occurred for a "moderately developed" pycnocline, but not for a pycnocline that is very weak or very strong. With a weak pycnocline the internal tide beam effectively reflected off the surface, and for a strong pycnocline the reflection was off the base of the pycnocline. Gerkema proposed that the scattering in the moderate pcynocline, essentially a linear process, is the first step in the "local" generation of internal solitary waves, a nonlinear and nonhdrostatic process.

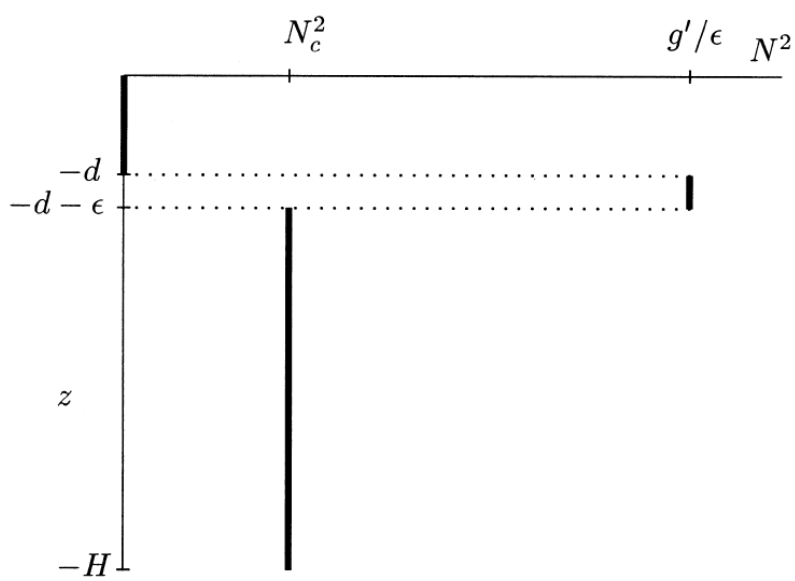

Figure 2.2: Figure 2 from Gerkema (2001) shows the set-up of his analytical *2c-layer model*. The stratification consists of an unstratified top layer of thickness d ($N^2 = 0$), a pycnocline layer of thickness ε and $N^2 = g'/\varepsilon$, and a lower layer with constant stratification ($N_c^2 = 4{\times}10^{-6}\,\mathrm{s}^{-2}$). H is the total water depth.

LIMM was used to reproduce the results from Gerkema (2001). Our numerical model set-up is

[1] Gerkema (2001) referred to this parameter as g'.

made to be as similar to G01 as possible, but the ε parameter is necessarily non-zero and is limited by the vertical resolution. In the following experiments, the domain is two-dimensional, with depth of 4 km and horizontal distance of 500 km. The vertical resolution is 5 m and the horizontal resolution is 60 m. The number of modes used in calculations is 20, and nonhydrostatic terms are not included. Table 2.1 lists the parameters for these piece-wise N^2 experiments. The PS_1 values used in LIMM experiments are similar to those from G01 or are within the range given.

Table 2.1: Information about the piece-wise N^2 profile experiments, for comparison with Gerkema (2001). Ducting refers to partial vertical confinement of energy. The regime $\mathscr{R}_j$ is related to the PS_1 and ε parameters.

Regime	Gerkema	PS_1 [m s^{-2}]	d [m]	ε [m]	main feature	name
$\mathscr{R}_1$	case A	0	60	5	reflection at surface	E1
$\mathscr{R}_2$	case C	5×10^{-3}	60	5	ducting in top layer	E3
$\mathscr{R}_3$	case B	1×10^{-1}	60	5	reflection at pycnocline	E2
$\mathscr{R}_1$	case A	0	60	25	similar to E1	E4
$\mathscr{R}_2$	case C	5×10^{-3}	60	25	similar to E3	E6
$\mathscr{R}_4$	n/a	1×10^{-1}	60	25	ducting in pycnocline	E5
$\mathscr{R}_1$	case A	0	120	25	similar to E1	E7
$\mathscr{R}_2$	case C	5×10^{-3}	120	25	similar to E3	E9
$\mathscr{R}_4$	n/a	1×10^{-1}	120	25	similar to E5	E8

The three cases discussed in Gerkema (2001) are reproduced with $\varepsilon = 5$ m and shown in Figure 2.3. Experiment E1 reproduces the weak or absent pycnocline case ($PS_1 = 0$), which we will call Regime $\mathscr{R}_1$. In Regime $\mathscr{R}_1$ the internal tide beam remains relatively undisturbed by the change in stratification and reflects back down from the surface. In Experiment E2 ($PS_1 = 0.1$), the pycnocline is so strong that the beam reflects off the bottom of it as if it were a rigid surface, showing only small disturbances in the mixed layer (see Figure 2.4 for view of u-velocity in the top 1 km). We call this Regime $\mathscr{R}_3$. Gerkema found that only for intermediate values of PS_1, ranging roughly between 0.002 to 0.02, does scattering occur. We call this Regime $\mathscr{R}_2$.

Gerkema describes Regime $\mathscr{R}_2$ as the moderate pycnocline case, and it is characterized by the decrease in beam energy density after surface reflection, the spreading of wave-energy over the domain, and the presence of wave-activity that leads to energy in the mixed layer. Gerkema

describes the energy being ducted in the mixed layer as currents, but in Experiment E3 (Figure 2.4) they look more like waves because of their alternating phase pattern as the energy propagates to the right. We describe this as ducting, or partial vertical confinement of energy. There is a clear downward leaking of energy from the mixed layer in the form of beams, and it appears to be the interference pattern of this multitude of beams that makes it look like energy is spread "all over the domain," as noted by Gerkema. Experiment E3 was repeated with $\varepsilon = 25$ m (E6), and then repeated with pycnocline depth d increased to 120 m (E9). No major differences were observed, suggesting that Regime $\mathscr{R}_2$ scattering is not sensitive to d or ε.

As expected, Regime $\mathscr{R}_1$, the no pycnocline case (effectively a 2-layer system with constant but different N^2 values), is also not sensitive to d or ε. In contrast, a new regime $\mathscr{R}_4$ was found when a Regime $\mathscr{R}_3$ experiment (E2) was repeated with ε increased to 25 m. In the new Regime $\mathscr{R}_4$ experiment (E5, bottom panel of Figure 2.4) we see that ducting in the mixed layer is replaced by ducting in the pycnocline layer, which is not possible in the *2-c layer model* of Gerkema (2001) because the pycnocline there was reduced to an interface. Increasing d to 120 m did not result in major differences and suggests that this new regime $\mathscr{R}_4$ is not sensitive to the depth of the pycnocline, though it appears to depend on the thickness of the pycnocline.

2.4 Scattering due to Gaussian N^2 profiles

2.4.1 Comparison with piece-wise N^2 profiles

The nine experiments from the previous section were repeated using a Gaussian approximation of the piece-wise N^2 profile. The form of the Gaussian stratification profile was

$$G(z) = A_N \left[exp\left(-\frac{(z - z_{pyc})^2}{2\sigma^2} \right) \right] + N^2_{min}, \tag{2.14}$$

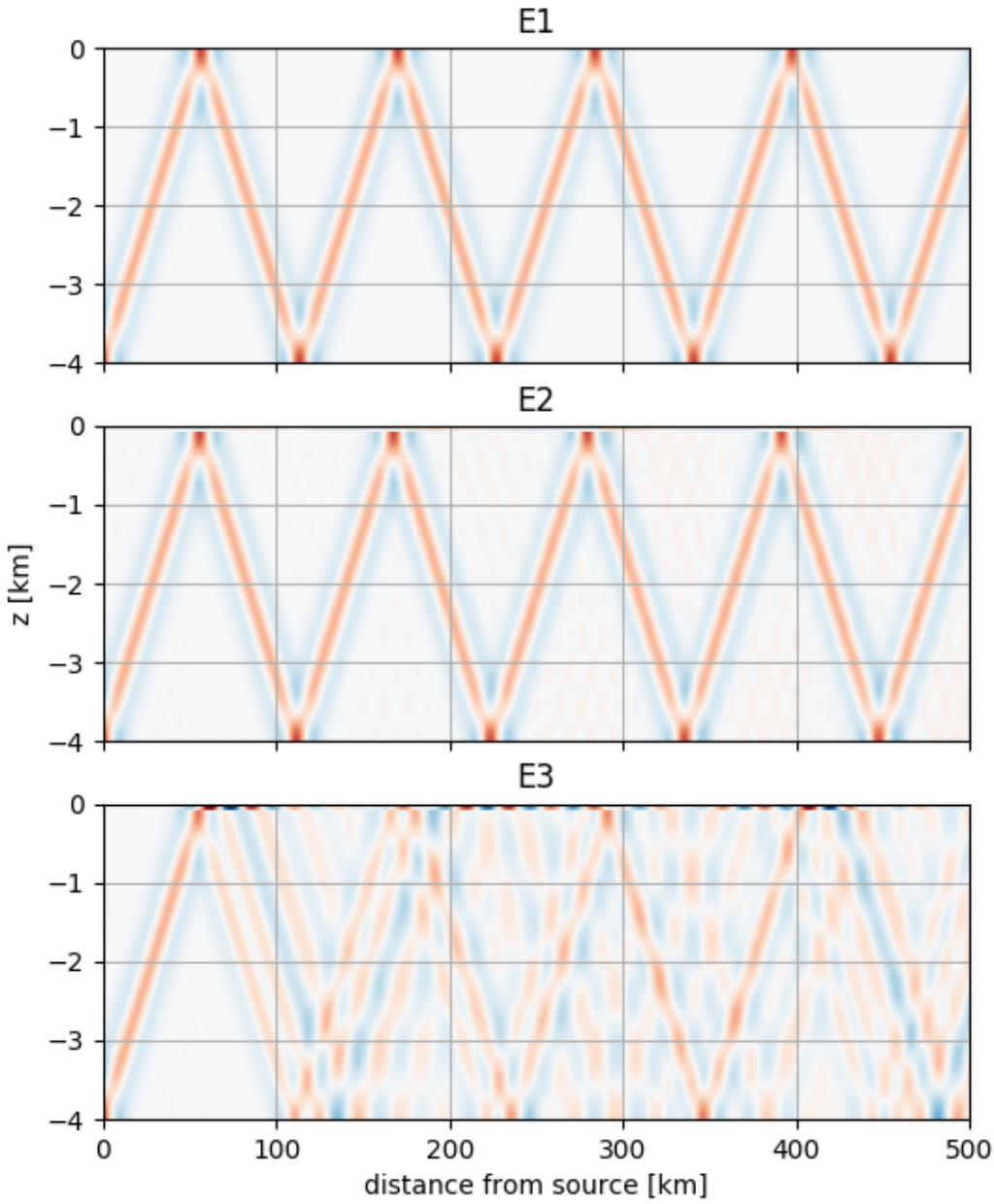

Figure 2.3: Horizontal u-velocity (full domain) for piece-wise N^2 experiments: E1 - the absent pycnocline case (Regime $\mathscr{R}_1$), E2 - the strong pycnocline case (Regime $\mathscr{R}_3$), and E3 - the moderate pycnocline case (Regime $\mathscr{R}_2$).

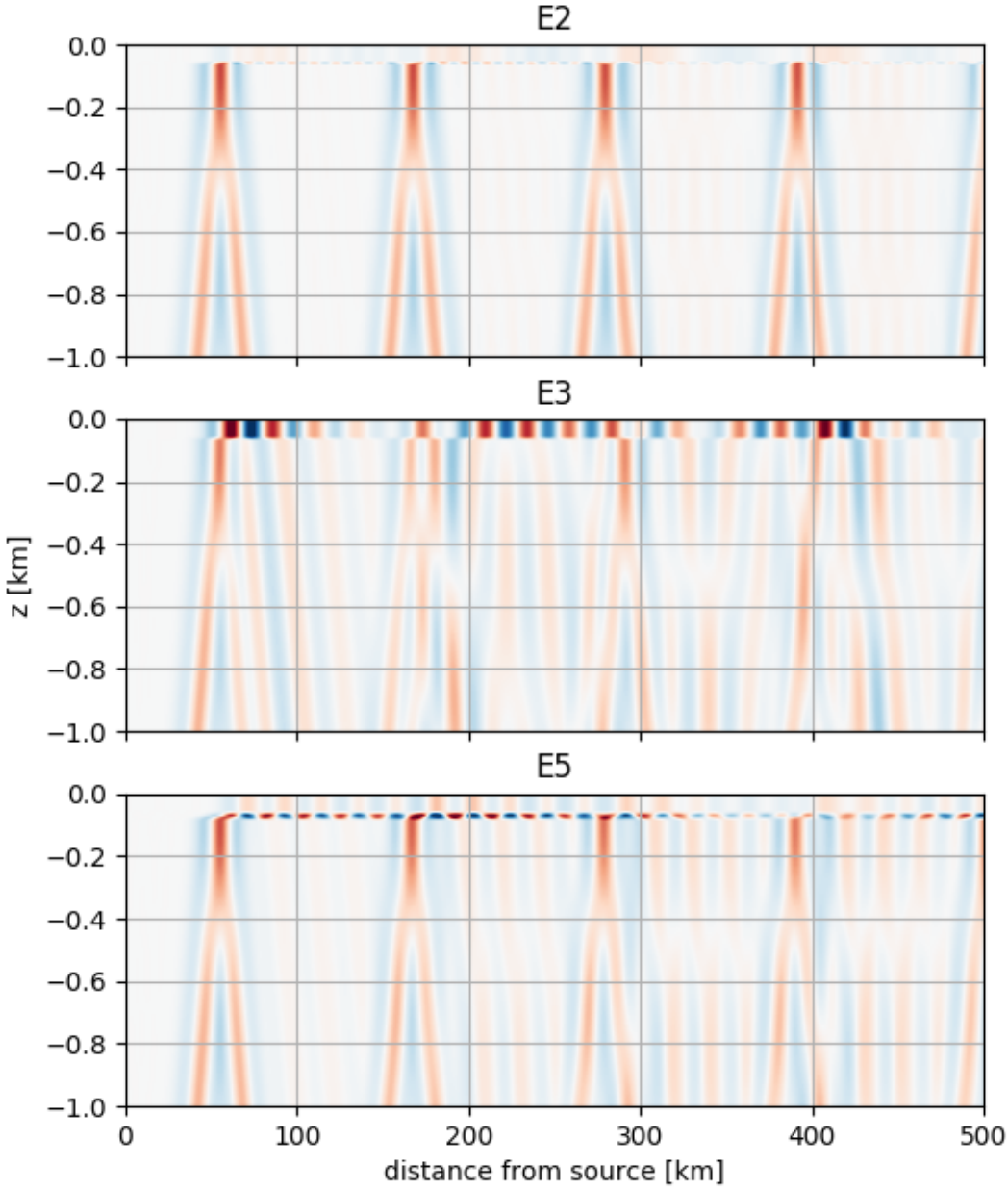

Figure 2.4: Horizontal u-velocity (upper 1 km) for piece-wise N^2 experiments: E2 - the strong pycnocline case (Regime $\mathscr{R}_3$), E3 - moderate pycnocline case (Regime $\mathscr{R}_2$), and E5 - the pycnocline ducting case (Regime $\mathscr{R}_4$).

where A_N is the amplitude, z_{pyc} is the center of the pycnocline, σ is the thickness parameter for the pycnocline, and $N^2_{min} = 4\times10^{-6}\,\mathrm{s}^{-2}$, unless otherwise noted. Values for the constants PS_2, z_{pyc}, and σ are given in Table 2.2. There was no observable difference between having $N = 0$ compared to $N = N_{min}$ in the top layer, so we adopt the latter for simplicity.

The Gaussian profile varies more smoothly than the piece-wise profile, and models a gradual change in stratification that is more representative of the ocean. The piece-wise stratification experiment with a moderately developed pycnocline ($PS_1 = 5\times10^{-3}\,\mathrm{m\,s}^{-2}$) centered at 70 m depth (E6) is repeated with a comparable Gaussian profile (hE6). The N^2 profiles of Experiments E6 and hE6 are shown in Figure 2.5(a). The vertical integrals of the two curves are visually comparable. The pycnocline strength parameter for Gaussian stratification profiles is defined as $PS_2 = 2A_N\sigma$. PS_2, like PS_1, is an estimate of the area under the N^2 curve. Specifically, PS_1 is an exact measure of the area under the curve, whereas PS_2 is an underestimate. Both appear to be adequate measures for the purpose of quantifying pycnocline strength, as we will see. The vertical modes calculated from the different stratification profiles are extremely similar (the first three modes are shown in Figure 2.5(b-c), suggesting that the velocity, pressure, and density fields will be similar as well.

The Gaussian stratification experiments are very similar to the piece-wise stratification experiments (compare Figures 2.3 and 2.4 with Figures 2.6 and 2.7). In the weak pycnocline cases (e.g., Experiment hE1), the internal tide beam remains relatively undisturbed by the change in stratification and reflects back down from the surface. Instead of $PS_2 = 0$, a very small value was used for these Regime $\mathscr{R}_1$ experiments so that N would not be constant. For Regime $\mathscr{R}_2$ experiments with a moderately developed pycnocline (e.g., hE3), internal tide beam energy is ducted in the top layer and spread out in the lower layer (see Figure 2.7 for view of u-velocity in the top 1 km). In Regime $\mathscr{R}_3$ (Experiment hE2), the beam again reflects off the bottom of the strong pycnocline as if it were a rigid surface, showing only small disturbances in the mixed layer and the pycnocline. Experiment hE2 shows a little more disturbance in the pycnocline than its piece-wise stratification counterpart (E2), but is still clearly in Regime $\mathscr{R}_3$.

When the pycnocline thickness of a strong pycnocline experiment (hE2) is increased to $\sigma = 12.5$ m,

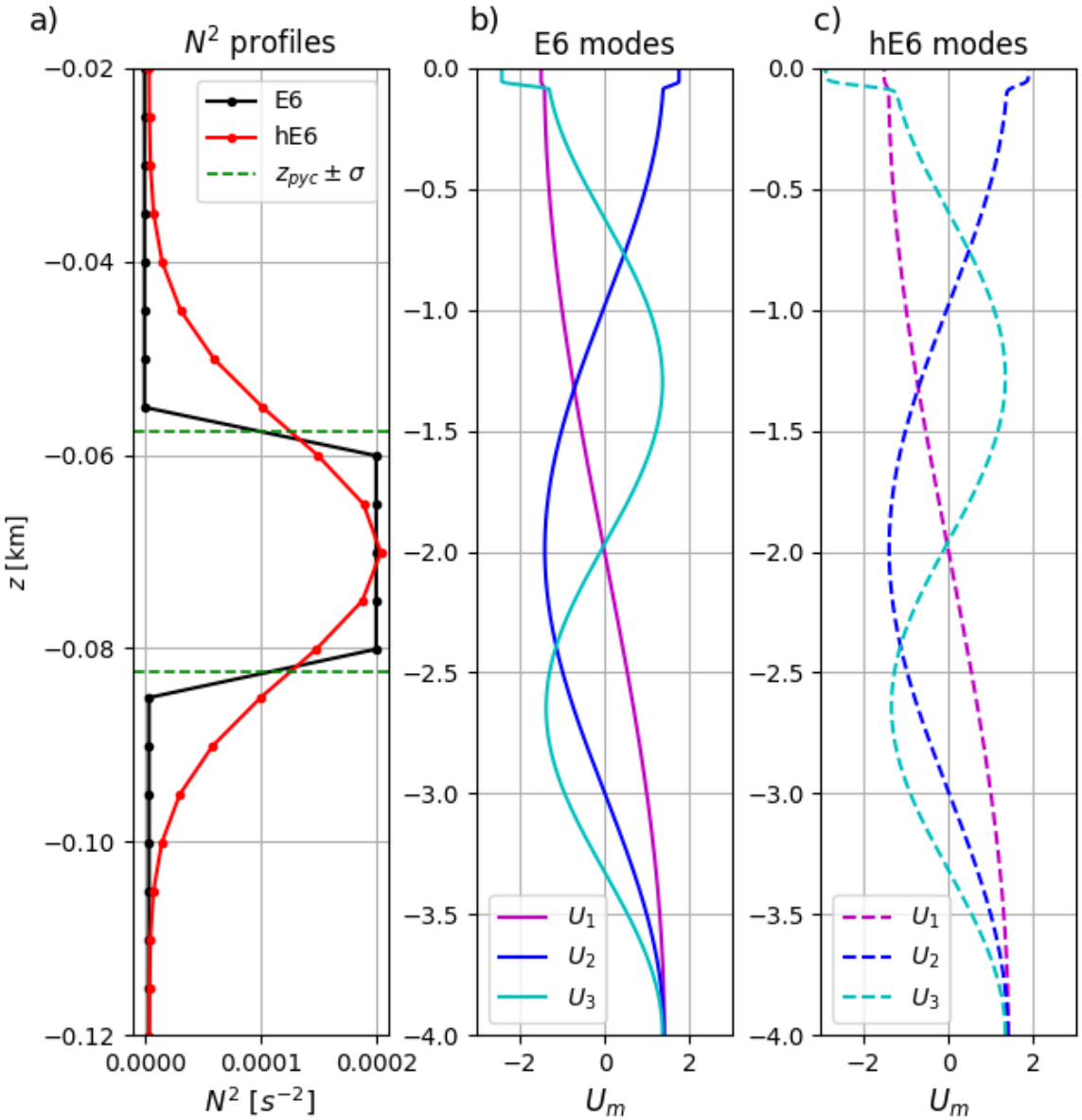

Figure 2.5: Stratification profiles for experiments E6 and hE6 (a) are plotted together for comparison. The first three vertical modes calculated with the E6 and hE6 profiles are shown in b) and c), respectively. The vertical axis of a) is for the top 20-120 m while the axes for b) and c) are for the full depth of 4 km. Green dashed lines at $z_{pyc} \pm \sigma$ indicate the boundaries for the vertical integral represented by PS_2, where σ is a defining parameter for the Gaussian stratification profile.

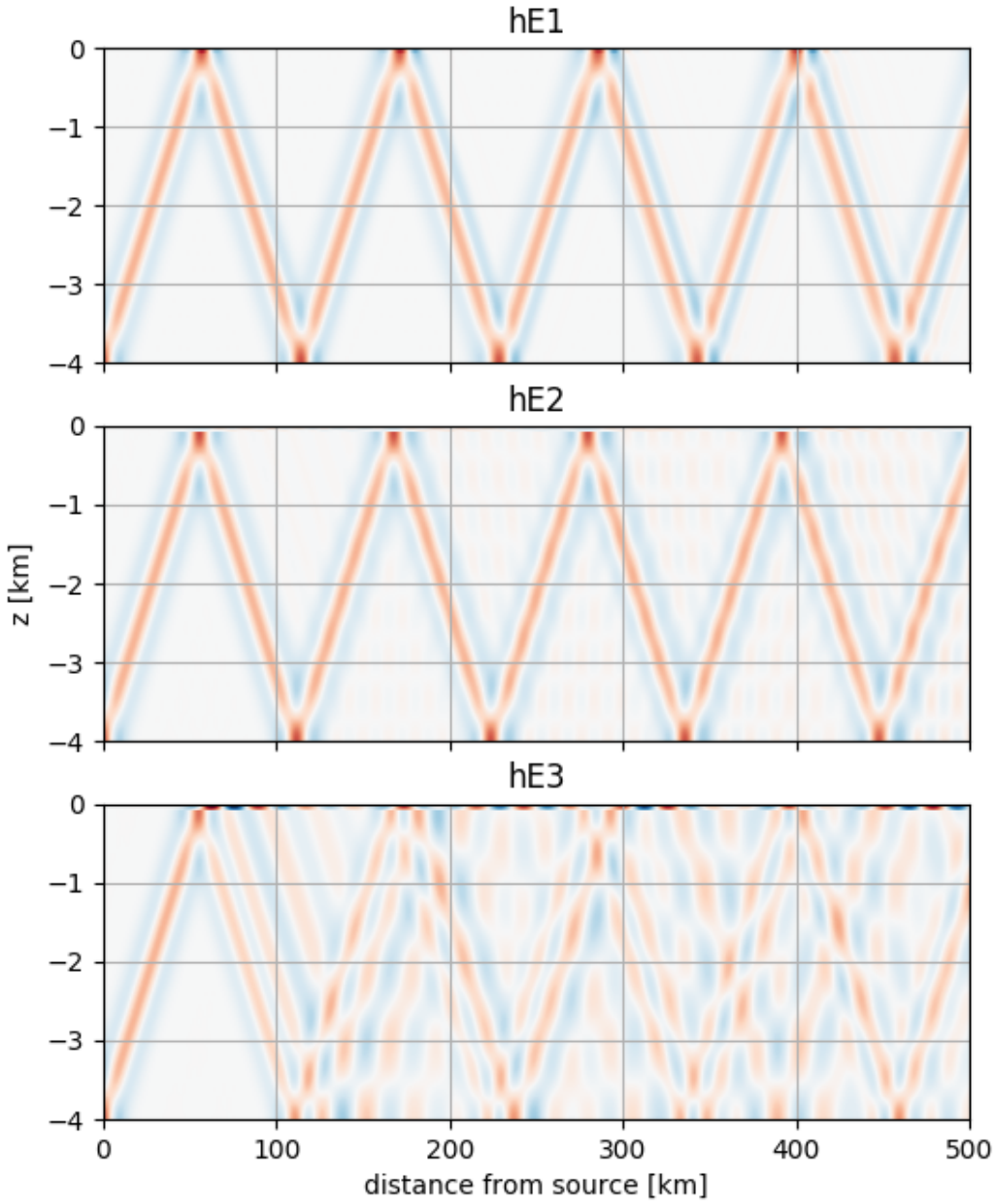

Figure 2.6: Horizontal u-velocity (full domain) for Gaussian N^2 experiments: hE1 - the absent pycnocline case (Regime $\mathscr{R}_1$), hE2 - the strong pycnocline case (Regime $\mathscr{R}_3$), and hE3 - the moderate pycnocline case (Regime $\mathscr{R}_2$).

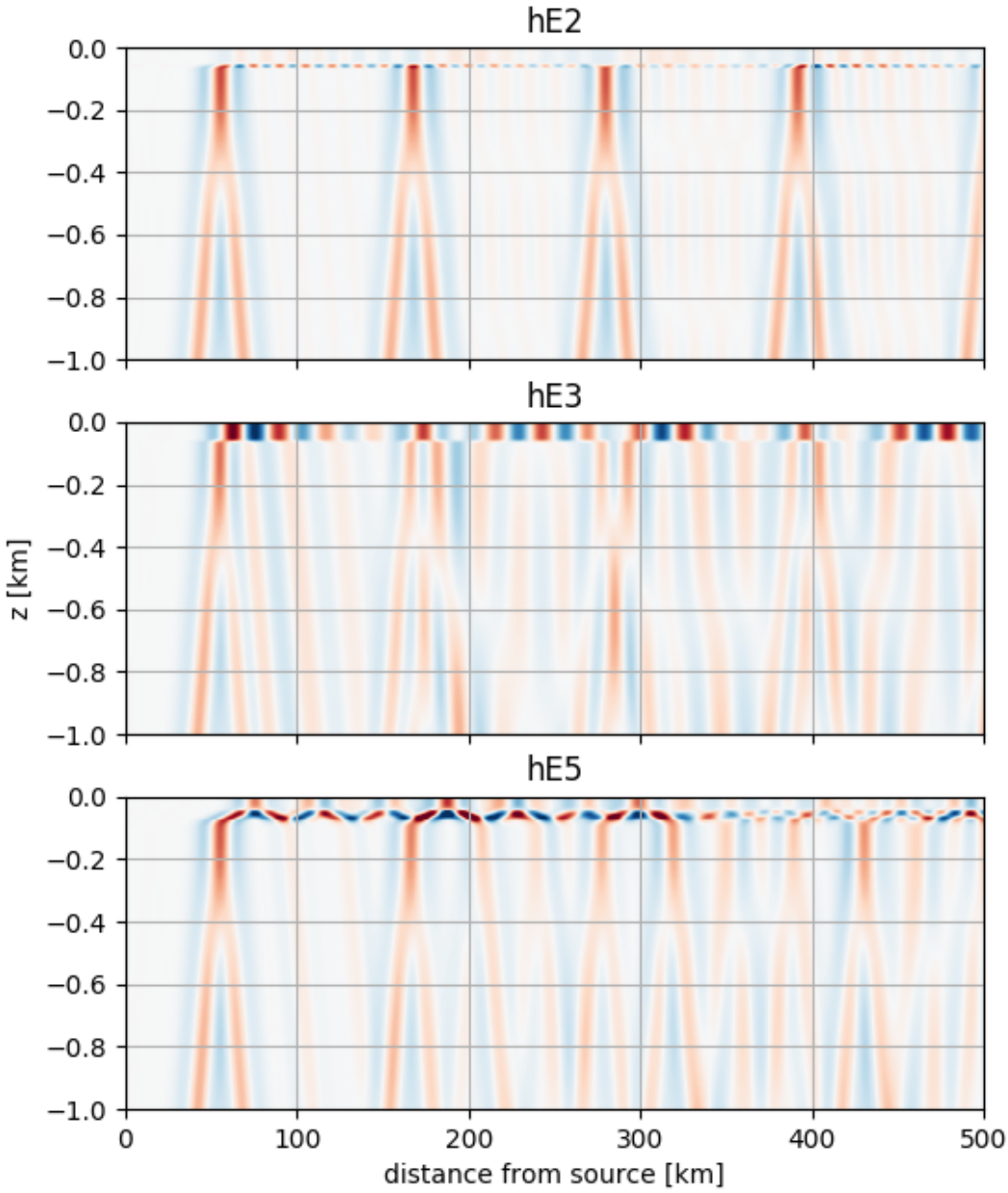

Figure 2.7: Horizontal u-velocity (upper 1 km) for Gaussian N^2 experiments: hE2 - the strong pycnocline case (Regime $\mathscr{R}_3$), hE3 - moderate pycnocline case (Regime $\mathscr{R}_2$), and hE5 - the pycnocline ducting case (Regime $\mathscr{R}_4$).

there is again a regime change from $\mathscr{R}_3$ to $\mathscr{R}_4$, with the appearance of ducting in the pycnocline layer (hE5). It appears that Regime $\mathscr{R}_3$ results from very thin pycnoclines ($\sigma <\sim 10$ m) that are unlikely to be found in the ocean, and Regime $\mathscr{R}_4$ is associated with a more realistic N^2 profile. As seen before, the depth of the pycnocline does not seem to matter, and pycnocline thickness only matters for the strong pycnocline case. Descriptions and examples of the four different regimes are given in Table 2.3.

Table 2.2: Information about Gaussian N^2 profile experiments, for comparison with experiments from Table 2.1. The regime $\mathscr{R}_j$ is related to the PS_2 and σ parameters.

Regime	PS_2 [m s^{-2}]	z_{pyc} [m]	σ [m]	main feature	name	compare
$\mathscr{R}_1$	5×10^{-4}	- 60	2.5	reflection at surface	hE1	E1
$\mathscr{R}_2$	5×10^{-3}	-60	2.5	ducting in top layer	hE3	E3
$\mathscr{R}_3$	1×10^{-1}	-60	2.5	reflection at pycnocline	hE2	E2
$\mathscr{R}_1$	5×10^{-4}	-70	12.5	similar to hE1	hE4	E4
$\mathscr{R}_2$	5×10^{-3}	-70	12.5	similar to hE3	hE6	E6
$\mathscr{R}_4$	1×10^{-1}	-70	12.5	ducting in pycnocline	hE5	E5
$\mathscr{R}_1$	5×10^{-4}	-130	12.5	similar to hE1	hE7	E7
$\mathscr{R}_2$	5×10^{-3}	-130	12.5	similar to hE3	hE9	E9
$\mathscr{R}_4$	1×10^{-1}	-130	12.5	similar to hE5	hE8	E8

Table 2.3: Behavior of internal tide beams passing through non-uniform stratification can be categorized into four different regimes, based on the PS_2 and σ parameters.

Regime	PS_2 [m s^{-2}]	σ [m]	main feature	example
$\mathscr{R}_1$	$\leq 5\times10^{-4}$	any	weak pycnocline, no scattering	hE1
$\mathscr{R}_2$	$\sim 5\times10^{-3}$	any	moderate pycnocline, top layer ducting	hE3
$\mathscr{R}_3$	$\geq 1\times10^{-2}$	$\leq 5/2$	strong pycnocline, almost no scattering	hE2
$\mathscr{R}_4$	$\geq 1\times10^{-2}$	$\geq 25/2$	strong pycnocline, pycnocline layer ducting	hE5

2.4.2 Going towards more realistic N^2 profiles

In this section we use the HIF metric (introduced in section 2) to quantify the amount of scattering and ducting in Regimes $\mathscr{R}_2$ and $\mathscr{R}_4$ (the two other regimes do not show scattering). By comparing the horizontal location and magnitude of increases and decreases in $HIF(x, z_i)$ with a u-velocity plot,

we can estimate the amount of energy flux crossing a certain depth z_i from 0 to x. $HIF_n(x, z_i)$ is normalized by the maximum $HIF(x, z_i)$ value and ranges from 0 to 1.

First we will consider a realistic stratification profile that is based on averaging ten years of conductivity, temperature, and depth (CTD) data from the Hawaii Ocean Time-series program (HOT) at station ALOHA (Karl & Lukas, 1996). We will refer to this as the HOT profile, and it is similar to what was used in the internal tide generation model described in Carter et al. (2008). Figure 2.8 shows the u-velocity and associated $HIF_n(x, z_i = 1.5\,\text{km})$ curve of the HOT simulation. The velocity field shows that there is very little scattering in the sense of beam splitting, reduced beam amplitude, or horizontal ducting of energy in the top or pycnocline layer. The internal tide beam reflects off both the surface and the bottom without much change to its beam structure. $HIF_n(x, z_i)$ goes from zero to its maximum when the internal tide beam first passes z_i on its upward trajectory ($x \sim 20\,\text{km}$), and decreases to approximately 0 (< 0.006) when the beam passes z_i on its way down ($x \sim 1100\,\text{km}$). The increases and decreases of $HIF_n(x, z_i)$ occur over a small horizontal extent. This means that almost all (> 0.99) of the internal tide beam energy that went up past z_i as a single beam came back down as a single beam. As the beam propagates to the right and reflects off the top and bottom boundaries, progressively more energy is lost from the beam due to scattering (not to dissipation since LIMM is an inviscid model), but the beam remains largely intact.

A number of experiments are performed to examine the effects of different Gaussian stratification profiles on the energy flux of an internal tide beam (Table 2.4). The N^2 profiles of a few experiments (G1, G2, G4, and G6) are plotted with the HOT profile for comparison (Figure 2.9). Recall that PS_2 is a lower bound estimate of the area under Gaussian N^2 profiles, and this allows for visual comparison of PS_2 values. The main point of Table 2.4 experiments is that PS_2 predicts whether there is a pycnocline layer, and whether ducting is mainly in the top layer or in the pycnocline layer. We find that the transition between Regimes $\mathscr{R}_2$ and $\mathscr{R}_4$ occurs roughly around $PS_2 = 0.01\,\text{m}\,\text{s}^{-2}$, with smaller values indicating Regime $\mathscr{R}_2$ and larger values indicating Regime $\mathscr{R}_4$. By a rough visual comparison it appears that the area under the N^2 profile is larger for HOT than it is for G6, suggesting that the HOT experiment would be in Regime $\mathscr{R}_4$ since G6 is in Regime $\mathscr{R}_4$.

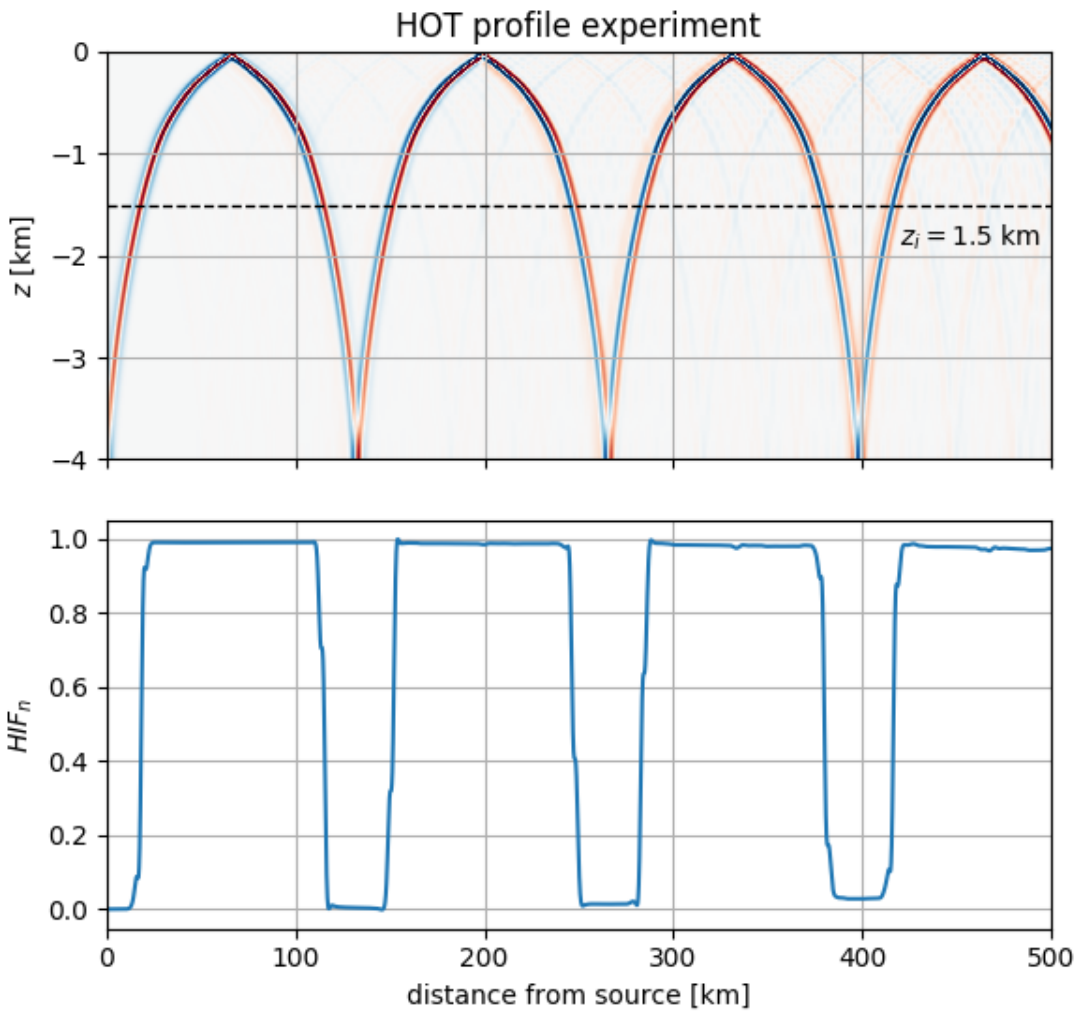

Figure 2.8: The u-velocity (top) and $HIF_n(x, z_i = 1.5\,\text{km})$ (bottom) for the HOT profile experiment. The internal tide beam propagates though the pycnocline and reflects off the top and bottom boundaries without losing much energy to scattering. The HIF curve shows that almost all of the upward energy flux is balanced by downward energy flux between $x = 0$ and 125 km.

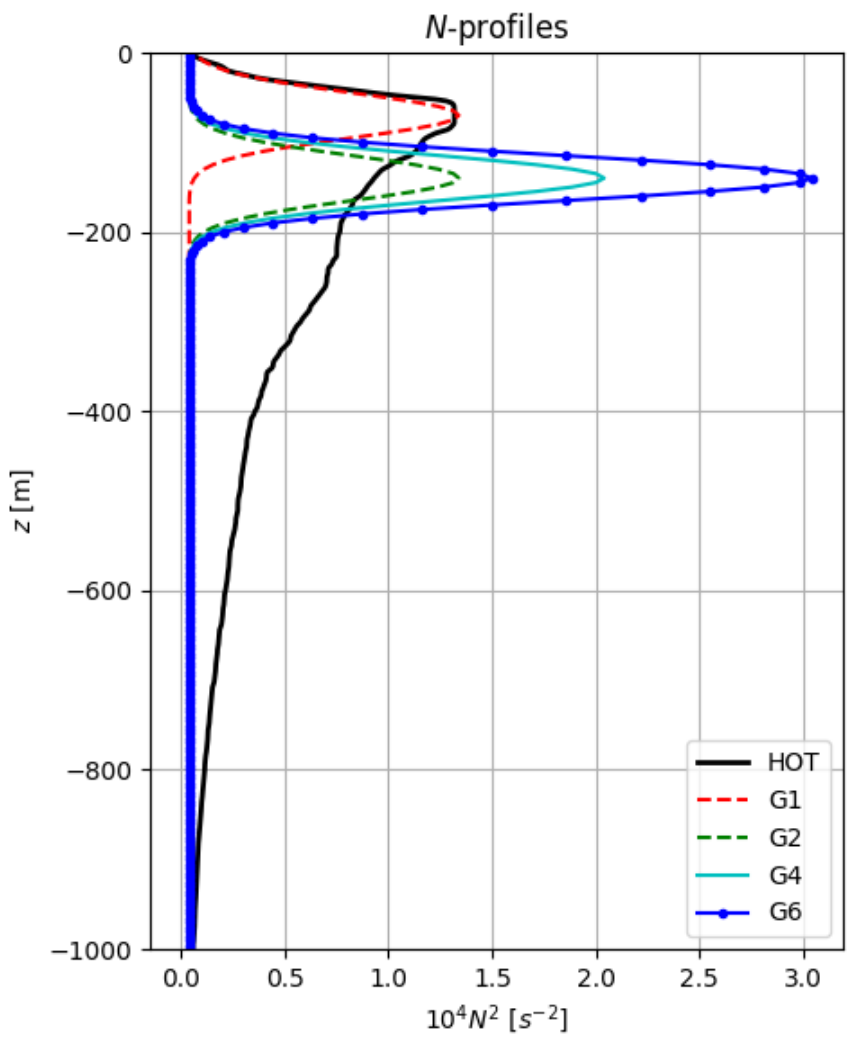

Figure 2.9: Stratification N^2 profiles for various experiments are shown together for comparison of their vertical integrals (areas under the N^2 curve). The PS_2 parameter is an (under)estimate of the area under the N^2 curve, and is related to the type and amount of scattering.

Table 2.4: Parameters for Gaussian stratification experiments are listed. The type of scattering (Regimes $\mathscr{R}_2$ or $\mathscr{R}_4$) is related to $PS_2 = 2A_N\sigma$, but not to z_{pyc}. The transition between Regimes $\mathscr{R}_2$ and $\mathscr{R}_4$ occurs roughly around $PS_2 = 0.01\,\mathrm{m\,s^{-2}}$, with smaller values indicating Regime $\mathscr{R}_2$ and larger values indicating Regime $\mathscr{R}_4$.

Regime	PS_2 [m s^{-2}]	Percent Reflection	z_{pyc} [m]	σ [m]	$A_N[s^{-2}]$	name
$\mathscr{R}_2$	0.0065	30	-70	25	1.3×10^{-4}	G1
$\mathscr{R}_2$	0.0065	40	-140	25	1.3×10^{-4}	G2
$\mathscr{R}_2$	0.0065	47	-210	25	1.3×10^{-4}	G3
$\mathscr{R}_2$	0.0075	50	-140	15	2.5×10^{-4}	G12
$\mathscr{R}_2$	0.0075	56	-210	15	2.5×10^{-4}	G13
$\mathscr{R}_4$	0.010	52	-140	25	2.0×10^{-4}	G4
$\mathscr{R}_4$	0.010	56	-210	25	2.0×10^{-4}	G5
$\mathscr{R}_4$	0.015	56	-140	25	3.0×10^{-4}	G6
$\mathscr{R}_4$	0.015	58	-210	25	3.0×10^{-4}	G7
$\mathscr{R}_4$	0.020	57	-140	25	4.0×10^{-4}	G8
$\mathscr{R}_4$	0.020	58	-210	25	4.0×10^{-4}	G9
$\mathscr{R}_4$	0.050	58	-140	25	1.0×10^{-3}	G10
$\mathscr{R}_4$	0.050	58	-210	25	1.0×10^{-3}	G11

In the ocean the u-velocity of upward propagating internal tide beams are often undetectable after the first surface reflection (Martin et al., 2006, Pickering & Alford, 2012), so interference with beams that have reflected off the bottom is unlikely. To study the scattering effects from a single beam, for simplicity, the experiment domain is made to be very deep so that the bottom reflected beams do not come back to the study region. Figure 2.10 shows two different simulations using the same N^2 profile (G1); one has domain that is 4 km deep and one that is 40 km deep. Since the beam is still generated at the bottom of the water column at $x = 0$, it now comes up to the surface much farther from the source (around 570 km instead of 50 km). In the deep domain simulation, bottom reflection occurs far from the surface reflection, and the upward and downward beams do not meet in the region shown. The number of modes used in calculations is increased from 20 to 125 to account for the narrowness of the beam relative to the increased depth of the water column.

Stratification profile G1 has the same $max(N^2)$ as the HOT profile (Figure 2.9), but its PS_2 value is less than $1\times10^{-2}\,\mathrm{m\,s^{-2}}$, indicating it is in Regime $\mathscr{R}_2$. Based on $HIF_n(x, z_i = 2\,\mathrm{km})$, we estimate that approximately 30% of energy flux is internally reflected downward as the internal tide beam

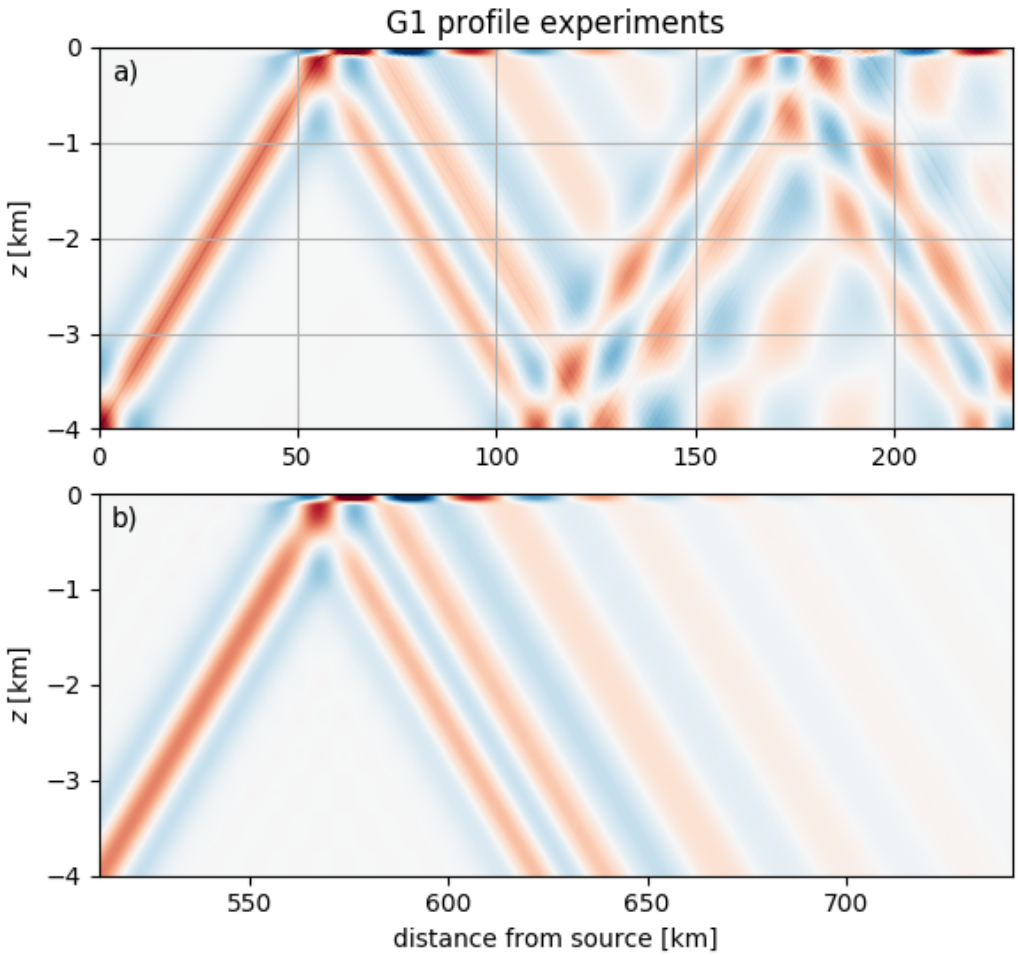

Figure 2.10: Two experiments are run with the G1 stratification profile for different sized domains: a) H = 4 km and b) H = 40 km. In the deep domain simulation, bottom reflection occurs far from the surface reflection and the upward and downward beams do not meet in the region shown.

passes through the pycnocline (Figure 2.11). $HIF_n(x, z_i)$ reaches a maximum once the beam has fully passed above 2 km depth, around $x \sim$550 km. Around $x \sim$600 km, a downward beam causes HIF_n to decrease to 0.7, and then decrease further as energy ducted in the top layer leaked downward in the form of beams. The first reduction of 30% appears to be due to internal reflection at the base of the pycnocline. The remaining energy (70%) passes through the pycnocline where the beam is refracted, as expected from equation 2.12, and then into the top layer where ducting and surface reflection happens. The pycnocline depths are increased in Experiments G2 (Figure 2.12) and G3 (not shown), and both stay in Regime $\mathscr{R}_2$ and show top layer ducting. The three experiments differ only in that the amount of internal reflection increases with depth of the pycnocline (see Table 2.4).

Regime $\mathscr{R}_2$ scattering is characterized by ducting in the top layer and subsequent downward leaking of energy in the form of beams. The horizontal scale of the ducted energy appears to increase with increased pycnocline depth. With PS_2 and other variables (σ, A_N) fixed, increasing the pycnocline depth increases the amount of internal reflection at the base of the pycnocline (also referred to as percent reflection). Experiment G1 with z_{pyc} = -70 m shows 30% reflection while Experiment G2 with z_{pyc} = -140 m shows 40%. As the amplitude of the N^2 profile is increased, e.g., Experiments G4 and G7 (Figures 2.13 and 2.14), scattering moves from Regime $\mathscr{R}_2$ to Regime $\mathscr{R}_4$ as ducting shifts from the top layer to the pycnocline layer. Experiment G4 shows the transition from Regime $\mathscr{R}_2$ to Regime $\mathscr{R}_4$, where ducting in the pycnocline layer starts to appear. The percent reflection for Experiment G4 is around 52%, and increases only slightly (by 4%) when the pycnocline depth is increased from 140 m to 210 m (Experiment G5). This is a signature of Regime $\mathscr{R}_4$, that percent reflection is independent of z_{pyc}, in contrast to Regime $\mathscr{R}_2$ where percent reflection is highly dependent on z_{pyc}.

Holding other factors constant, increasing A_N leads to the regime change from $\mathscr{R}_2$ to $\mathscr{R}_4$ because PS_2 is increased. If the increase of A_N is accompanied by a reduction in σ so that PS_2 remains below a certain threshold (approximately 0.01 m s^{-2}), scattering will still be of the Regime $\mathscr{R}_2$ type unless the pycnocline is too weak to support scattering (i.e., Regime $\mathscr{R}_1$, see Table 2.3). For example, Experiment G12 (Figure 2.15) has larger A_N than an in-between-regimes experiment (e.g., Experiment

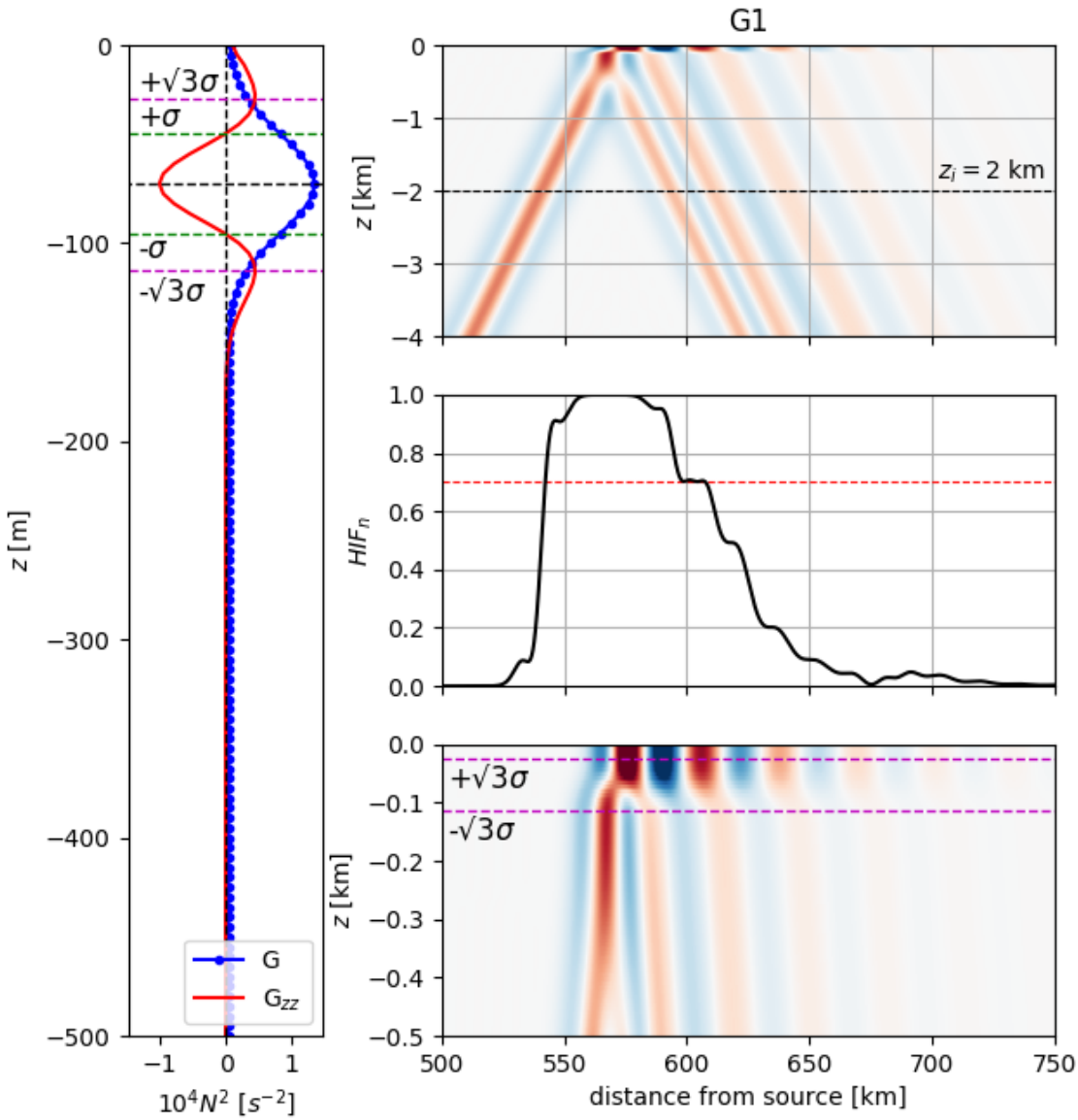

Figure 2.11: Stratification information (left panel), u-velocity (top and bottom right panels), and associated HIF curve (middle right panel) for Experiment G1. The N^2 profile G (blue) and its second derivative G_{zz} (red, not to scale) are shown in the left panel with horizontal dashed lines indicating z_{pyc} (black), +/- σ distance from z_{pyc} (green), and +/- $\sqrt{3}\sigma$ from z_{pyc} (magenta). The distance σ is shown since it is a key parameter describing the shape of the Gaussian function. The $HIF_n(x, z_i)$ plot can be used to estimate the amount of energy flux passing a certain depth z_i (2 km in this case) - the red dashed line indicates the amount of energy (normalized so that the maximum is 1) remaining above z_i after 600 km.

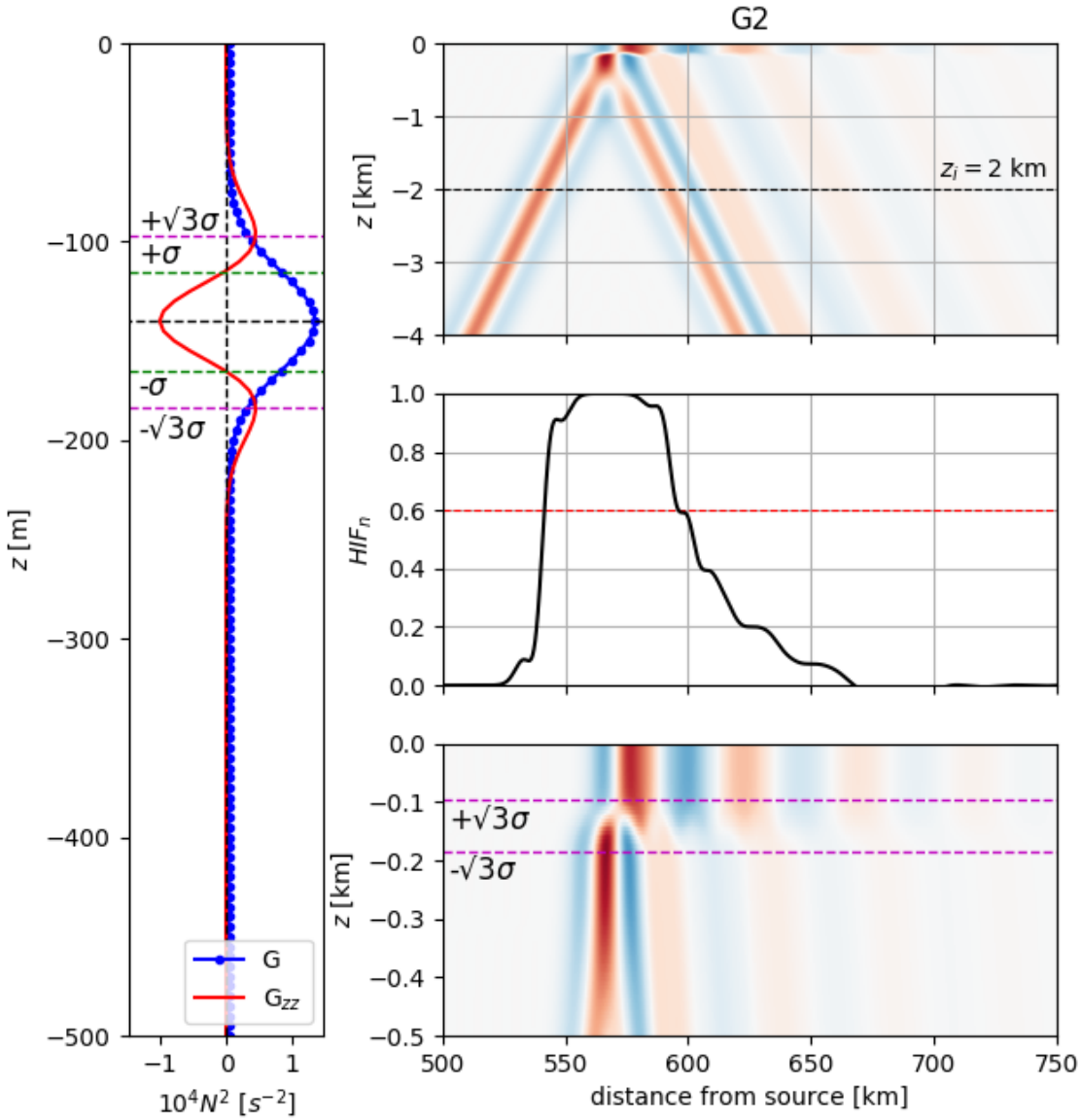

Figure 2.12: Same as Figure 2.11 except it is for Experiment G2.

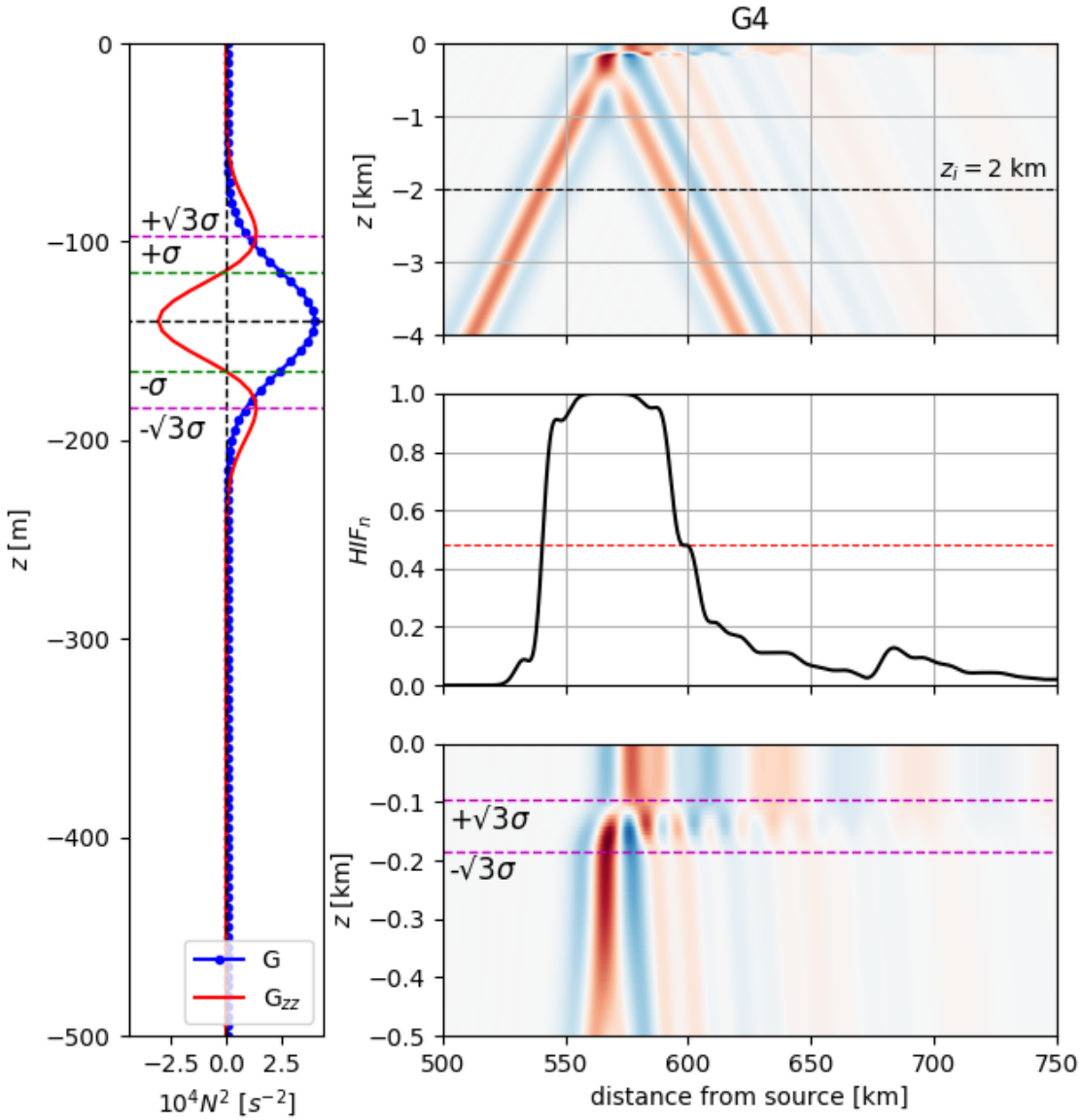

Figure 2.13: Same as Figure 2.11 except it is for Experiment G4.

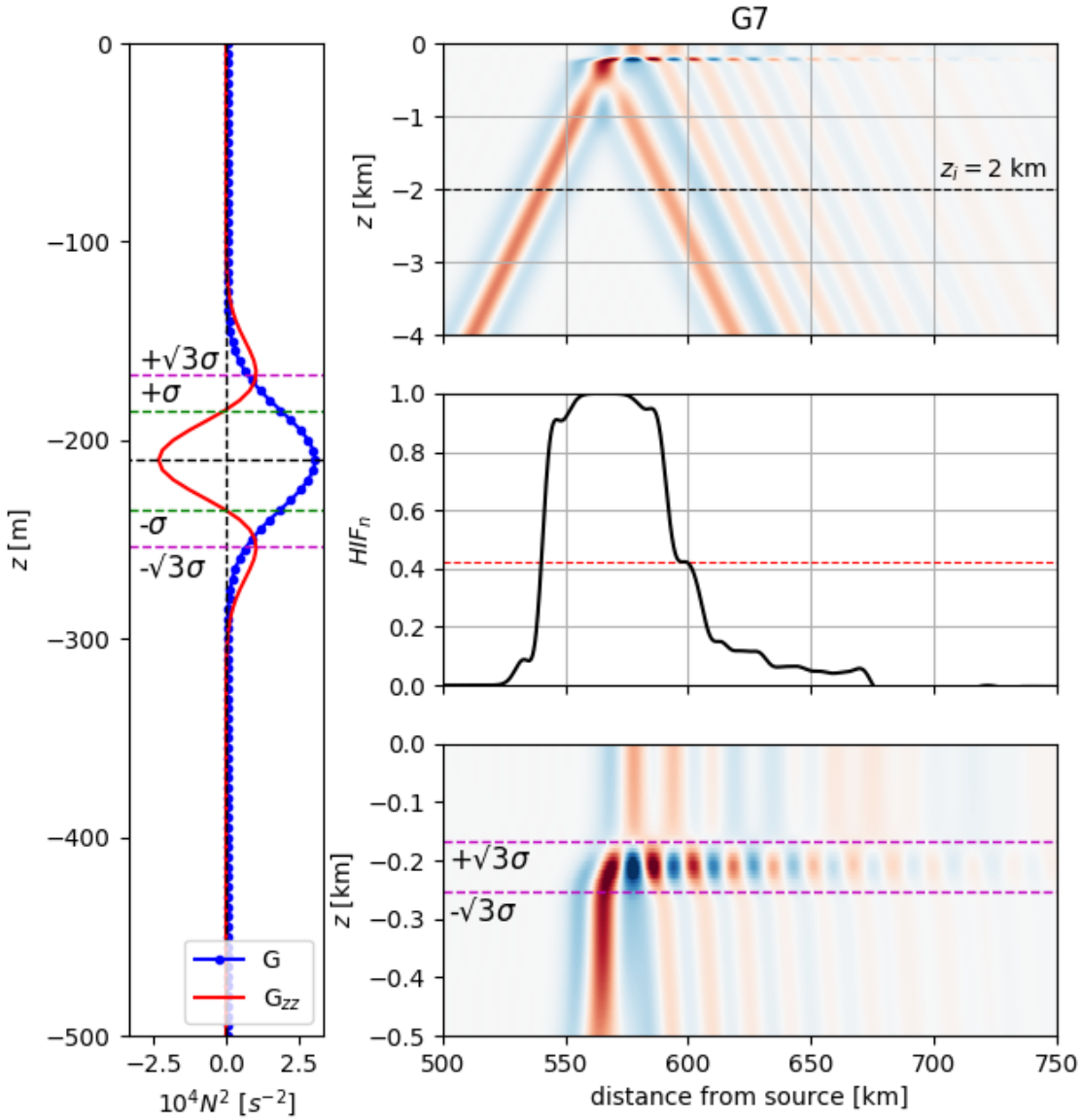

Figure 2.14: Same as Figure 2.11 except it is for Experiment G7.

G4), but it is in Regime $\mathscr{R}_2$ because its PS_2 value is less than 0.01 m s^{-2}. While the PS_2 parameter determines the type of scattering, it does not predict the amount of scattering caused by internal reflection in the pycnocline (e.g., PS_2 of Experiment G11 is more than three times that of Experiment G7, but they show the same percent reflection).

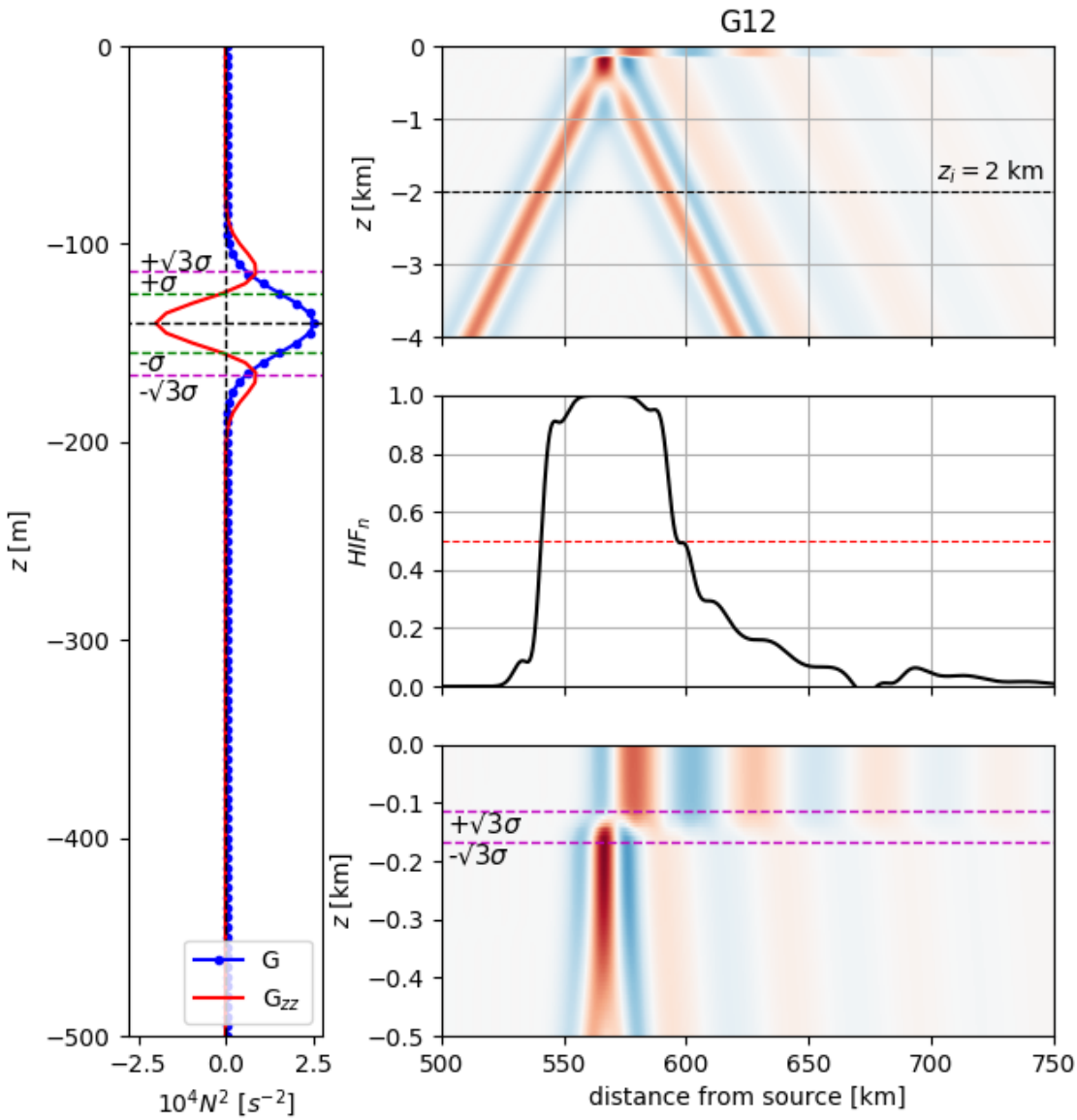

Figure 2.15: Same as Figure 2.11 except it is for Experiment G12.

2.4.3 Predicting percent reflection for Regime $\mathscr{R}_4$ scattering

Parameters for the density stratification and the internal tide beam are varied to see what controls the amount of energy reflected when the beam encounters changing stratification in the pycnocline (Table 2.5). As seen in the previous section, Regime $\mathscr{R}_4$ experiments (e.g., Experiments G7-11) show that percent reflection does not depend on the depth of the pycnocline, even though it did for Regime $\mathscr{R}_2$ experiments (e.g., Experiments G1-3). Percent reflection in Regime $\mathscr{R}_4$ experiments from Table 2.4 are all close to 58%, even though they have different A_N, z_{pyc}, and PS_2 values. For the experiments in this section, A_N will be kept at values $\geq 5.0\times10^{-4}$ s^{-2} because larger A_N values lead to greater separation of the reflected beams (by increasing the horizontal scale of the beams in the pycnocline, according to equation 2.12). This makes it easier to calculate percent reflection using the HIF curve. For example, compare Experiment G7 ($A_N = 3.0\times10^{-4}$ s^{-2}, Figure 2.14) with Experiment G11 ($A_N = 1.0\times10^{-3}$ s^{-2}, Figure 2.16).

Recall that under the WKB approximation, if N varies slowly enough over the scale of a wave, there will be full transmission of the wave and no internal reflection. Therefore, the vertical derivatives of N are important factors to consider when trying to understand and quantify internal reflection. For the Gaussian function defined in equation 2.14, the first derivative with respect to z is

$$G_z(z) = -A_N \left(\frac{z - z_{pyc}}{\sigma^2}\right) exp\left(-\frac{(z - z_{pyc})^2}{2\sigma^2}\right), \tag{2.15}$$

the second derivative is

$$G_{zz}(z) = \frac{A_N}{\sigma^2}\left(\frac{(z - z_{pyc})^2}{\sigma^2} - 1\right) exp\left(-\frac{(z - z_{pyc})^2}{2\sigma^2}\right), \tag{2.16}$$

and the third derivative is

$$G_{zzz}(z) = \frac{A_N}{\sigma^4}(z - z_{pyc})\left(3 - \frac{(z - z_{pyc})^2}{\sigma^2}\right) exp\left(-\frac{(z - z_{pyc})^2}{2\sigma^2}\right). \tag{2.17}$$

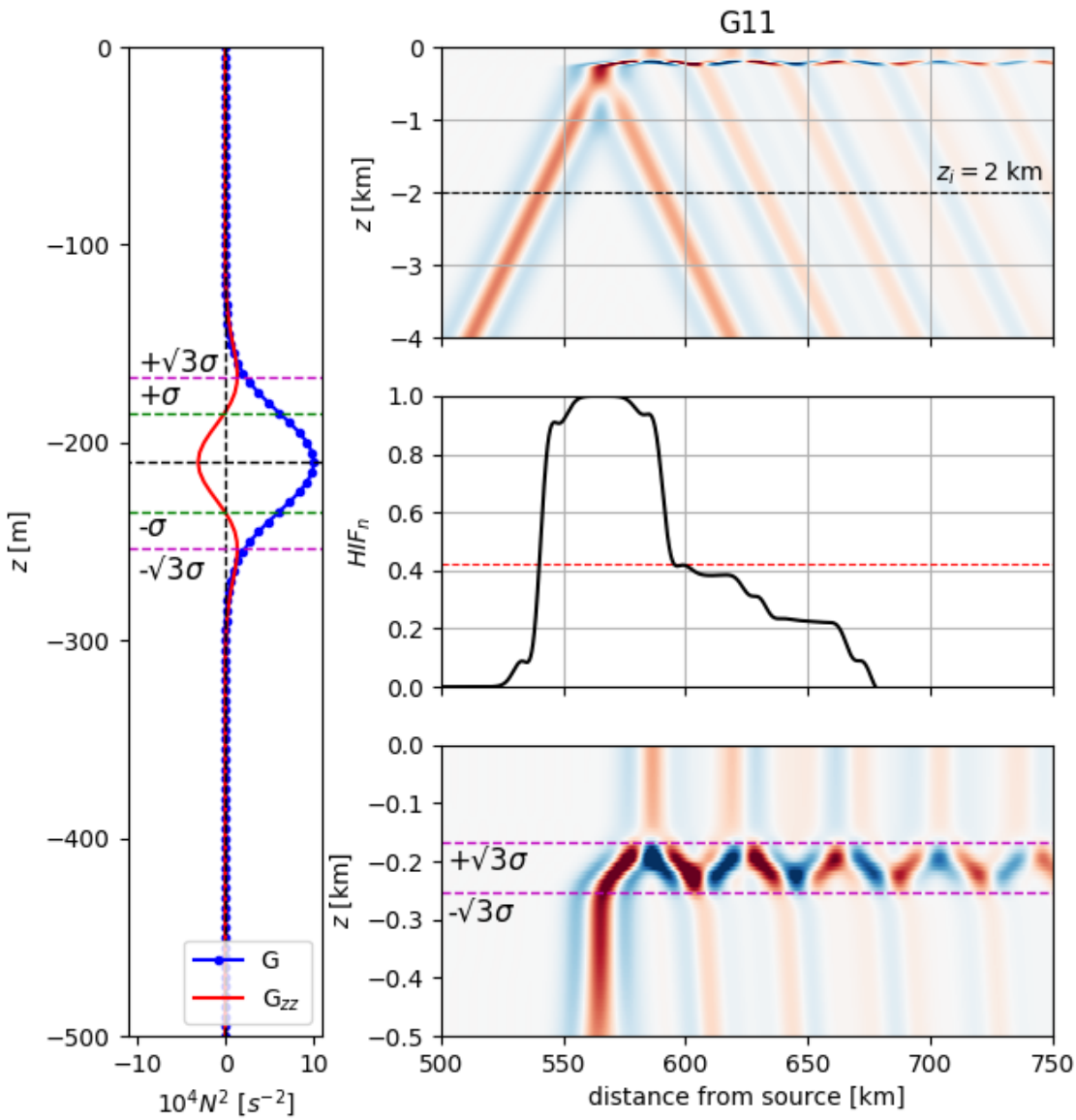

Figure 2.16: Same as Figure 2.11 except it is for Experiment G11.

By examining the internal tide beam propagation path of a Regime $\mathscr{R}_4$ experiment that shows clear refraction and reflection (Experiment G11, Figure 2.16), we hypothesize that of the three derivatives of G, curvature G_{zz} is the most important factor associated with internal reflection. Internal reflection of the beam appears to happen not at the extrema points of G_z ($z_{pyc} \pm \sigma$) but closer to the maxima of G_{zz} ($z_{pyc} \pm \sqrt{3}\sigma$), where

$$max(G_{zz}) = 2\,e^{-\frac{3}{2}}\,\frac{A_N}{\sigma^2}. \tag{2.18}$$

We expect that stronger curvature would correspond to larger percent reflection since it leads to larger deviation from the WKB approximation. Smaller σ and larger A_N both contribute to larger curvature, but these two parameters alone do not predict percent reflection, as the beam scale b_{scale} also matters. Since it is the change in N over the scale of the wave that matters (Gill, 1982), larger beam scale means more change within the beam, and therefore larger deviation from the WKB approximation. However, even when the beam scale is held constant, $max(G_{zz})$ alone is not enough to predict percent reflection. For example, Experiment G26 has larger $max(G_{zz})$ than Experiment G17 by a factor of about 2 but shows 5% less reflection (both have $b_{scale} = 400\,\mathrm{m}$).

We search for a parameter Q that is predictive of percent reflection, and propose that it should be directly proportional to $max(G_{zz})$ [$\mathrm{m}^{-2}s^{-2}$] and b_{scale} [m]. In order to be nondimensional, Q needs to have two factors of length in the numerator to balance the two factors of length in the denominator from $max(G_{zz})$, so we include two factors of b_{scale} in the numerator. We find that $\sqrt{A_N}$ predicts better than A_N, so we include a factor of $\sqrt{A_N}$ in the numerator. We propose the nondimensional parameter

$$Q = c_0 \frac{max(G_{zz})\,b_{scale}^2}{\sqrt{A_N}\,N_{min}} = 2\,e^{-\frac{3}{2}}\,c_0\,\frac{\sqrt{A_N}\,b_{scale}^2}{N_{min}\,\sigma^2}, \tag{2.19}$$

where $c_0 = \sqrt{4 \times 10^{-3}}$ is an arbitrary constant. We find that Q has the strongest predictive power for percent reflection when compared to other relevant parameters.

For the experiments in Table 2.5, Q is the only variable that has strong correlation with percent reflection, decreasing monotonically as percent reflection does the same. As Q ranges from 2.4 to

173, percent reflection ranges from 13% to 70%. The relationship is not linear, and small changes in Q do not always correspond to changes in percent reflection (e.g., Q values for Experiments G19 and G26 differ by 2 but percent reflection is the same). With respect to where reflection occurs, Experiment G11 (Figure 2.16) is an example of internal reflections occurring between $\pm\sqrt{3}\sigma$ of z_{pyc}, while Experiment G20 (Figure 2.17) is an example of the reflections occurring slightly farther away from z_{pyc}. Although pycnocline ducting does not seem strictly bounded by $z_{pyc} \pm \sqrt{3}\sigma$, where the curvature of N is at a maximum, it does seem that $max(G_{zz})$ is an important quantity in predicting percent reflection and therefore their locations are also important.

Table 2.5: Parameters for Gaussian stratification experiments in Regime $\mathscr{R}_4$ are listed. The number of modes used in calculations range from 125 (for $b_{scale} = 400$) to 300 (for $b_{scale} = 150$). PR stands for percent reflection. Q is the parameter described in the text, rounded to 2 significant digits; it has the strongest predictive power for percent reflection when compared to other parameters listed in the table. $N_{min} = 2\times10^{-3}s^{-1}$ except for the v2* experiments where $N_{min} = 1\times10^{-3}s^{-1}$.

PR	Q	z_{pyc} [m]	σ [m]	A_N [s^{-2}]	b_{scale} [m]	max(G_{zz}) [m^{-2}s^{-2}]	name
70	173	-250	25	1.0×10^{-2}	400	6.8×10^{-6}	G101
58	110	-140	25	1.0×10^{-3}	400	6.8×10^{-7}	G10
58	110	-210	25	1.0×10^{-3}	400	6.8×10^{-7}	G11
58	110	-250	25	1.0×10^{-3}	400	6.8×10^{-7}	G14
57	80	-250	35	5.0×10^{-4}	400	1.8×10^{-7}	G16v2*
57	69	-250	40	1.0×10^{-3}	500	2.7×10^{-7}	G27
54	57	-250	35	1.0×10^{-3}	400	3.6×10^{-7}	G15
51	40	-250	35	5.0×10^{-4}	400	1.8×10^{-7}	G16
48	40	-250	50	5.0×10^{-4}	400	8.8×10^{-8}	G17v2*
45	28	-250	50	1.0×10^{-3}	400	1.8×10^{-7}	G18
42	20	-250	50	5.0×10^{-4}	400	8.8×10^{-8}	G17
37	18	-250	75	2.0×10^{-3}	400	1.6×10^{-7}	G26
37	16	-250	50	1.0×10^{-3}	300	1.8×10^{-7}	G19
32	11	-250	60	1.0×10^{-3}	300	1.2×10^{-7}	G20
30	10	-250	75	1.0×10^{-3}	350	7.9×10^{-8}	G21
24	6.0	-250	75	1.0×10^{-3}	270	7.9×10^{-8}	G22
22	4.9	-250	60	1.0×10^{-3}	200	1.2×10^{-7}	G23
16	3.2	-250	75	1.0×10^{-3}	200	7.9×10^{-8}	G24
13	2.4	-250	65	1.0×10^{-3}	150	1.0×10^{-7}	G25

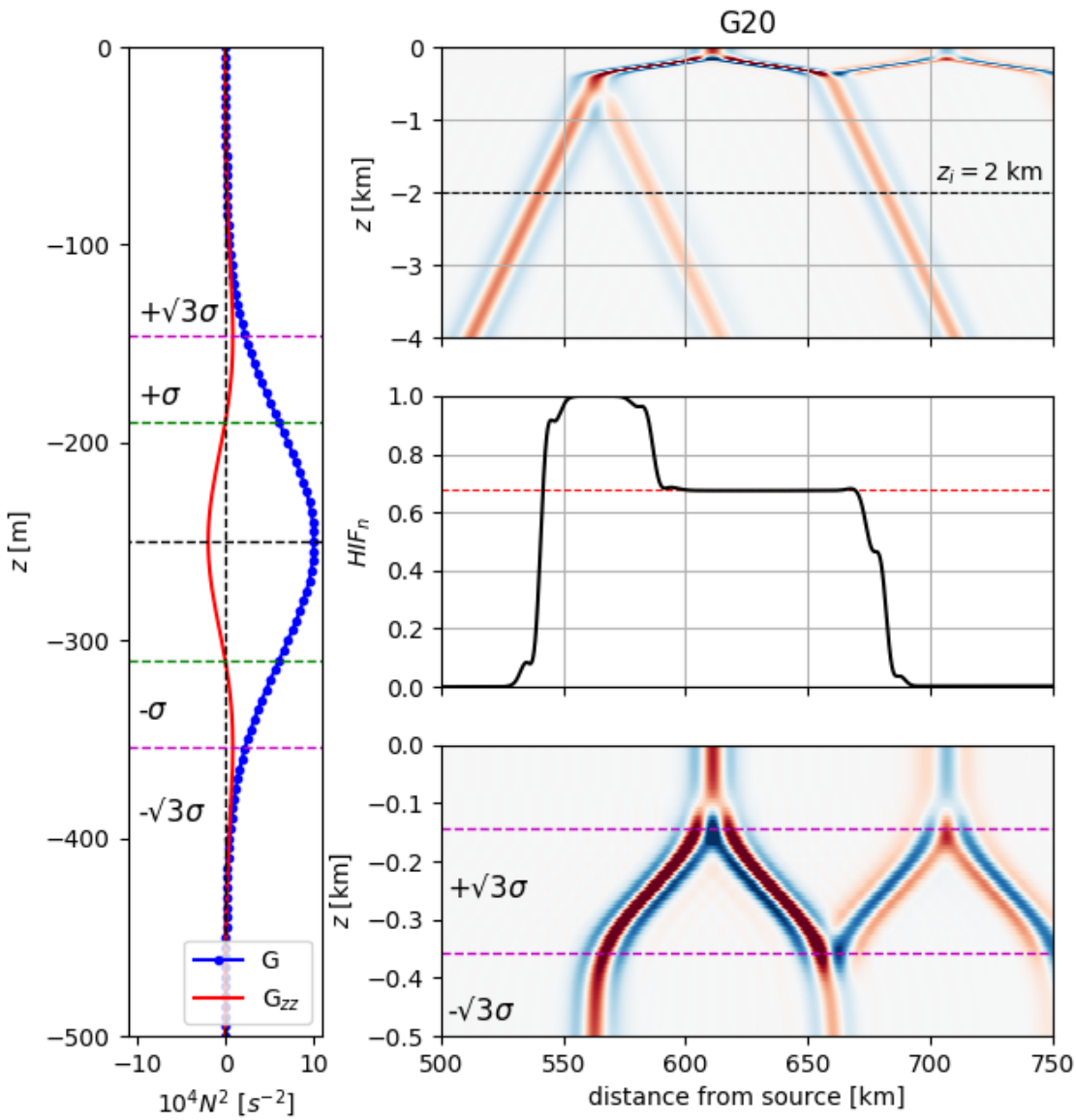

Figure 2.17: Same as Figure 2.11 except it is for Experiment G20.

2.5 Summary and Discussion

The linear scattering of internal tide beams, characterized by spreading of energy due to internal reflection and refraction, can result in decreased beam energy density and the horizontal ducting of beam energy. A previous study on scattering by Gerkema (2001) is reproduced and extended using a numerical model based on solving for vertical normal modes. A measure of the strength of the pycnocline, based on the vertical integral of the $N^2(z)$ profile, was proposed by Gerkema (2001) to separate experiments into three regimes. The case of an moderate strength pycnocline, Regime $\mathscr{R}_2$, was found to exhibit scattering of beam energy. These results are reproduced and a fourth regime ($\mathscr{R}_4$) characterized by a strong pycnocline and ducting of energy in the pycnocline layer is identified.

In the moderately developed pycnocline case (Regime $\mathscr{R}_2$), internal tide beam energy enters the top layer where the stratification is either weak or absent, and appears to be ducted, propagating horizontally and with energy leaking downward in the form of beams. The horizontal length scale of wave energy in the top layer increases with increased depth of the pycnocline. In Regime $\mathscr{R}_4$, energy is stronger in the pycnocline layer than in the top layer, and ducting appears to be a result of internal reflection within the pycnocline, approximately bounded within $z_{pyc} \pm \sqrt{3}\boldsymbol{\sigma}$. The degree of scattering is associated with the percentage of energy reflected when the beam encounters the maximum curvature of the N^2 profile at $z_{pyc} \pm \sqrt{3}\boldsymbol{\sigma}$. A non-dimensional parameter Q based on $max(G_{zz})$, $max(N^2)$, N_{min}, and the width scale of the beam is identified and found to be a strong predictor of how much energy is reflected and scattered in Regime $\mathscr{R}_4$.

Horizontal ducting in the pycnocline layer causes beam energy to spend more time in highly stratified regions, where vertical scales are compressed. While this compression effect could lead to increased dissipation (because smaller scales are more easily dissipated) and possible increased nonlinear transformations (as observed and modeled by Gayen & Sarkar (2013, 2014), Xie et al. (2011)), decreased beam energy density also implies less nonlinearity due to decreased amplitude. Studies using a nonlinear model that can simulate dissipation are needed.

While the HOT profile has the basic shape of a realistic stratification profile, it is averaged over

ten years of data and therefore missing small scale features that would be present in shorter term (∼hours) observations. Preliminary experiments using realistic single cast stratification profiles from Hawaii show that in addition to the main pycnocline, smaller amplitude and vertical scale variations in the stratification profile can also lead to scattering and spreading of the beam. This can be missed by numerical models which do not have sufficient resolution to resolve small scale features in N.

We find that inadequate resolution can also lead to spurious scattering and defocusing of the beam (Figure 2.18). Using the Massachusetts Institute of Technology General Circulation Model (MITgcm) to run two almost identical simulations using the HOT stratification profile, we found that uniform vertical resolution of $dz = 20\,\mathrm{m}$ can cause spurious scattering of an internal tide beam as it transits through the pycnocline. The MITgcm is capable of modeling nonlinear and nonhydrostatic dynamics but velocity amplitudes were kept low in these simulations to avoid nonlinearity and including nonhydrostatic terms did not make a difference. The MITgcm simulation with $dz = 5\,\mathrm{m}$ and viscosity and diffusivity values of $5\times10^{-4}\,\mathrm{m^2\,s^{-1}}$ and $5\times10^{-5}\,\mathrm{m^2\,s^{-1}}$, respectively, was found to be identical to a LIMM simulation with $dz = 2\,\mathrm{m}$.

Since running a time-stepping numerical model at high resolution is costly, we used LIMM to identify configurations that would be interesting for future examination with more sophisticated models. Building upon this study to better understand the effects of scattering in a linear regime, by considering energy dissipation and small scale changes in stratification, will contribute to more realistic simulations of nonlinear and nonhydrostatic processes.

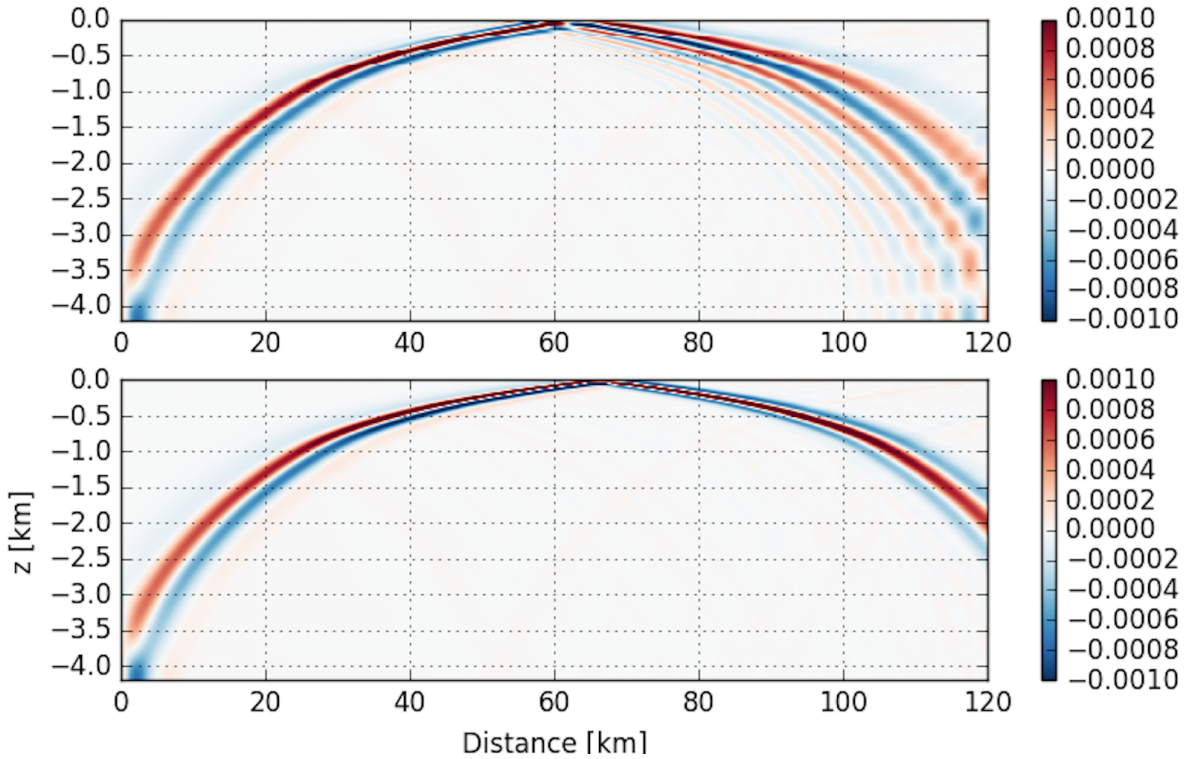

Figure 2.18: Snapshots of horizontal velocity [ms^{-1}] for two MITgcm experiments which are identical except for vertical resolution. Upper panel shows spurious scattering of a reflected beam due to insufficient vertical resolution ($dz = 20\,\mathrm{m}$), and the lower panel shows a simulation with $dz = 5\,\mathrm{m}$ which agrees with output from an analytical model with $dz = 2\,\mathrm{m}$.

CHAPTER 3

Latitude dependence of the fate of internal tide beams

3.1 Introduction

Mechanical energy capable of causing diapycnal mixing in the ocean is transferred to the internal wave field when barotropic tides pass over underwater topography and generate internal tides. The resulting internal tide energy is initially confined in vertically confined envelopes, or beams. These internal tide beams (ITB) are ubiquitous in the ocean (Dauxois et al., 2018) and have been observed in numerous locations (Martin et al., 2006, Cole et al., 2009, Johnston et al., 2011, Waterhouse et al., 2018). As ITBs propagate through regions of non-uniform stratification in the upper ocean, wave energy can be transferred to non-tidal frequencies through different nonlinear processes (Gerkema, 2001, Grisouard & Staquet, 2010, Mercier et al., 2012, Gayen & Sarkar, 2013, 2014). Observations have shown that in several cases, ITBs are no longer detectable in horizontal kinetic energy beyond the first surface reflection (Martin et al., 2006, Pickering & Alford, 2012). Importantly, this implies that some of the internal tide kinetic energy no longer propagates into the abyssal ocean and consequently will not be available to maintain the global ocean's density stratification.

Numerical and laboratory studies show that as ITBs propagate up through the pycnocline, wave energy can be scattered as well as transferred to non-tidal frequencies through various nonlinear processes such as the generation of internal solitary waves (ISW), induced-mean flows, and M_2 harmonics and subharmonics (Grisouard & Staquet, 2010, Grisouard et al., 2011, Mercier et al., 2012, Xie et al., 2013b,a, Gayen & Sarkar, 2014). A wave beam can scatter through internal refraction and reflection, an essentially linear process, and disturbances of the isopycnals in the pycnocline can grow and evolve into ISWs (Gerkema, 2001, Akylas et al., 2007). Solitary waves have been widely observed (Jackson & Apel, 2004, Jackson, 2007, 2009) and are mainly generated by the barotropic tide, interacting with prominent topographies in coastal regions (Apel, 2002, Cai et al., 2012, Lien et al., 2014). In the open ocean, ISWs can be generated by an ITB impinging upon the pycnocline from below, a process referred to as "local generation" (New & Pingree, 1990). It has been suggested that in the Bay of Biscay, ITBs have not been observed after their surface reflection because their energy has been converted into both ISWs and mixing (New & Pingree, 1990, New & Da Silva, 2002).

Triadic resonant instability (TRI; Dauxois et al., 2018), of which the parametric subharmonic instability (PSI) is a special case, can cause ITB degradation as the beam propagates from its generation site up to the surface (Gayen & Sarkar, 2013). TRI is a weakly nonlinear wave-wave interaction that can transfer energy from a primary wave to secondary waves of much smaller scales (McComas & Bretherton, 1977). It is regarded as a potentially efficient mechanism to transfer energy directly from large to small vertical scales (Koudella & Staquet, 2006), possibly serving as an important link between barotropic tides and turbulent mixing (Hibiya et al., 2002, Furuichi et al., 2005, Xie et al., 2011). The diagram in Figure 3.1 shows one of the conditions of TRI, that the wave vectors of the primary and two secondary waves have to add up. The other condition is that the frequencies of the secondary waves have to add up to the frequency of the primary wave. In general, there can be a continuum of frequencies for TRI secondary waves (Korobov & Lamb, 2008).

Energy transfer from the large-scale semi-diurnal tide M_2 to small-scale oscillations at sub-M_2 frequencies can occur for a range of latitudes equatorward of 28.8° (Hibiya & Nagasawa, 2004, Gerkema et al., 2006), the so called M_2 subharmonic "critical latitude" (CL) where the inertial frequency

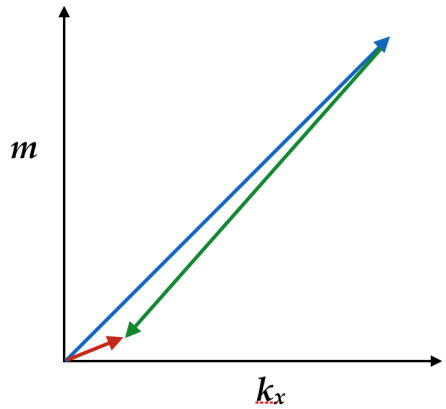

Figure 3.1: Wave vector diagram for TRI. The red vector represents the primary wave, and the green and blue vectors represent the secondary waves. The vertical wavenumber is m, and the horizontal wavenumber is k_x.

equals $\frac{1}{2}M_2$. Many studies show that TRI is most effective as an energy transfer mechanism at the CL, and its efficiency drops off equatorward (MacKinnon & Winters, 2005, Alford et al., 2007, MacKinnon et al., 2013a). Studies around the Kauai Channel (Carter & Gregg, 2006, Rainville & Pinkel, 006a, Sun & Pinkel, 2013) and the Luzon Strait (Xie et al., 2011, Liao et al., 2012) have inferred from observations that TRI is a possible mechanism of nonlinear energy transfer at latitudes as low as 21°. The locally horizontal component of the Coriolis parameter can shift the CL poleward by up to a few degrees, and this could have dynamical consequences for TRI and implications for tidal dissipation (Gerkema & Shrira, 2005, Gerkema et al., 2006). Richet et al. (2017) found that the Doppler shift of M_2 due to large scale currents can also move the CL poleward, by as much as 6°. Additionally, currents such as geostrophic background flow change the local effective Coriolis frequency, and can have important implications for the spatial distribution of TRI (Yang et al., 2018, Dong et al., 2019).

Equatorward of the CL, where secondary waves propagate freely, there is no general consensus about which frequencies are preferred by TRI. Observational (Xie et al., 2011) and numerical (Nikurashin & Legg, 2011) studies found that M_2-forced secondary waves can have frequencies separated by as much as 0.5 cycles per day, or 0.26 M_2, at latitudes near 21°. Analytical (Staquet & Sommeria, 2002) and numerical (Hazewinkel & Winters, 2011) studies found that TRI growth rates

are at a maximum when the secondary wave frequencies approach equality. It is commonly thought that poleward of the CL, secondary wave frequencies are outside of the internal wave frequency range and so TRI cannot be active (Nikurashin & Legg, 2011). However, Richet et al. (2018) suggest that transfers of energy to non-propagating evansecent waves poleward of the CL can actually be an efficient mechanism for dissipating internal tide energy. When the frequency of at least one of the two secondary waves are outside of the internal wave band, what results is a forced wave instead of a progressive wave, and the instability can no longer be a resonant triad. However, energy can still be transferred through non-resonant triad interactions, and possibly the impact of forced, or trapped, waves on mixing are even greater because energy can build up more quickly in trapped waves, which are then more likely to overturn (Korobov & Lamb, 2008).

We present an idealized latitudinal study of nonlinear energy transfers using a configuration from Grisouard and Staquet (2010; hereafter GS10), which produces ISWs through the local generation mechanism, as a basis for comparison. A wave beam propagating up to the sea surface is simulated in order to examine the transfers of ITB energy to other frequencies for different latitudes. Two different realistic stratification profiles are tested, one from the Bay of Biscay which is representative of mid-latitudes, and another from Hawaii which is representative of tropical latitudes. The two profiles are almost identical below 1000 m depth, but above that they are different in that the mid-latitude profile has a permanent pycnocline around 800 m depth and a much sharper seasonal pycnocline. Maximum N is again almost the same for the two profiles, but the change in N with depth is a lot more gradual in the Hawaii profile. We examine simulations for a range of latitudes using each profile in order to isolate the effects due to rotation alone, even if the stratification used might not be representative of conditions at those latitudes. Using the Bay of Biscay profile we find that there is generation of ISWs at various latitudes from 0-60°N, but that ISW amplitudes are diminished or absent when TRI are present. Using the profile from Hawaii we do not see any indication of solitary waves for latitudes from 0-50°N. Both sets of experiments show transfers of energy to subharmonic frequencies which suggest the presence of TRI.

The numerical set-up and parameters of the experiments are described in section 2. The results

for the Bay of Biscay stratification experiments are shown in section 3, and the results for the Hawaii stratification experiments are shown in section 4. Quantitative measures of nonlinear energy transfers for both sets of experiments are presented in section 5. Summary and discussion of the results, open questions, and limitations of the study are presented in section 6.

3.2 Methods

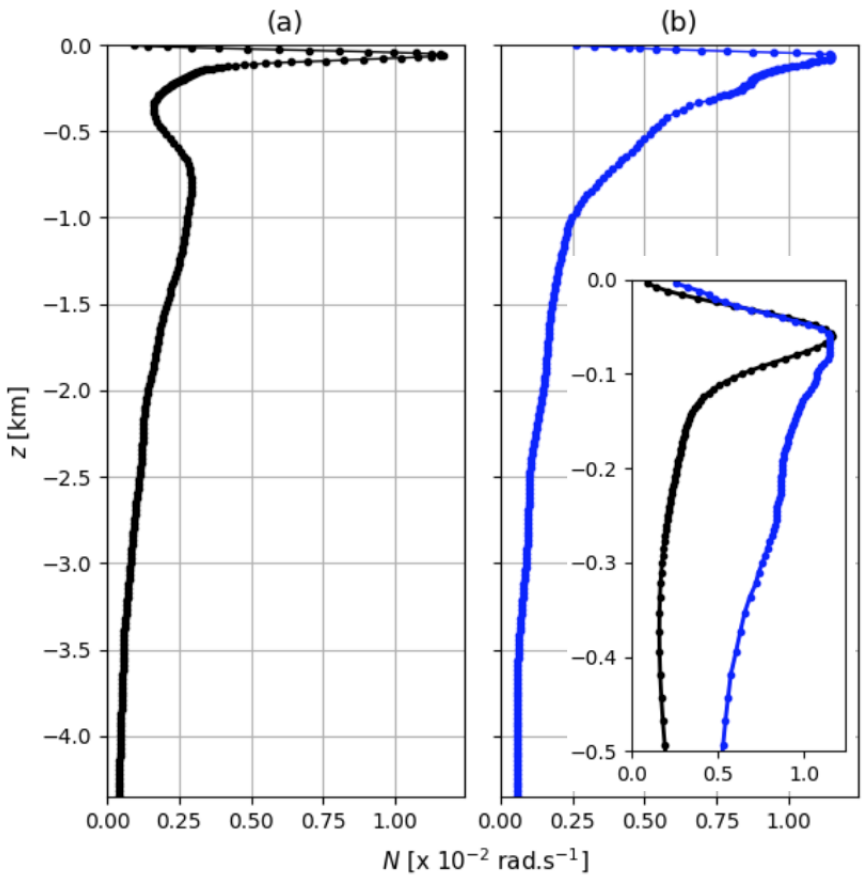

Figure 3.2: Buoyancy frequency $N(z)$ for the experiments in this study are based on density stratification profiles that are representative of a) the Bay of Biscay at 45°N and b) Hawaii at 22.75°N. Inset shows both stratification profiles down to 500 m depth.

We use the Massachusetts Institute of Technology general circulation model (MIT-gcm, checkpoint

c65i), a finite-volume, nonlinear, nonhydrostatic numerical model that solves the equations of motion using the Boussinesq approximation (Marshall et al., 1997). The numerical set-up used in this study is nearly identical to experiment E2 of GS10, except for changes to the Coriolis frequency and in the stratification profile used in the different experiments (Table 3.1). The domain of the numerical experiments is a two-dimensional rectangular region that is 4355 m deep and 200 km wide. As in GS10, the adjective "horizontal" will refer to the x direction, and u is the velocity in this direction. The x-grid is variable with spacing ranging from 50-180 m, and the transition is centered at 156 km. This was done to reduce computation cost without losing horizontal resolution where it is important. The variable $x-$grid is set up in the same way as the variable z-grid, which is described in GS10. The variable z-grid has spacing ranging from 4-25 m, and the transition is centered around 330 m depth. The grid size is $3360 \times 1 \times 234$ points. Higher vertical resolution, with vertical spacing less than or equal to 5 m throughout the water column (887 layers), was tested and resulted in no noticeable changes. Other differences from GS10 in the set-up include turning off the nonlocal K-Profile Parameterization (KPP) scheme of Large et al. (1994), decreasing the time-step to 11.18 s, and increasing the viscosity and diffusivity to $5 \times 10^{-4}\,\mathrm{m^4\,s^{-1}}$ and $5 \times 10^{-5}\,\mathrm{m^4\,s^{-1}}$, respectively. Biharmonic viscosity and diffusivity were both decreased to be $3 \times 10^{2}\,\mathrm{m^4\,s^{-1}}$.

Two different stratification conditions, or buoyancy frequency profiles $N(z)$, were used in the numerical experiments (Figure 3.2). One is representative of the Bay of Biscay (BB) in late spring, the same as in GS10 E2, and another is a 10-year average of data from Station ALOHA of the Hawaii Ocean Time-series (HOT) program (Karl & Lukas, 1996). The maximum for the N profile, or the center of the pycnocline h_p, occurs at 58 m for the BB profile, and at 72 m for the HOT profile. The wave beam originates from the left boundary of the domain, centered at 2155 m depth, and propagates to the right. The analytical expression of the forcing envelope is based on the profile of an internal wave beam in a rotating fluid of constant N, as described in GS10. The amplitude of the wave beam is $12\,\mathrm{cm\,s^{-1}}$, and its vertical wavenumber m (in cycles per meter) is $1/L_z$, where $L_z = 1500\,\mathrm{m}$. The forcing frequency is that of the M_2 tide, i.e. $\omega_0 = 1.405 \times 10^{-4}\,\mathrm{s^{-1}}$. A sponge layer is implemented in the right boundary beginning at 150 km.

Table 3.1: Experiments are named by the stratification profile used (BB for Bay of Biscay, and HOT for Station ALOHA) and their approximate latitude; f is the Coriolis frequency, and t_s is the time it takes the forcing beam to reach the surface, in units of $T_0 = 2\pi/\omega_0$, the wave period of M_2. Two time intervals are specified, R_1: $3t_s$ to $3t_s + 10\,T_0$, and R_2: $3t_s + 15\,T_0$ to $3t_s + 25\,T_0$ (times are rounded down to the nearest integer multiple of T_0).

Experiment	latitude [°N]	f [s^{-1}]	t_s [T_0]	R_1 [T_0]	R_2 [T_0]
BB0	0	0	1.45	4-14	19-29
BB05	5	1.27×10^{-5}	1.46	4-14	19-29
BB10	10	2.53×10^{-5}	1.49	4-14	19-29
BB15	15	3.76×10^{-5}	1.56	4-14	19-29
BB20	20	4.97×10^{-5}	1.65	4-14	19-29
BB25	25	6.15×10^{-5}	1.79	5-15	20-30
BB29	29	7.03×10^{-5}	1.93	5-15	20-30
BB35	35	8.34×10^{-5}	2.23	6-16	21-31
BB40	40	9.35×10^{-5}	2.59	7-17	22-32
BB45 (GS10 E2)	45	1.03×10^{-4}	3.11	9-19	24-34
BB50	50	1.11×10^{-4}	3.89	11-21	26-36
BB55	55	1.19×10^{-4}	5.14	15-25	30-40
BB60	60	1.26×10^{-4}	7.35	22-32	37-47
HOT0	0	0	1.45	4-14	19-29
HOT05	5	1.27×10^{-5}	1.46	4-14	19-29
HOT10	10	2.53×10^{-5}	1.50	4-14	19-29
HOT15	15	3.76×10^{-5}	1.56	4-14	19-29
HOT20	20	4.97×10^{-5}	1.63	4-14	19-29
HOT25	25	6.15×10^{-5}	1.76	5-15	20-30
HOT29	29	7.03×10^{-5}	1.91	5-15	20-30
HOT35	35	8.34×10^{-5}	2.20	6-16	21-31
HOT40	40	9.35×10^{-5}	2.59	7-17	22-32
HOT45	45	1.03×10^{-4}	3.08	9-19	24-34
HOT50	50	1.11×10^{-4}	3.89	11-21	26-36

An important part of our analysis is the use of t_s, the time it takes the forcing beam energy to reach the surface, and time intervals R_1 and R_2 (Table 3.1) to compare simulations for different latitudes. We calculate t_s by dividing the vertical distance the beam needs to travel to reach the surface by the vertical group velocity of the wave, which is a function of z. Although the Wentzel-Kramers-Brillouin (WKB) approximation does not hold in the pycnocline, we use it here because the derived expressions are sufficiently accurate for our purpose. Using the dispersion relation for internal gravity waves and making the WKB approximation, the vertical group velocity is:

$$c_{gz}(z) = \frac{N(z)^2 k_x^2}{m(z)^3 \sqrt{f^2 + N(z)^2 k_x^2 / m(z)^2}} \tag{3.1}$$

(Pearson-Potts, 2019), where we deduce the horizontal wavenumber k_x using the internal wave dispersion relation:

$$k_x = m(z) \sqrt{\frac{\omega_0^2 - f^2}{N(z)^2 - \omega_0^2}}. \tag{3.2}$$

We calculate the z-dependent time increments $dt(z) = dz(z)/c_{gz}(z)$ as z goes from -2155 m (the center of the beam) to 0 along the z-grid, and the total time to surface is the vertical integral (sum). The wave characteristic of an ITB is calculated with ray tracing using the above dispersion relation, and used to determine the horizontal location of the surface reflection.

We save the model output every $T_0/20$, which means that frequency Power Spectral Densities (PSD), calculated with a periodogram with no additional windowing or smoothing, have a frequency range from 0 to $10\,\omega_0$. Using time intervals of $10\,T_0$, the frequency difference between adjacent points in PSDs is $(10\,T_0)^{-1}$. For wavenumber PSDs, we first average horizontal velocities in x, from 20-25 km, then apply WKB stretching following Leaman & Sanford (1975) to correct for changes attributable to changes in N. We then interpolate the velocities and z coordinates to a uniform vertical grid of 10 m spacing. Again using a periodogram with no additional windowing, we calculate PSDs that have wavenumbers ranging from 0 to 0.5 cycles per meter (cpm).

3.3 Bay of Biscay stratification experiments

3.3.1 Pycnocline displacements and ITB degradation

We choose experiment E2 from GS10 (BB45 in Table 3.1) as a basis for comparison. Using a realistic stratification profile representative of Bay of Biscay conditions (Figure 3.2a), we replicate the local generation of ISWs by an upward propagating ITB impinging on the pycnocline from below at a latitude of 45°N. The snapshots of isopycnals and u-velocity for experiment E2 at both $5t_s$ and $10t_s$ (top two rows of Figure 3.3) are very similar, suggesting that at 45°N the simulation has reached a steady state after $5t_s$. Near the M_2 subharmonic critical latitude at 29°N, the ITB causes large pycnocline displacements that propagate to the right at $5t_s$, but by $10t_s$ the beam is severely degraded by what looks to be the transfer of energy to lower frequency waves of smaller vertical scale (middle two rows of Figure 3.3). There is no longer a strong disturbance to the pycnocline at the expected surface reflection location at $10t_s$, nor indications of a reflected downward propagating beam. At 15°N, the beam appears intact and interfacial waves are generated at $5t_s$, but by $10t_s$ there is a lot of small scale noise in the isopycnal displacements, and the beam is again defocused by the appearance of lower frequency waves which have flatter characteristics (bottom two rows of Figure 3.3).

The presence of TRI is one possible explanation for the appearance of lower frequency waves and the resultant degradation of the ITB. We will later examine both frequency and wave number spectra to see if the conditions of TRI are met. For now, we identify banded structures that intersect the main beam, whose direction corresponds to M_2 subharmonic waves (i.e., any wave of frequency lower than M_2 and not limited to $\frac{1}{2}M_2$), as candidates for TRI secondary waves. Following Gerkema et al. (2006), we interpret the bands as troughs and crests of secondary wave beams. TRI secondary waves at 29°N have characteristics that are horizontal, as expected for waves of frequency $\omega = \frac{1}{2}M_2 = f$. At latitudes poleward of 45°N, there are no signs of TRI secondary waves and the simulations appear relatively stationary after $5t_s$ (Figure 3.4). Disturbances to the pycnocline propagate horizontally toward the

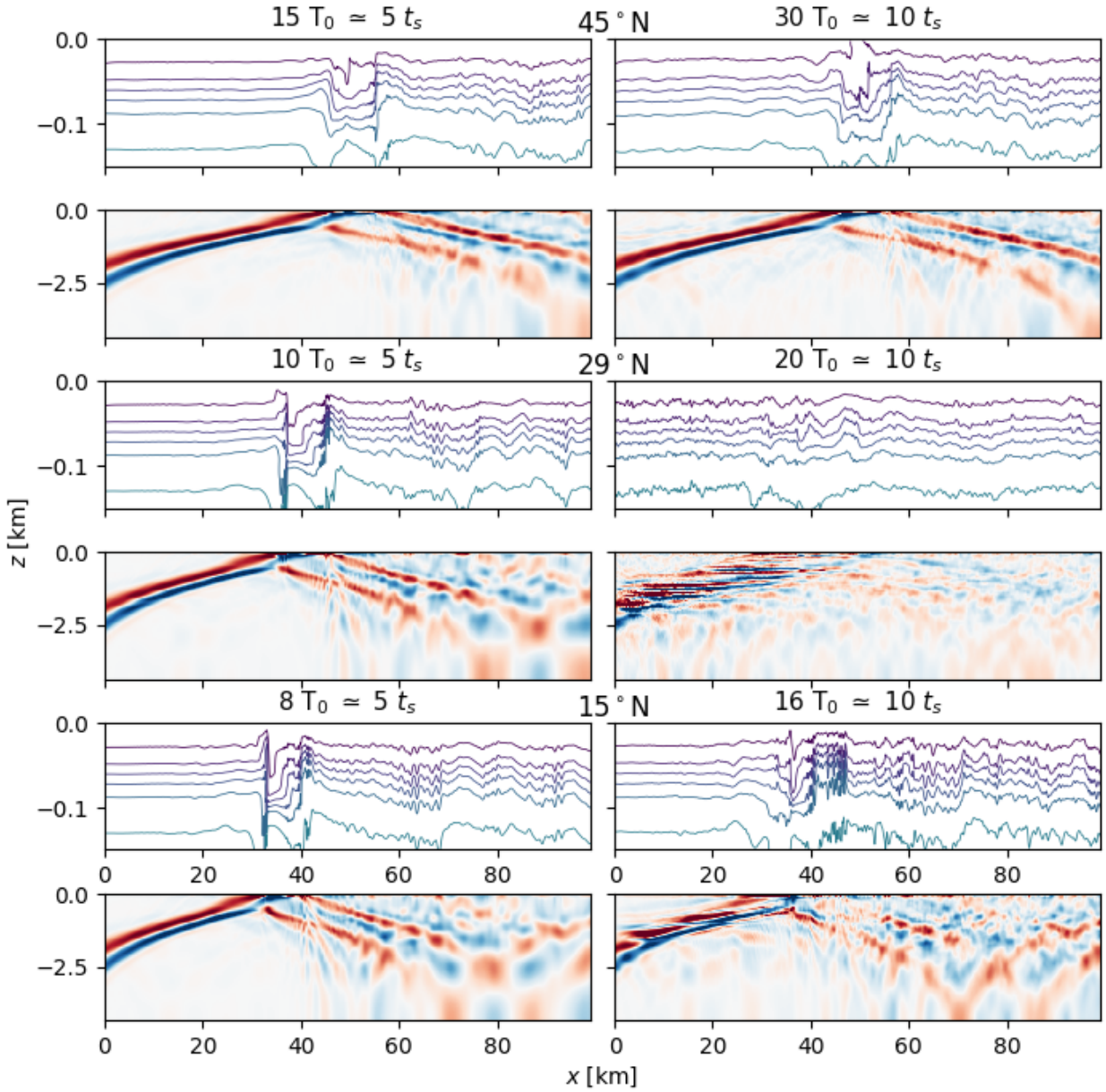

Figure 3.3: Snapshots of isopycnals and u-velocity (the color scale ranges from -0.12 to 0.12 $\mathrm{m\,s^{-1}}$) are shown for two different times: $5\,t_s$ (left column) and $10\,t_s$ (right column), and three different latitudes: 45°N (top two rows), 29°N (middle two rows), and 15°N (bottom two rows).

right edge of the domain, and there are wave trains of large amplitude and high frequency, especially at $5\,t_s$ for 55°N. Interfacial wave amplitudes appear to decrease with time for 50°N and 55°N, possibly due to the increase of higher frequency motions.

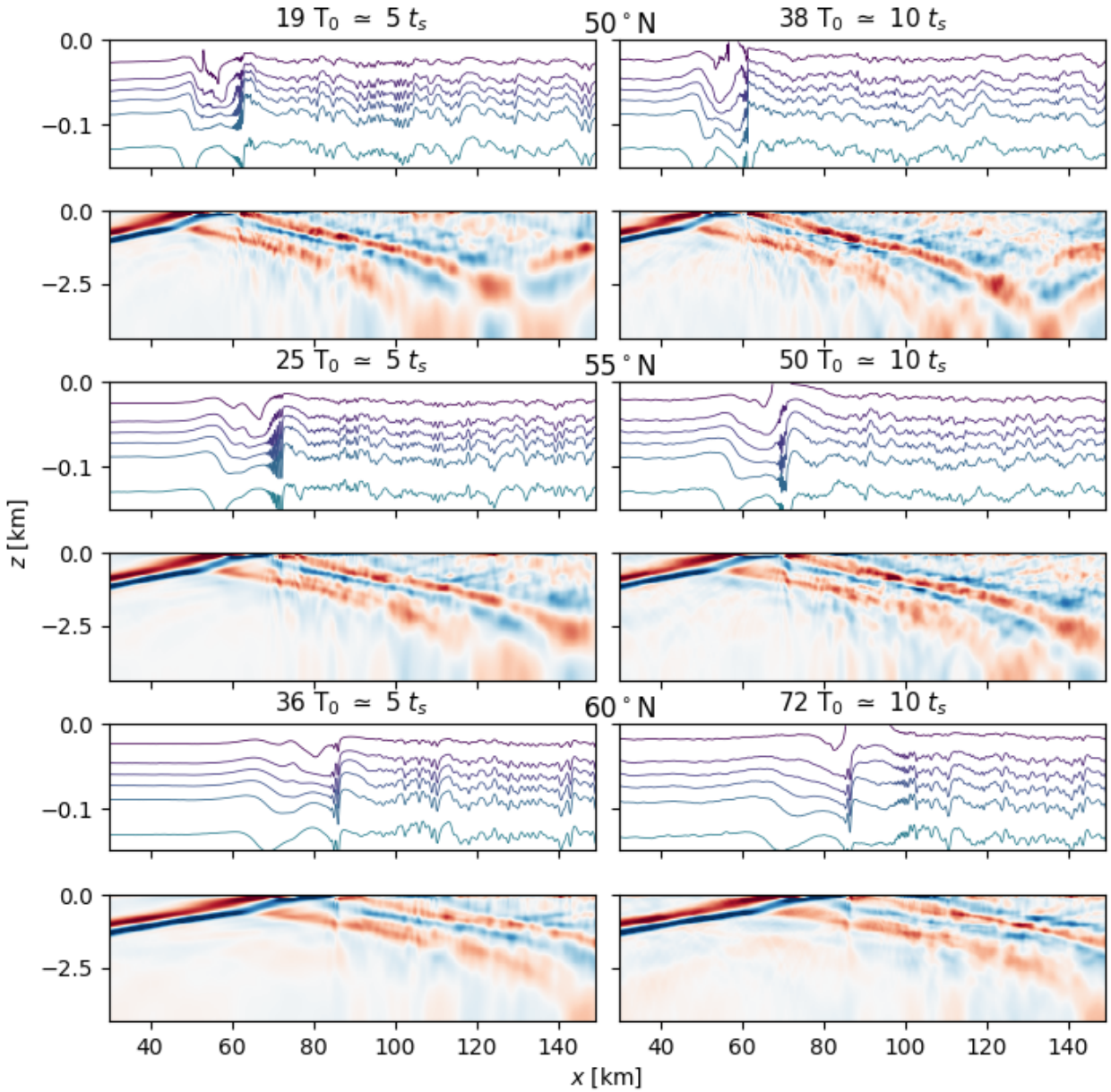

Figure 3.4: Same as Figure 3.3 except data is for latitudes 50°N (top two rows), 55°N (middle two rows), and 60°N (bottom two rows).

Looking at displacements of the pycnocline gives a clearer view of the effect of TRI on the generation of interfacial waves. In Figure 3.5 the pycnocline displacements for six different latitudes are plotted as functions of horizontal distance and time. The time periods shown are from $3t_s$ to $3t_s$+25 T_0 (rounded down to the nearest integer multiple of T_0) to facilitate comparison. The green boxes enclose two different time intervals, R_1 and R_2 (Table 3.1). In the first time period, R_1, large displacements are caused by the ITB impinging on the pycnocline from below, and isopycnal disturbances propagate horizontally to the right for all latitudes. In the second time period, however, pycnocline displacements are noticeably smaller in amplitude for latitudes 15-35°N, especially for 25°N and 29°N. For 45°N and 55°N, the propagation of interfacial waves appears stationary within the time period shown. This supports our hypothesis that TRI at latitudes around the CL and equatorward can disrupt the generation of interfacial waves, possibly because the beam has become defocused and already has lost much of its energy before it passes through the pycnocline.

The propagation of the isopycnal displacements is better seen in Figure 3.6. The propagation of isopycnal disturbances appear as diagonal lines, the slopes of which are the inverse phase speed of the interfacial waves. Displacements associated with the ITB impinging on the pycnocline from below are parallel to the blue dashed lines, radiating from the impact location every T_0, and displacements associated with higher frequency interfacial waves are parallel to the red dashed lines (similar to Figure 4 from GS10). We see again that at 45°N the simulation is quite stationary, and the situation during R_1 is similar to that of R_2. There are large isopycnal displacements where the beam impacts the pycnocline, occurring every wave period. Interfacial waves associated with the initial pycnocline displacement propagate to the right at a higher frequency. Interfacial wave trains (e.g., red lines) are separated by about 25 km, and have higher frequencies than the larger displacements from the ITB impact on the pycnocline (e.g., blue lines). The phase speed for the higher-frequency waves is nearly identical for the different latitudes because the influence of the Coriolis frequency on the propagation of these waves is felt less than for the lower-frequency waves. At 29°N there are strong displacements and propagating interfacial waves during R_1, but only very small propagating displacements at the forcing frequency during R_2, and no propagating interfacial waves. At 15°N

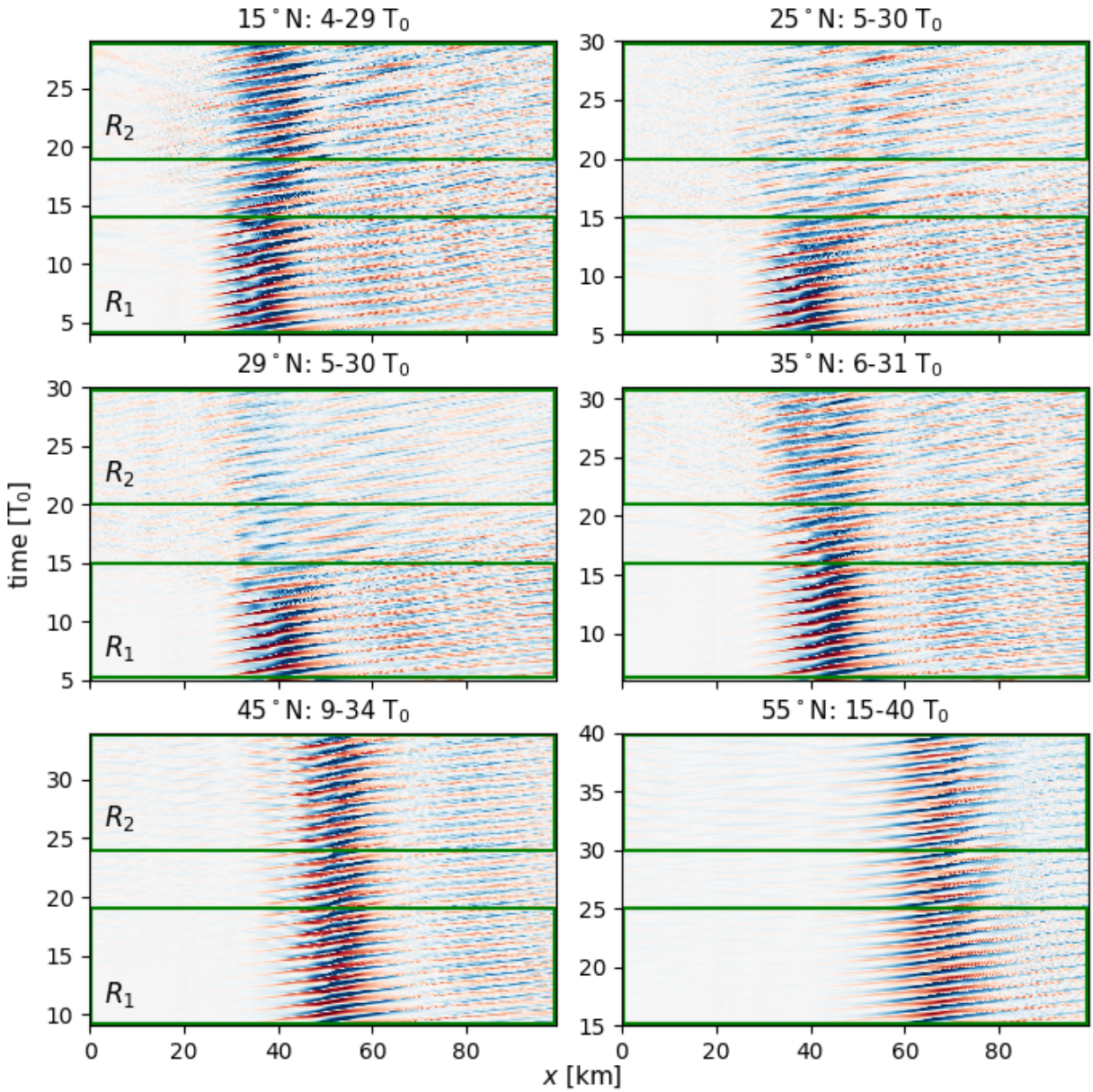

Figure 3.5: Displacement of the pycnocline for six different latitudes. The color scale ranges from -20 m to 20 m (blue is negative, red is positive). Note that the time axis for the different latitudes do not all start at the same value (with respect to T_0) but they all span a duration of 25 T_0. Time ranges from $3t_s$ to $3t_s + 25\,T_0$. The green boxes each span a duration of 10 T_0 (R_1 and R_2), and are separated by 5 T_0 (see Table 3.1 for details about t_s, R_1 and R_2).

the amplitude of the interfacial waves is diminished during R_2 but still present. Consistent with Figure 3.4, interfacial waves have larger amplitudes at 50 and 55°N when compared to 45°N, and the amplitudes are smaller during R_2 than R_1 (Figure 3.7). At 60°N the simulation appears stationary after 27 T_0. Disturbance to the pycnocline due to the initial impact of the ITB does not appear at 60°N in Figure 3.7 due to its small amplitude, but there are still clear indications of higher-frequency interfacial waves (Figure 3.4).

3.3.2 Frequency spectra

We examine the distribution of wave energy in frequency space by calculating power spectral densities of u-velocities in the pycnocline (Figures 3.8 and 3.9 show latitudes 5-29°N and 35-60°N, respectively). We find that M_2 energy in the pycnocline usually appears near the surface reflection and extends more than 50 km to the right. In many cases (e.g., 29°N, 50°N, 55°N), energy at M_2 and subharmonic frequencies extend to the left of the surface reflection as well. The persistence of energy in the pycnocline at different frequencies can be described as "ducting", or partial trapping, of ITB energy (Mathur & Peacock, 2009). Energy can stay in the pycnocline for a distance of more than 100 km. During R_1, wave energy is transferred to higher harmonics, up to $10\,\omega_0$, for all latitudes considered (0-60°N). For certain latitudes, both equatorward and poleward of the CL (e.g., 15°N, 25°N, 50°N), there is already transfer of energy to sub-M_2, or subharmonic, frequencies during R_1. For all latitudes, energy at subharmonic frequencies is higher during R_2 when compared to R_1, and exists over a wider horizontal extent. The appearance of energy at subharmonic latitudes is accompanied by a decrease in energy at higher harmonics for latitudes 25-35°N. For most latitudes, subharmonic energy is strongest at the Coriolis frequency f (green dashed lines). There is also energy at the frequency $\omega = \omega_0$-f, even when it is outside the internal wave band for latitudes poleward of the critical latitude.

To further examine the spatial extent of subharmonic energy we look at the PSD of u-velocity for the whole water column at only two frequencies, the forcing frequency ω_0 and the subharmonic

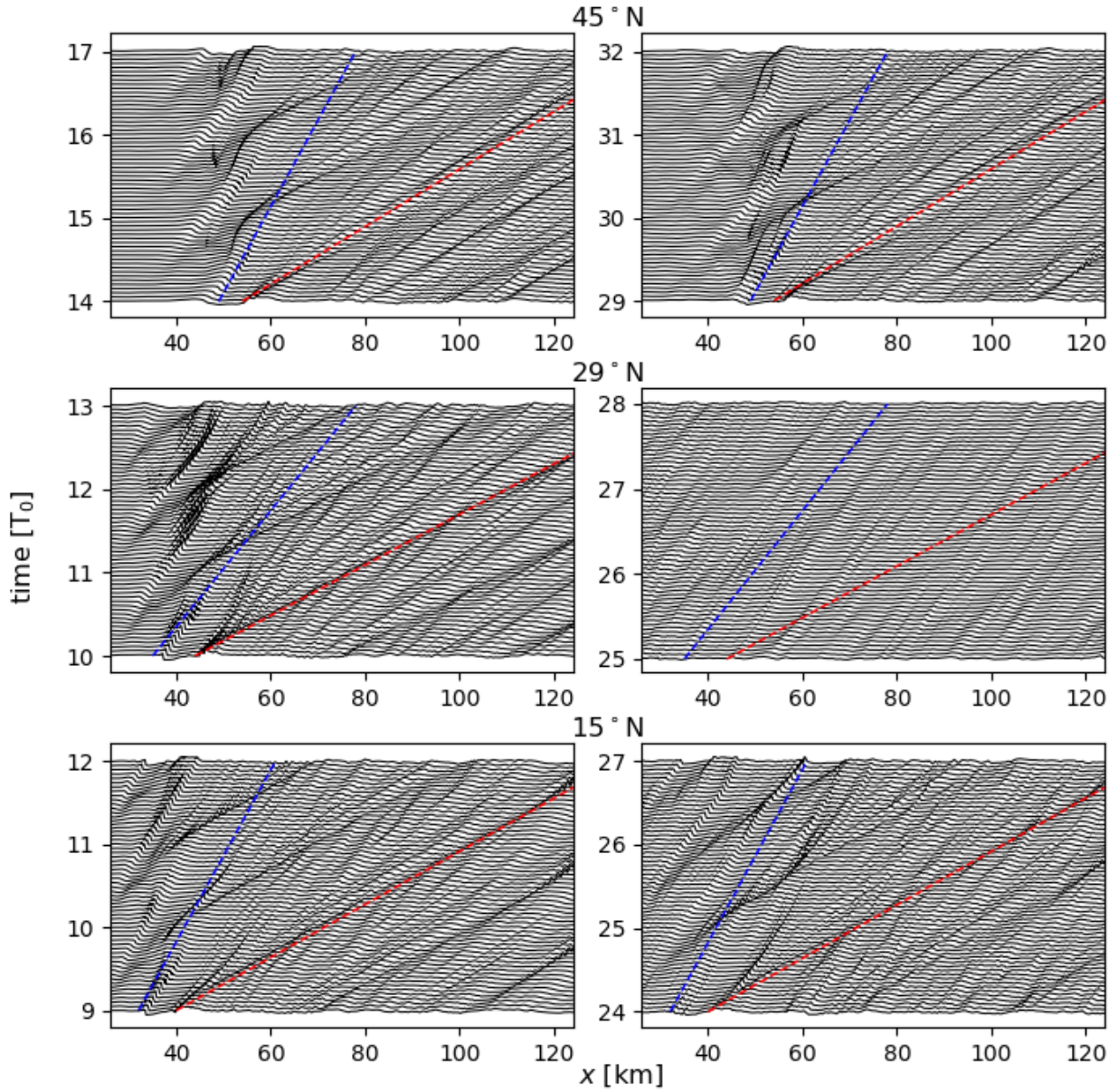

Figure 3.6: Isopycnals at the pycnocline are plotted as a function of distance and time for 3 different latitudes. Left panels show the first 3 wave periods of R_1, and right panels show the first 3 wave periods of R_2. The blue and red lines trace example waves associated with the ITB impinging on the pycnocline from below and with higher-frequency interfacial waves, respectively.

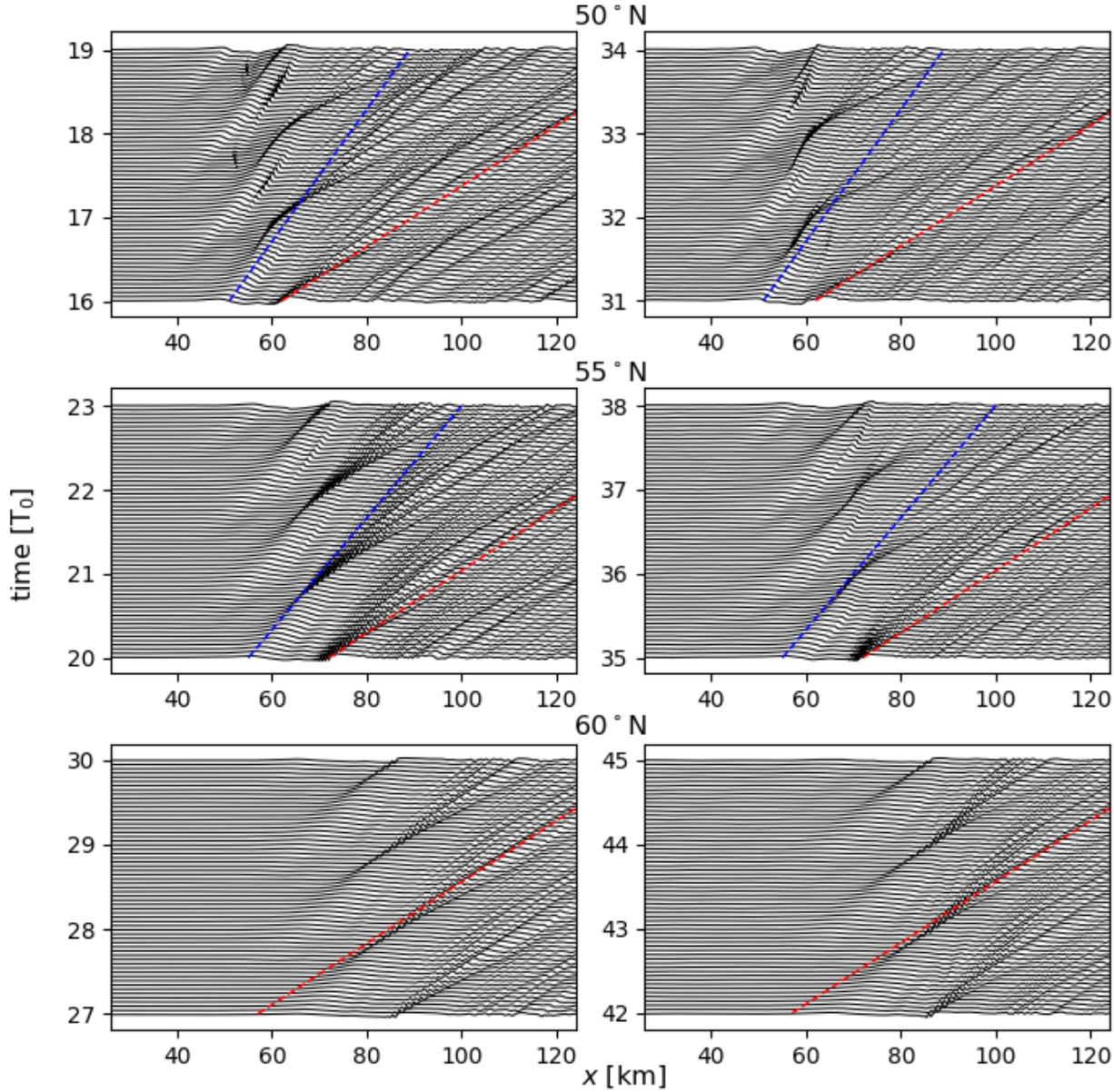

Figure 3.7: Same as Figure 3.6 except data is for latitudes 50°N, 55°N, and 60°N. There are no lines for the interfacial waves at 60°N because they are not identifiable in this plot.

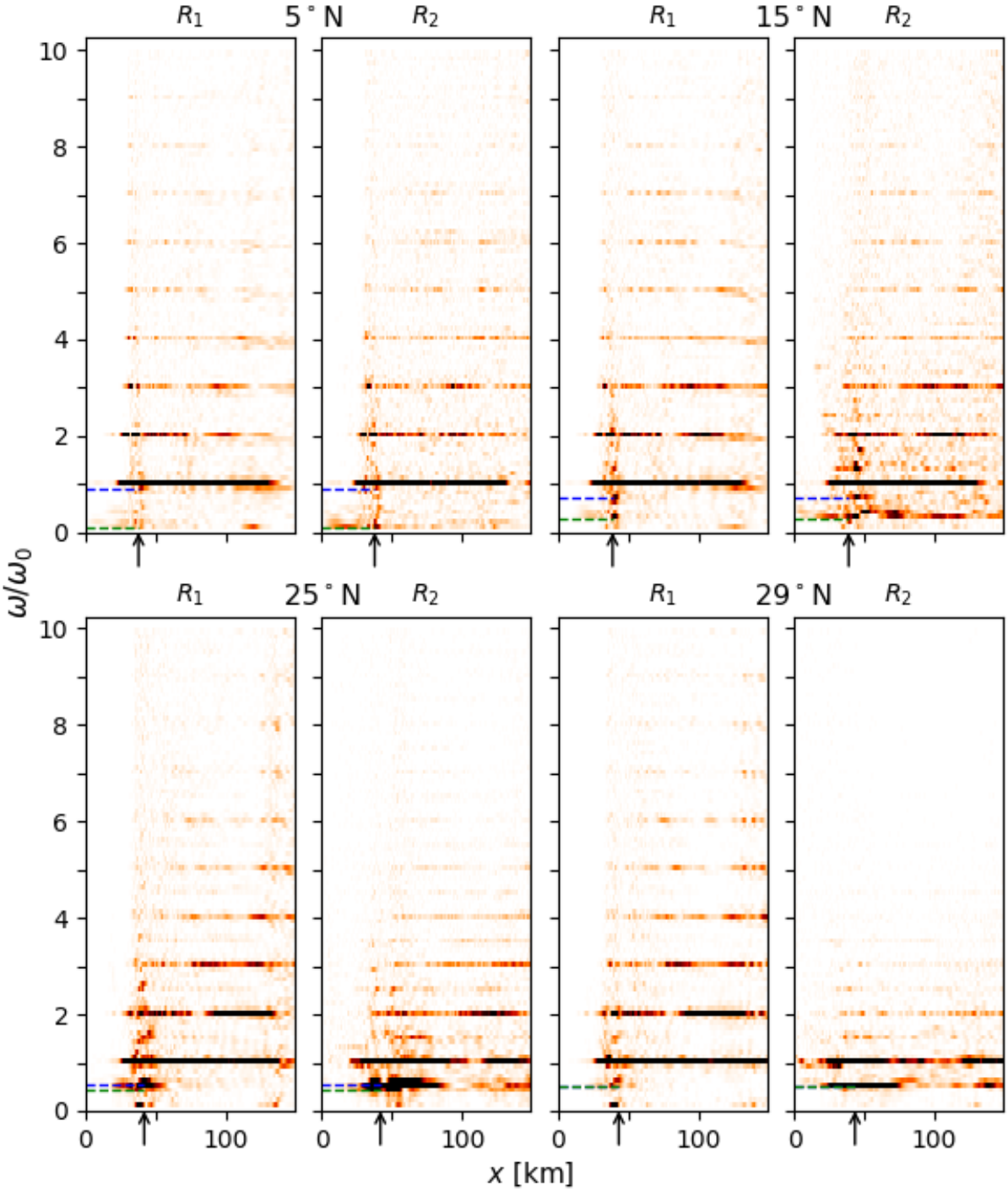

Figure 3.8: The PSD of u-velocity (averaged from 46-70 m depth) for 4 different latitudes (5-29°N) are shown for time periods R_1 and R_2. The color scale is the same for all plots, and the frequencies range from 0 to 10 ω_0. The small vertical arrows indicate the x-locations of the ITB surface reflection. Horizontal green dashed lines indicate the Coriolis frequency $\omega = f$, and the blue lines indicate $\omega = \omega_0$-f.

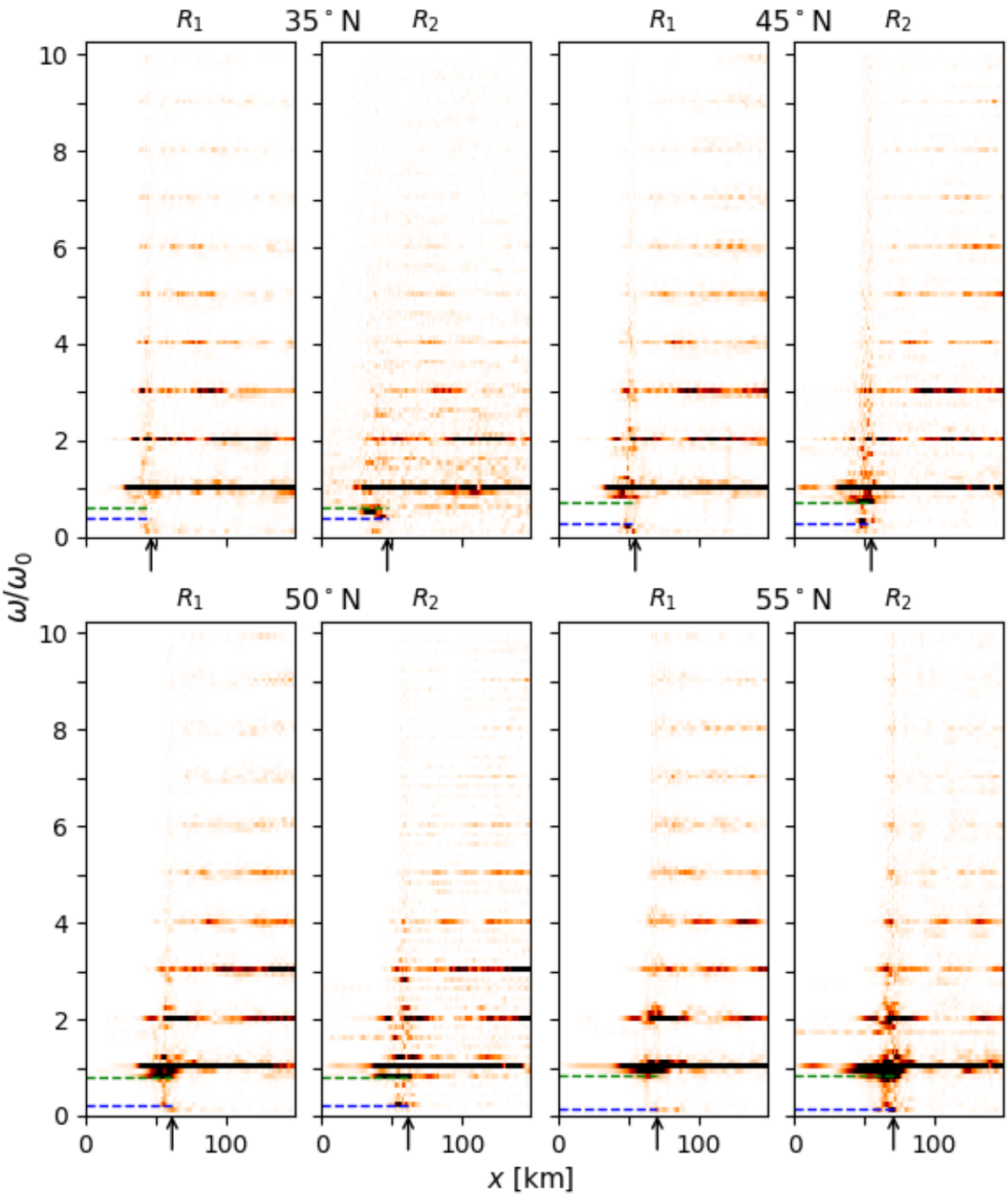

Figure 3.9: Same as Figure 3.8 except data is for latitudes 35-55°N.

frequency $\frac{1}{2}\omega_0$ (Figure 3.10). At both 25°N and 29°N there is subharmonic energy during R_1 but it is only a fraction of the energy at M_2. During R_2 the subharmonic energy becomes stronger than the energy remaining at M_2 and spreads over a wider area. The M_2 beam is noticeably weakened as it propagates upward and not much energy makes it up to the surface. It is worth noting that even during R_1 the M_2 beam appears weakened after surface reflection, presumably due to loss of energy to other frequencies, the generation of interfacial waves, and scattering in the pycnocline. As seen in Figures 3.8 and 3.9, subharmonic energy is often strongest at the local Coriolis frequency, though not always. For example, at 25°N f is 0.44 ω_0 while PSD is strongest at 0.5 ω_0 (Figure 3.11c; label will be added). And at 35°N, f and ω_0-f are 0.59 ω_0 and 0.41 ω_0, respectively, while PSD is again strongest at 0.5 ω_0. Although PSD is strongest at 0.5 ω_0 for 35°N, Figure 3.11 shows that it is only strong in a small area, and elevated PSD actually covers a larger extent at 0.6 ω_0 and 0.4 ω_0.

3.3.3 Wave number spectra

Triadic resonant interactions, such as PSI, transfer energy to secondary waves of smaller vertical scale and of subharmonic frequencies that add up to the forcing frequency. In the previous section we saw that there are transfers of energy from an M_2 internal tide beam to subharmonic waves with frequencies f and ω_0-f. Looking at the wavenumber spectra (Figure 3.12) of u-velocity of the beam prior to surface reflection (from 20-25 km), we see that the beam becomes dominated by small vertical scale motions. There is a spread of energy to larger wavenumbers for latitudes equatorward of 35°N. At 45°N the simulation appears stationary, as we have seen before. Black arrows point to the vertical wavenumber of the forcing beam, and energy is focused around this value early in the simulations, as expected.

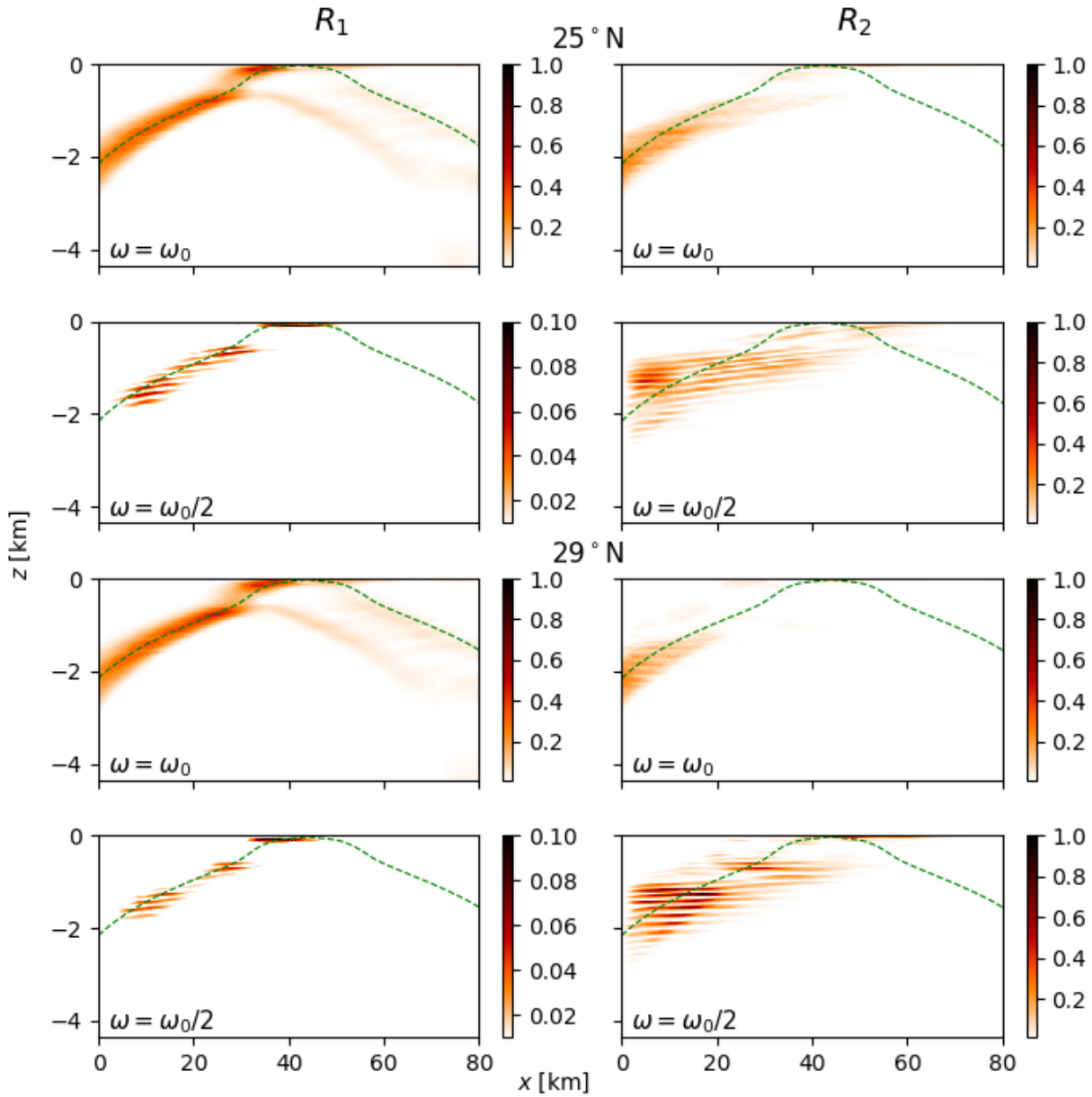

Figure 3.10: The PSD of u-velocities for the time periods R_1 (left panels) and R_2 (right panels). At each latitude the PSDs are normalized by the maximum PSD at ω_0 for R_1. The frequencies are noted in the lower left corner. Note that the color scale is not the same for all plots. Internal wave characteristics are plotted in green.

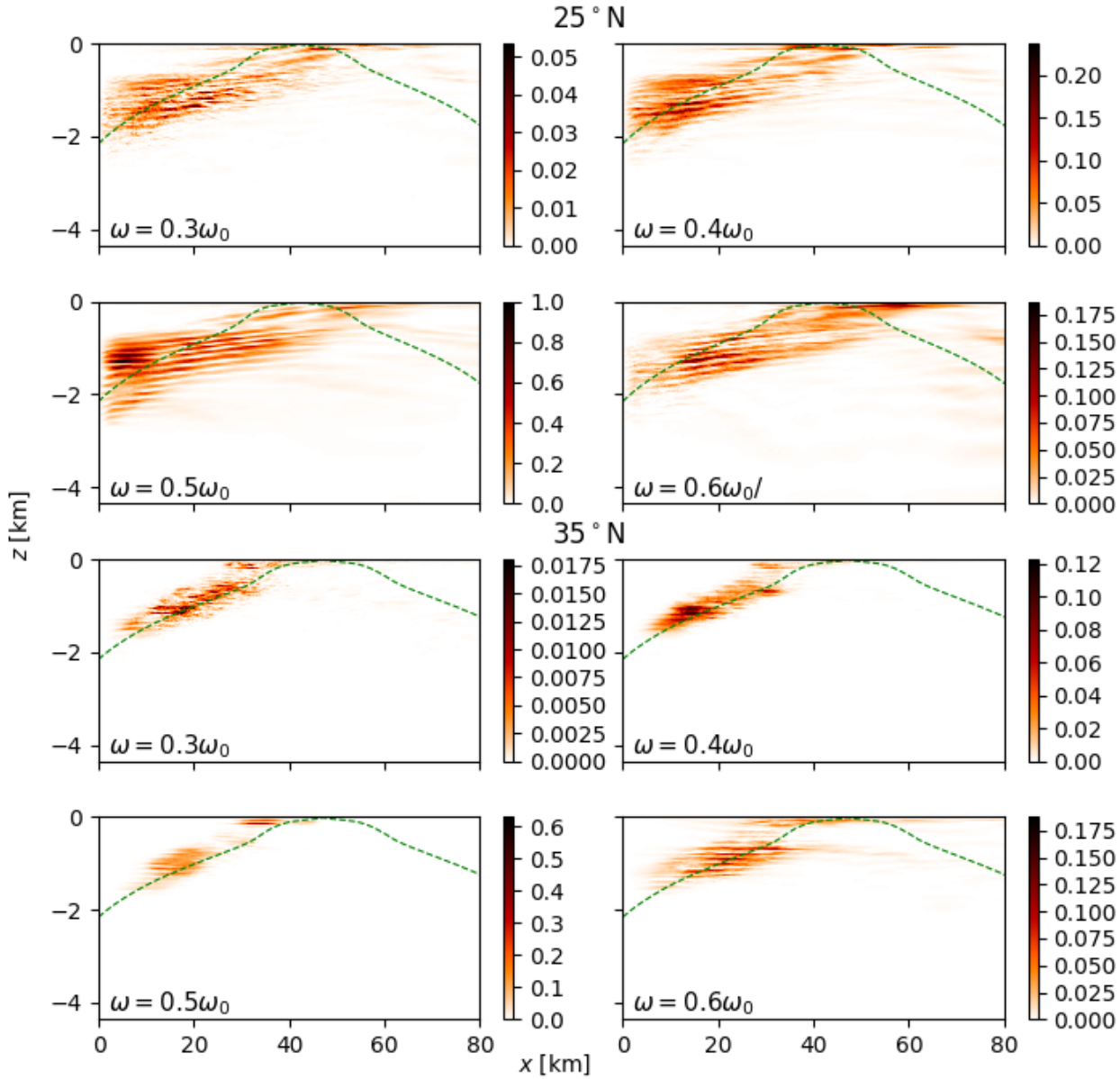

Figure 3.11: The PSD of u-velocity for R_2 at four discrete frequencies. At each latitude the PSD is normalized by the maximum PSD (of any frequency) for R_2 (the maximum for 35°N occurs for ω_0, not shown). The frequencies are noted in the lower left corner. Note that the color scale is not the same for all plots. Internal wave characteristics are plotted in green.

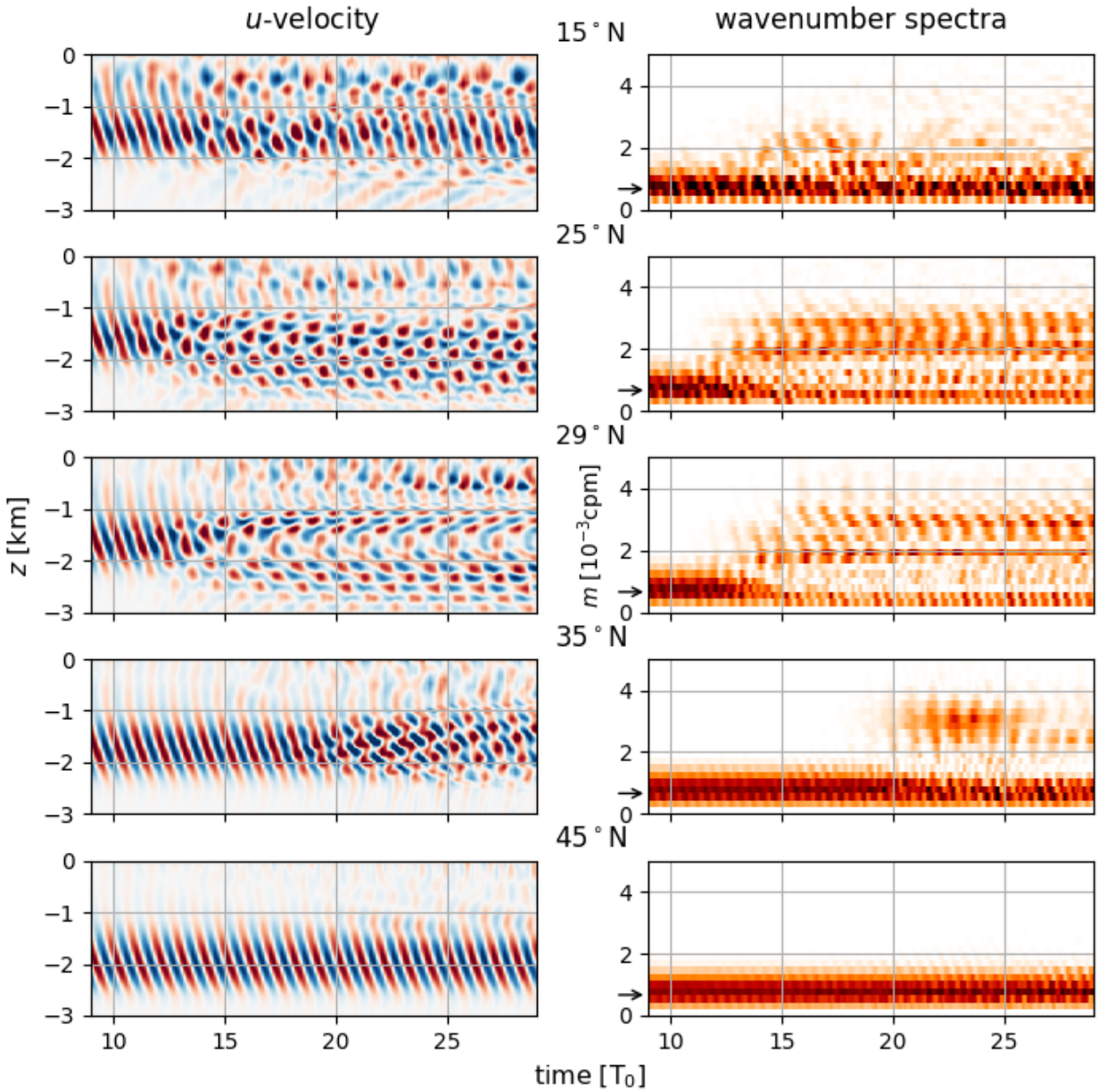

Figure 3.12: Left column: u-velocity (WKB stretched) averaged from 20-25 km in the x direction as a function of time. Right column: associated vertical wavenumber spectra as a function of time. The small black arrows point to the wavenumber of the forcing beam.

3.4 Hawaii stratification (HOT) experiments

For further comparison with GS10 E2, we look at what happens when we change the stratification from one that is representative of a mid-latitude environment (BB) to one from tropical latitudes (HOT). As before with the BB profile, we see that the simulation appears stationary at 45°N, with the ITB causing a displacement in isopycnals when it impacts the pycnocline from below (Figure 3.13). However, there does not appear to be any propagation of interfacial waves at any of the latitudes. At 29°N there is a large impact on the pycnocline due to the upward propagating beam at $5t_s$, but not at $10t_s$, where lower frequency waves have extracted a large amount of energy out of the ITB and there is only a faint reflected downward propagating beam. The situation is similar at 15°N, but the beam degradation is not as severe. Looking at pycnocline displacements as we did before, we find again that the amplitudes of the displacements are reduced for latitudes 35°N and equatorward during R_2, while the simulations at 45°N and poleward appear stationary (Figure 3.14). Examining isopycnals around the pycnocline as a function of time confirms that there is impact from the ITB on the pycnocline at all latitudes during R_1, but there is no propagation of higher frequency interfacial waves (Figure 3.15), as there were for BB experiments. For 29°N there is impact from the ITB during R_1 but it is very weak during R_2. Again the situation is similar at 15°N, where there is weaker disturbance to the pycnocline from the impinging ITB during R_2, and there is a faint propagation of interfacial waves at the M_2 frequency only.

PSD of u-velocity around the pycnocline shows that there is transfer of energy to subharmonic waves at the local Coriolis frequency and at $\omega = \omega_0 - f$ during R_2 (Figures 3.16 and 3.17). Compared to the simulations with the BB stratification, there is much less transfer of energy to higher harmonics, and the M_2 energy in the pycnocline is much more limited in horizontal extent. Similar to the BB experiments there is still some transfer of energy to sub-M_2 frequencies for latitudes poleward of the CL (e.g., 40°N and 45°N). Focusing on only two latitudes, 25°N and 29°N, we see again that substantial energy is transferred to subharmonic frequencies and results in the weakening of the M_2 ITB during R_2 (Figure 3.18). Although f at 25°N and 35°N is $0.44\,\omega_0$ and $0.59\,\omega_0$, respectively, PSD

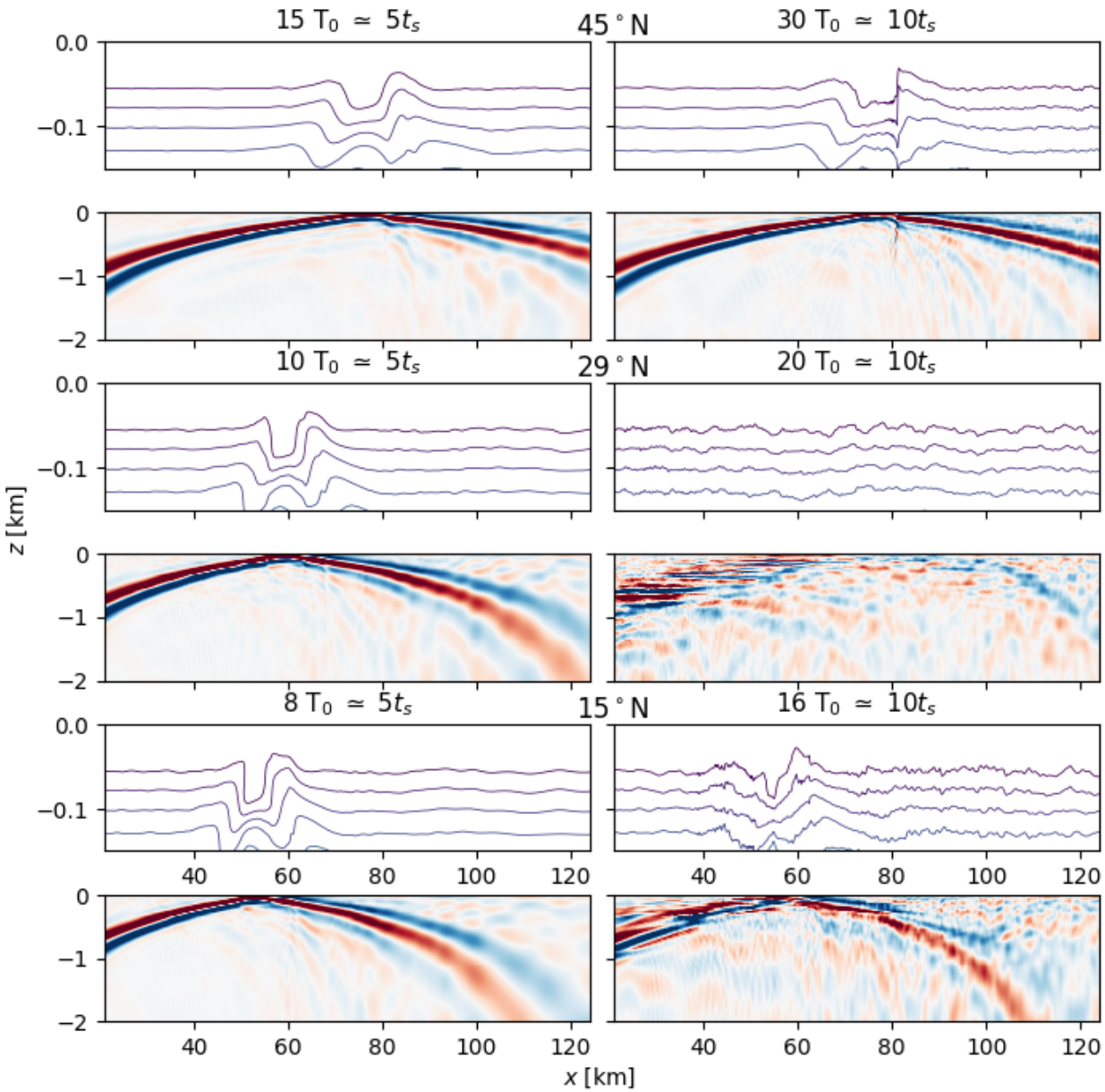

Figure 3.13: Same as Figure 3.3 except the stratification is from HOT (pycnocline is at 72 m depth).

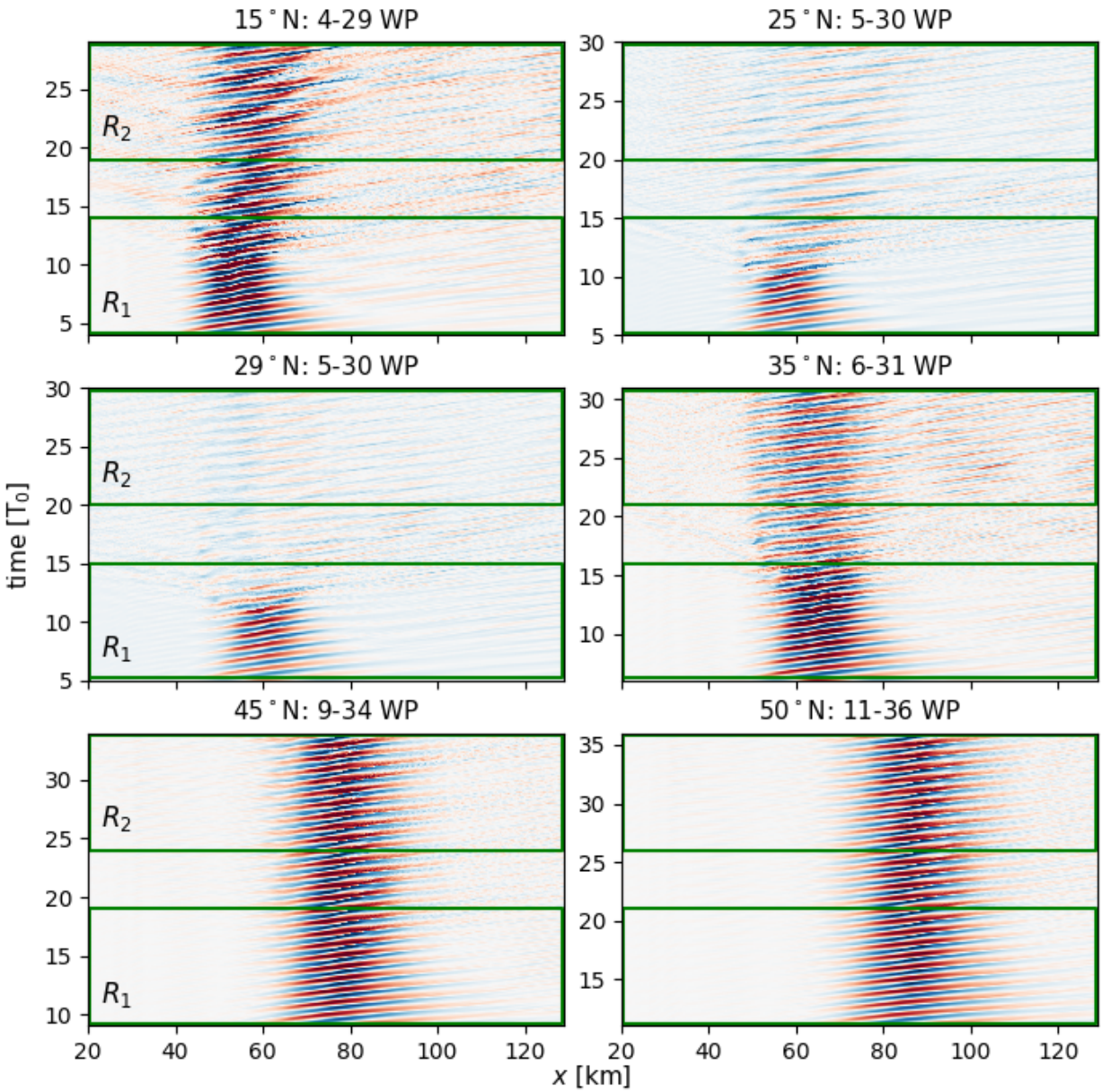

Figure 3.14: Same as Figure 3.5 except the stratification is from HOT, and 55°N is replaced by 50°N.

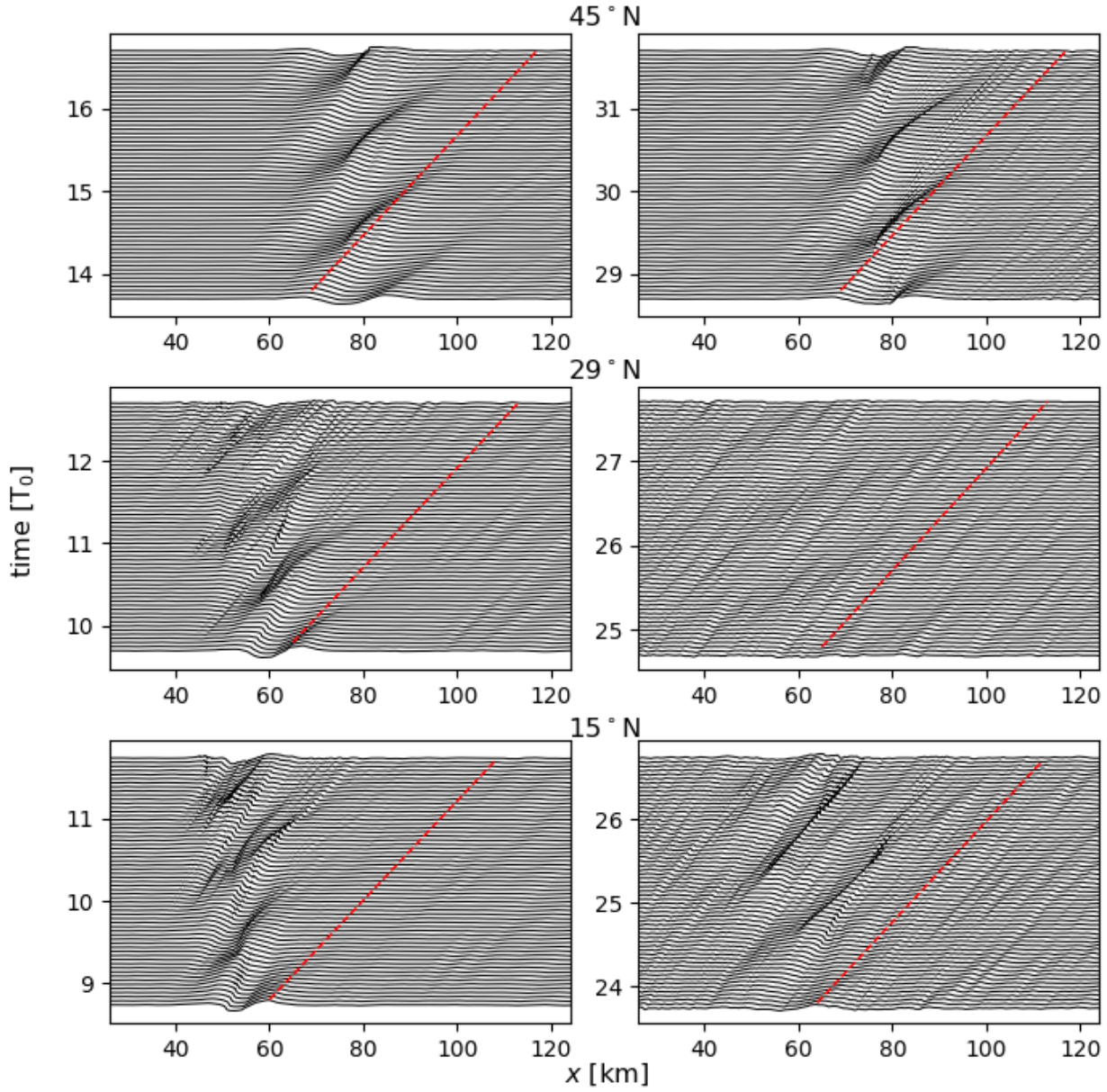

Figure 3.15: Same as Figure 3.6 except the stratification is from HOT and the density is for 74 m depth. Here the red lines trace example waves associated with the ITB impinging on the pycnocline from below. There are no indications of propagating interfacial waves.

is strongest at $0.5\,\omega_0$ for both latitudes (Figure 3.19). Examining wavenumber spectra shows, as for BB experiments, that the transfer of energy to subharmonic waves is correlated with the transfer of energy to smaller vertical scale motions for latitudes 35°N and equatorward (Figure 3.20). Note that velocities and PSDs increasingly weaken after $15\,T_0$ for 25°N and 29°N because the ITB near the pycnocline has lost much of its energy by $15\,T_0$, as we can see from Figure 3.14.

3.5 Quantifying nonlinear energy transfers

As a way to quantify the energy at different frequencies during $\boldsymbol{R}_1$ and $\boldsymbol{R}_2$ for different latitudes, we introduce three indices: the M_2 index, the sup-M_2 index, and the sub-M_2 index. Each index is calculated from the PSD of u-velocity averaged over a depth interval centered on the pycnocline (20 m for BB, 24 m for HOT). The PSD is then integrated horizontally over 50 km, starting from the surface reflection. The M_2 index (top row of Figure 3.21) is the M_2 energy in this integrated PSD, normalized by the total contributed by all frequencies. Similarly, the sup-M_2 and sub-M_2 indices are the fractions contributed by superharmonic and subharmonic frequencies, respectively.

For both sets of experiments the M_2 index is dependent on latitude and on how long the simulations have been run. M_2 energy reaches a minimum during $\boldsymbol{R}_2$ at 29°N and increases away from the CL, with higher levels poleward of the CL than equatorward. The sup-M_2 index is low around 29°N for the BB experiments during $\boldsymbol{R}_2$, presumably because the internal tide beam itself is already weakened before reaching the pycnocline. For the HOT experiments, sup-M_2 is in general higher during $\boldsymbol{R}_2$ than $\boldsymbol{R}_1$ and is very low at latitudes 40-50°N, in contrast to BB experiments. For the BB experiments, sub-M_2 is highest at 29°N and drops off gradually equatorward of the CL and sharply poleward of the CL. For HOT experiments sub-M_2 actually reaches its peak at 20°N. This could be because at latitudes closer to the CL, the beam has already lost much of its energy due to TRI before reaching the pycnocline, and does not have as much energy to transfer to subharmonic motions in the pycnocline.

Examining the pycnocline u-velocity might not fully capture the subharmonic energy, as often the

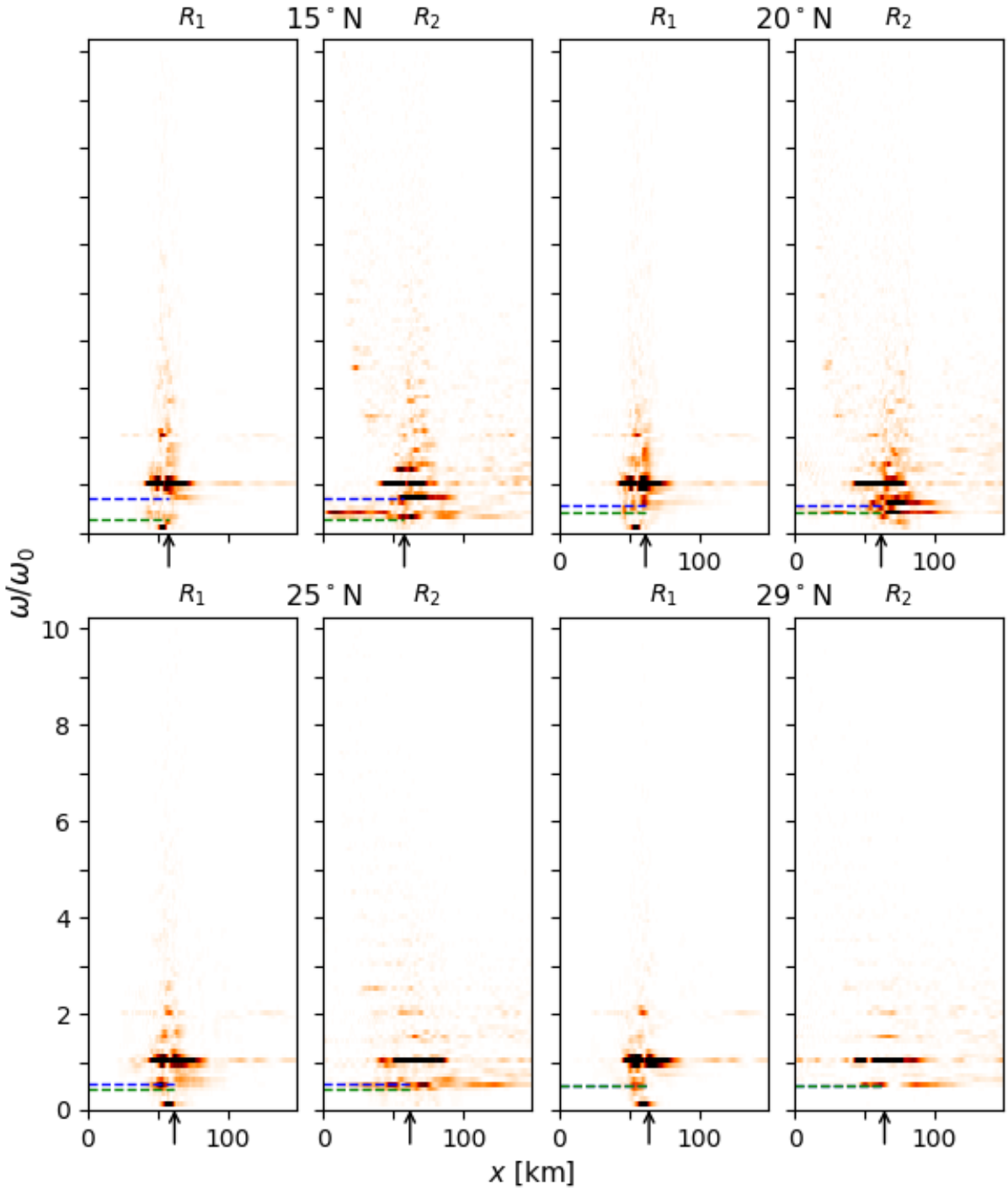

Figure 3.16: Same as Figure 3.8 except here the stratification is from HOT, and 5°N is replaced by 20°N. Velocity is averaged from 62-82 m depth.

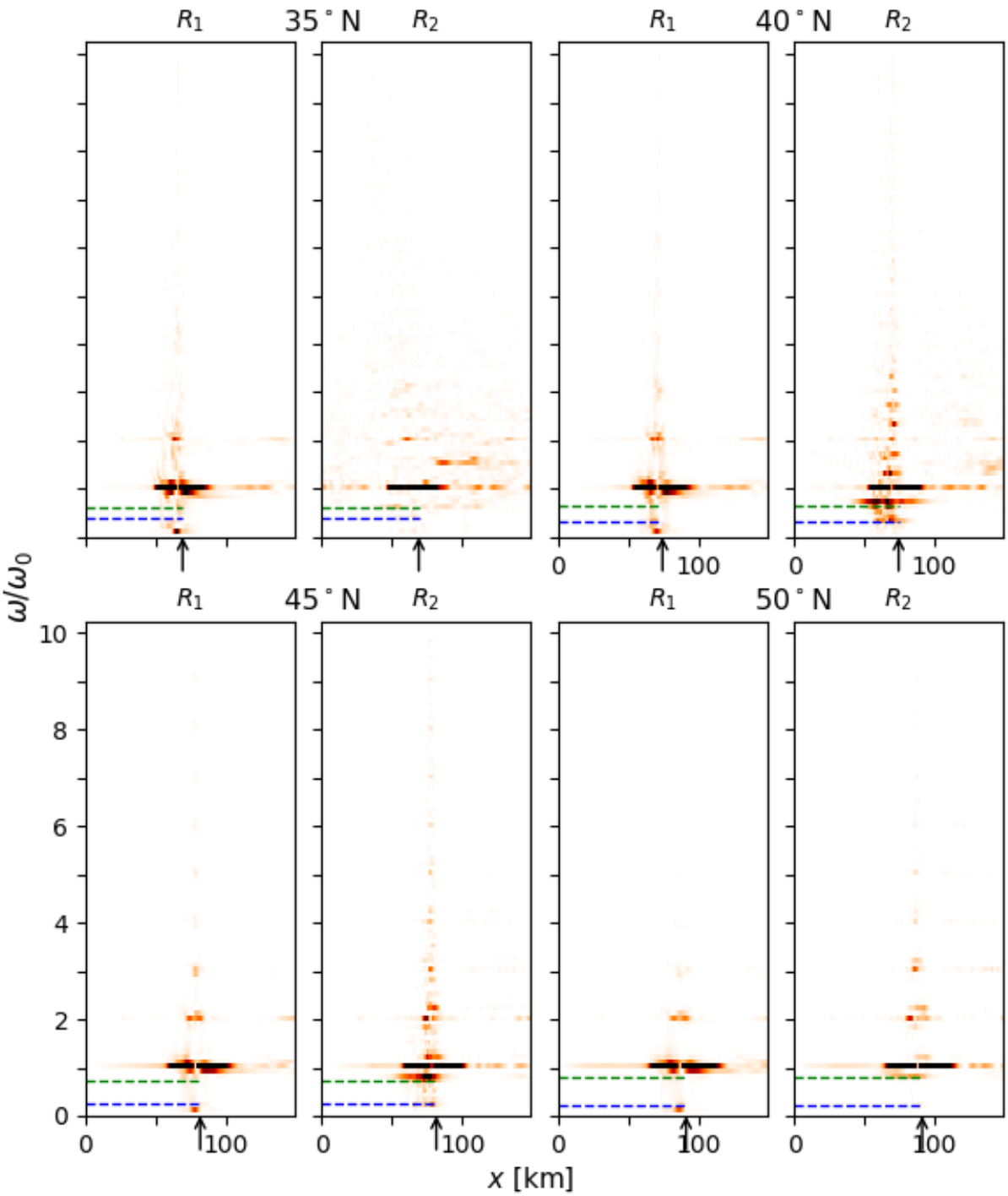

Figure 3.17: Same as Figure 3.9 except here the stratification is from HOT, and 55°N is replaced by 40°N.

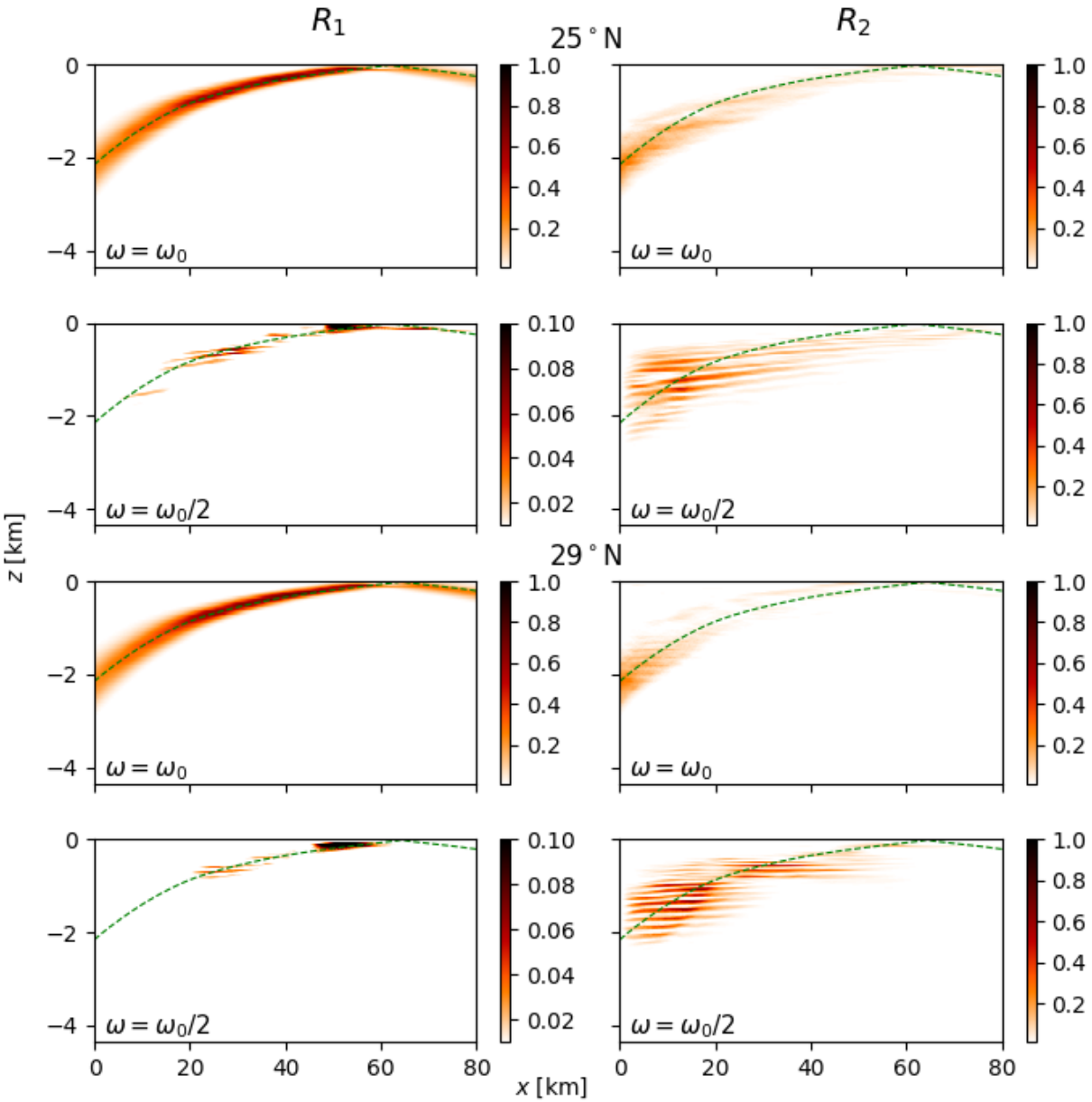

Figure 3.18: Same as Figure 3.10 except here the stratification is from HOT.

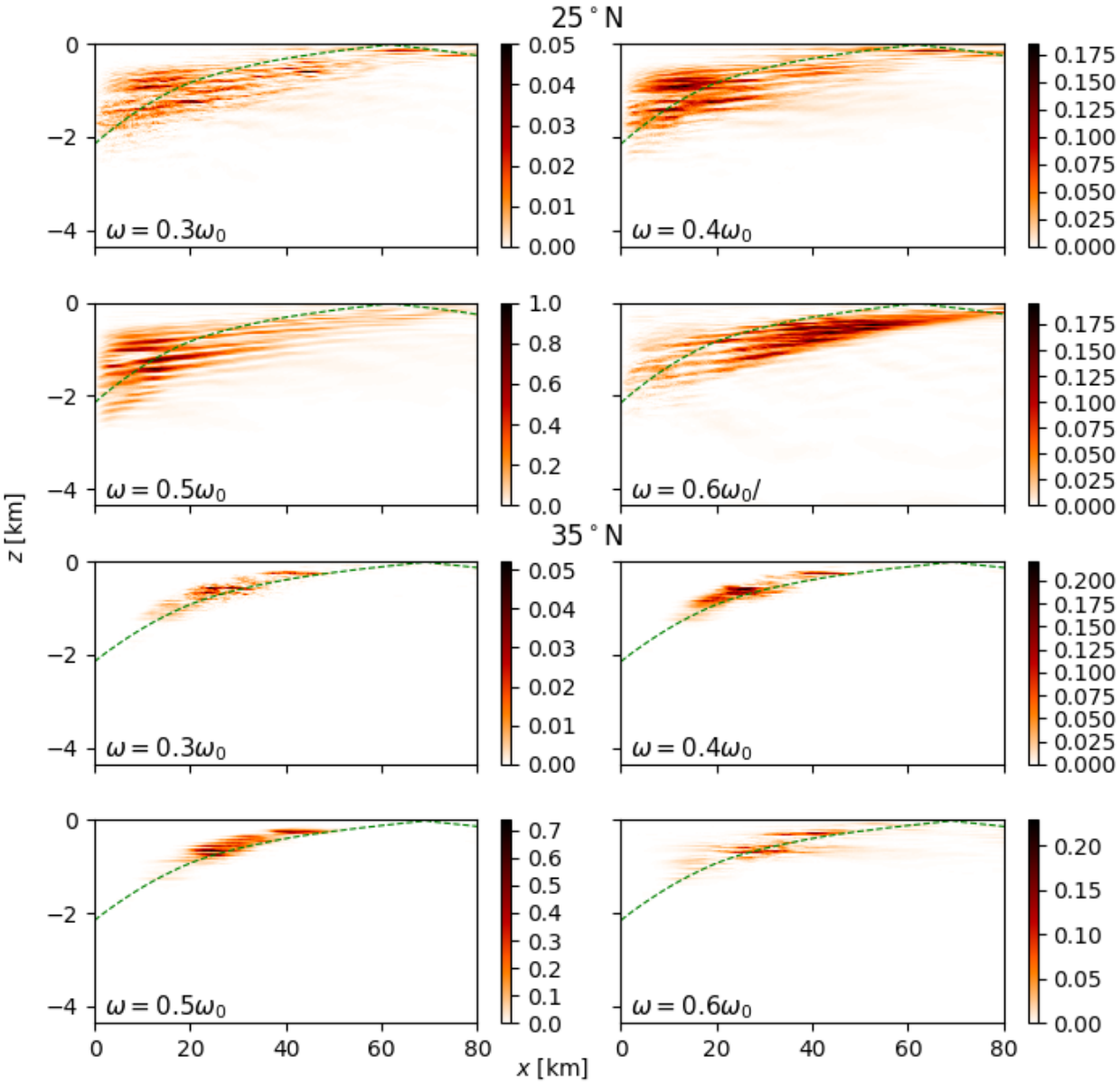

Figure 3.19: Same as Figure 3.11 except here the stratification is from HOT.

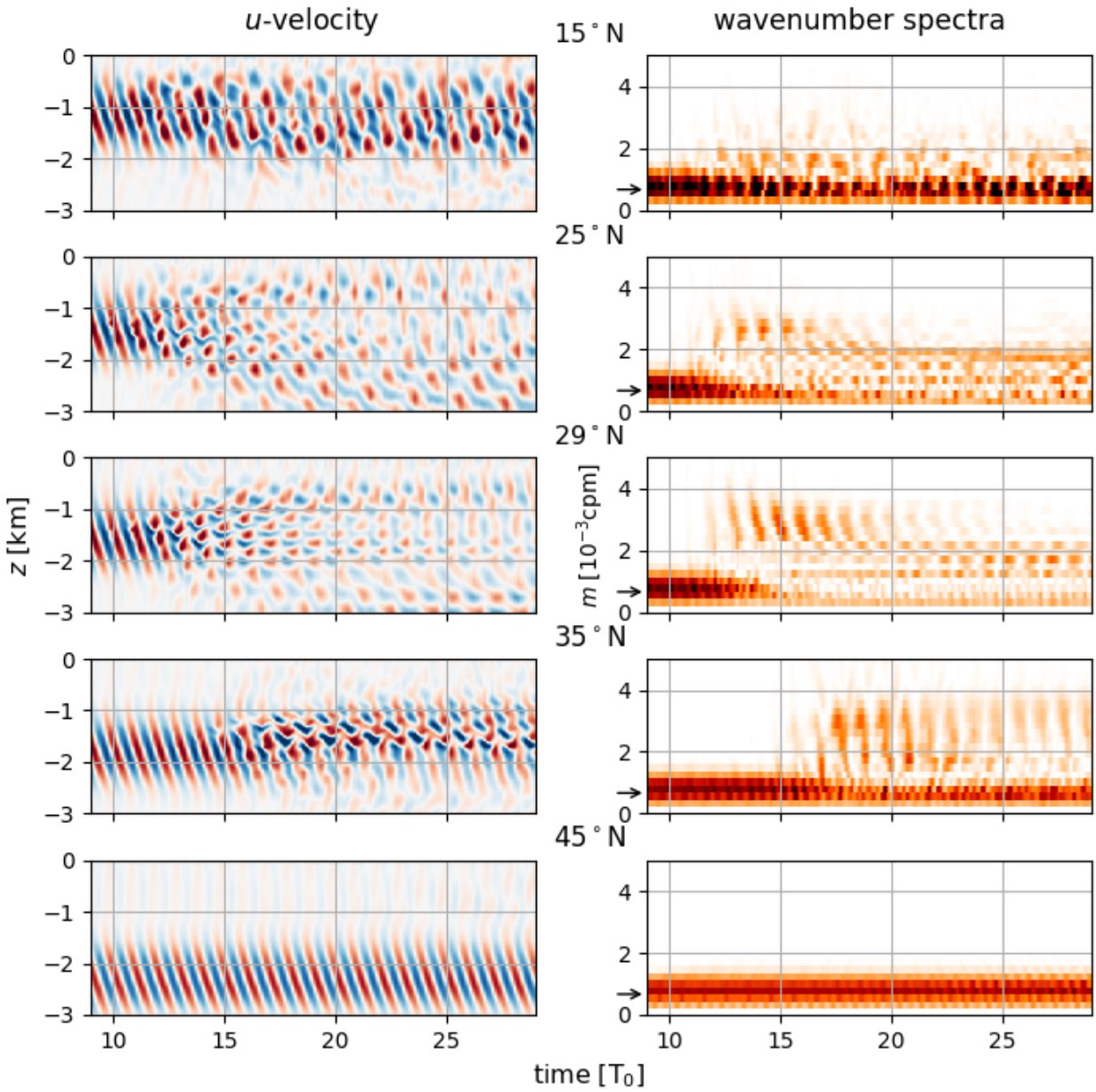

Figure 3.20: Same as Figure 3.12 except here the stratification is from HOT and the u-velocity is averaged from 40–45 km.

subharmonic waves appear near the left boundary and diminish as the beam propagates upwards, before reaching the pycnocline (see Figure 3.10). Another way to quantify the transfer of energy to subharmonic frequencies is to calculate the Subharmonic Energy Ratio SER (Chou, 2013, Ansong et al., 2018) by taking the ratio of the maximum PSD at a subharmonic frequency, not necessarily at half M_2, to the maximum PSD at M_2 (Table 3.2). The spatial domain considered is from $x = 0\text{-}80$ km and spans the full water column (the domain shown in Figure 3.10). For 25°N and 29°N, maximum SER occurs near the surface above the pycnocline for $\boldsymbol{R}_1$, and near the left boundary where the beam originates for $\boldsymbol{R}_2$ (Figure 3.10). Although there is non-negligible energy at subharmonic frequencies even up to 60°N, the spatial extent of this energy is very limited at latitudes poleward of 35°N. It is worth noting that some SER values might be reduced because the frequency of maximum PSD does not fall on an integer multiple of $\frac{1}{10}\boldsymbol{\omega}_0$, the frequency grid spacing for our analysis. Overall, SER values (bottom row of Figure 3.21) are as we expect based on previous analysis using the M_2, sup-M_2, and sub-M_2 indices. SER values are much higher during $\boldsymbol{R}_2$ than $\boldsymbol{R}_1$, suggesting that it takes substantial time for subharmonic waves to grow. They are highest at 29°N, reaching almost 4 for BB experiments, and dropping off gradually equatorward of the CL. SER appears to be a better indication of TRI than the sub-M_2 index because it accounts for energy throughout the domain and not only in the pycnocline.

3.6 Summary and Discussion

This study examines two sets of experiments, one using a stratification profile representative of the Bay of Biscay at mid-latitudes, and another one using a profile representative of tropical latitudes from HOT. Different values of the Coriolis frequency were tested in each set of experiments to investigate the latitude dependence of what happens to ITBs as they propagate up toward the surface and transits through the pycnocline. Both sets of experiments show transfers of energy from the M_2 tide to subharmonic frequencies, accompanied by the appearance of energy at small vertical scales, suggesting the presence of triadic resonant instability. Many studies of TRI focused on PSI, a special

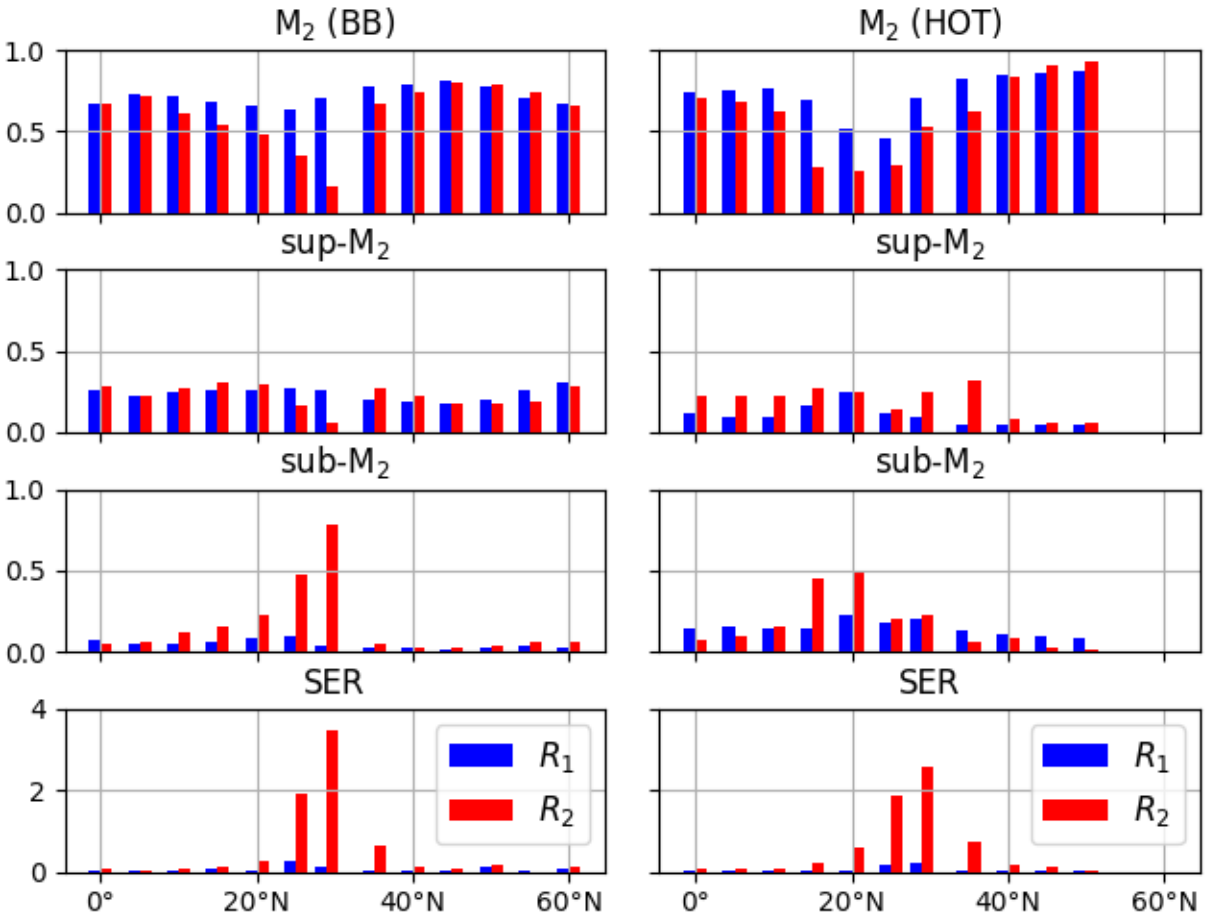

Figure 3.21: Indices representing energy in different frequency bands, for R_1 and R_2 and different latitudes (top three rows). Details about these indices are given in the text. The fourth row shows the Subharmonic Energy Ratio (SER). Note that there are no data at 55°N and 60°N for HOT experiments.

Table 3.2: The ratio of M_2 subharmonic energy to M_2 energy (SER) during $\boldsymbol{R_1}$ and $\boldsymbol{R_2}$ (two rightmost columns). The first column lists the approximate latitude of the experiment, the second lists the local inertial frequency f normalized by $\boldsymbol{\omega_0}$, the third lists the frequency that has the highest PSD during $\boldsymbol{R_2}$ (sometimes it is different during $\boldsymbol{R_1}$), and the fourth lists the stratification profile that is used.

latitude [°N]	f [ω_0]	ω_s	**stratification**	SER (R_1)	SER (R_2)
0	0	0.1	BB	1.71×10^{-2}	4.81×10^{-2}
		0.4	HOT	5.26×10^{-3}	7.82×10^{-2}
5	0.1	0.1	BB	9.05×10^{-3}	2.84×10^{-2}
		0.4	HOT	5.47×10^{-3}	8.39×10^{-2}
10	0.2	0.2	BB	5.89×10^{-3}	6.50×10^{-2}
		0.4	HOT	1.23×10^{-2}	7.78×10^{-2}
15	0.27	0.3	BB	4.77×10^{-2}	1.23×10^{-1}
		0.3	HOT	1.43×10^{-2}	2.03×10^{-1}
20	0.35	0.4	BB	4.35×10^{-2}	2.42×10^{-1}
		0.4	HOT	2.54×10^{-2}	6.04×10^{-1}
25	0.44	0.5	BB	2.41×10^{-1}	1.92
		0.5	HOT	1.52×10^{-1}	1.89
29	0.50	0.5	BB	1.33×10^{-1}	3.48
		0.5	HOT	2.33×10^{-1}	2.57
35	0.59	0.5	BB	8.79×10^{-3}	6.28×10^{-1}
		0.5	HOT	1.63×10^{-2}	7.37×10^{-1}
40	0.67	0.5	BB	8.51×10^{-3}	1.19×10^{-1}
		0.5	HOT	3.11×10^{-2}	1.43×10^{-1}
45	0.73	0.7	BB	1.14×10^{-2}	8.91×10^{-2}
		0.8	HOT	6.15×10^{-3}	1.01×10^{-1}
50	0.79	0.8	BB	1.06×10^{-1}	1.51×10^{-1}
		0.8	HOT	3.42×10^{-3}	3.43×10^{-2}
55	0.85	0.8	BB	1.66×10^{-2}	1.49×10^{-1}
60	0.90	0.9	BB	8.32×10^{-2}	1.29×10^{-1}

case where the frequencies of secondary waves are assumed to be nearly equal and approximately half the frequency of the primary wave (McComas & Bretherton, 1977, MacKinnon & Winters, 2005, Carter & Gregg, 2006, Alford et al., 2007, Sun & Pinkel, 2013, Chou et al., 2014). However, we find that for a range of latitudes, energy is transferred from M_2 to f and M_2-f, even when these frequencies are different from $\frac{1}{2}M_2$. This has important implications for evaluating the global importance of TRI as an energy transfer mechanism by determining the physical extent where TRI is possible, and for correct interpretation of observational data.

In the numerical experiments of this study, the PSD of u-velocity around the pycnocline clearly showed the appearance of motions at subharmonic frequencies during R_2 for latitudes 15-55°N. Subharmonic waves were present at latitudes equatorward as well as poleward of the CL. At 35°N, poleward of the CL, energy in subharmonic waves can have more than 0.6 of the energy remaining at M_2 in some parts of the domain. At latitudes poleward of the CL, secondary waves can have frequencies outside of the internal wave band. Some studies found that while TRI secondary waves poleward of the CL are not progressive, these forced waves, or evanescent waves, can be extremely important (Korobov & Lamb, 2008, Richet et al., 2018). Energy can be transferred through evanescent waves (Richet et al., 2018) and the impact of forced waves on mixing can be even more important than the impact of freely propagating waves because trapped waves can accumulate energy more quickly (Korobov & Lamb, 2008). In contrast to our results, several numerical studies that examined simulations at mid-latitudes (Hibiya et al., 2002, Gerkema et al., 2006) did not find evidence suggesting that TRI is active at these latitudes. This could be due to the lack of frequency resolution around f and M_2-f, and the small signal at these latitudes.

In our simulations, TRI is extremely active equatorward of the CL, down to 15°N, showing severe degradation of the ITB. To our knowledge, there is only one numerical study (Nikurashin & Legg, 2011) and one observational study (Xie et al., 2011) which consider TRI secondary waves with frequency f away from the CL. Mooring data from the Hawaii Ocean Mixing Experiment (HOME) show strong energy at the inertial frequency, but this had previously been attributed to wind-generated inertial waves. Examination of previous analysis of HOME data from 22°N (Guiles, 2009, Chou et al., 2014)

suggests that energy at the inertial frequency is largest within the internal tide beam, and does not appear to be surface intensified. This evidence is consistent with TRI, but not with PSI.

At latitudes where TRI is active, the ITB becomes degraded to the point that interfacial wave amplitudes are greatly reduced or not observable. Simulations with the BB profile show the transfer of energy to higher harmonics and propagation of interfacial waves in the pycnocline for a range of latitudes, but the HOT experiments do not. A possible explanation for why high-frequency interfacial waves are found only in BB experiments is that the difference in the N-profile changes the phase speed of the high-frequency waves to the point where the ITB does not resonate with the high-frequency waves that would be trapped in the pycnocline (Grisouard & Staquet, 2010, Grisouard et al., 2011). The interfacial waves in the BB experiments might indicate local generation of internal solitary waves, but more analysis is needed to determine if that is the case. The BB experiments also show much more horizontal "ducting" of energy in the pycnocline, over a distance of more than 100 km, both at superharmonic and subharmonic frequencies. This could be due to the sharpness of the pycnocline in the BB profile relative to the HOT profile. The stratification profiles for BB and HOT are representative of conditions in the Bay of Biscay around 45°N and of Hawaii around 23°N, respectively, but they are smoothed profiles and small vertical scale features are not present. Small vertical scale variations as well as changes in the horizontal could potentially play significant roles in scattering and changing the ITB structure, but this subject is outside the scope of the present study. Including additional tidal constituents such as S_2, large-scale background flow, and three dimensional dynamics is likely to affect the growth of TRI, and can be the subject of future studies.

CHAPTER 4

Conclusion

The question of where and how internal tide energy is dissipated is among the most important problems in the field of physical oceanography today. Diapycnal mixing is widely assumed to play a crucial role in the maintenance of global stratification, on which the meridional overturning circulation depends. Internal tides appear to be the largest contributor of energy to mixing (MacKinnon et al., 2017), but it is not clear what happens to them after they are generated by the interaction of barotropic tides and topography. A number of processes are possible facilitators of the energy cascade of large-scale internal tides to smaller scale motions that are more likely to dissipate. Only observations can reveal what takes place in the ocean, but numerical simulations can guide the design of observational studies and the interpretation of data. The work described here extends the results of previous studies, puts forth new hypotheses, and suggests important questions for future studies to address.

Motivated by observations that show internal tide beams being severely disrupted after surface reflection, two-dimensional numerical simulations were designed to study linear and nonlinear processes that affect internal tide beams as they transit through varying stratification of the upper ocean. We wanted to know what happens to internal tide beams to understand how much of the $\sim$1 TW associated with the internal tide field is available for abyssal mixing. Two different models were used, the nonlinear and nonhdrostatic MITgcm and the linear and inviscid LIMM. We found that

even in the linear regime, beam scattering due to internal reflection and refraction can substantially change the beam's vertical structure. When the beam encounters changing stratification, it can be partially reflected and transmitted, resulting in the splitting of beams and decrease in the energy density of individual beams. Additionally, due to refraction and multiple reflections, beam energy can be horizontally ducted in the pycnocline and even in the mixed layer. The partial vertical trapping of internal tide energy in the pycnocline can facilitate the generation of internal solitary waves, a nonlinear and nonhydrostatic process (Gerkema, 2001).

Nonlinear and nonhydrostatic interfacial waves were generated using the Bay of Biscay stratification for a range of latitudes, but not when using the HOT stratification profile. We found that triadic resonant interactions (TRI) were a much more important process for both sets of experiments, extracting large amounts of energy from the M_2 beam once it had enough time to develop. For the Bay of Biscay experiments, the weakening of the beam due to TRI interfered with the generation of interfacial waves. TRI appeared to be active over a range of latitudes, both equatorward and poleward of the critical latitude (29°). Sub-M_2 kinetic energy reached more than 10% of what remained at M_2 for all latitudes from 15°N to 60°N. At the critical latitude, kinetic energy of secondary waves can be more than three times the kinetic energy remaining at the forcing frequency. Secondary waves can have frequencies of f and M_2-f, even when the latter is sub-inertial (poleward of the critical latitude).

The work on beam scattering from Chapter 2 highlights the importance of having adequate vertical resolution in simulations. Internal tide beams scatter when they encounter steep stratification changes, likely including the small vertical scale features in $N(z)$ that are present in many observational profiles. Experiments using single cast stratification profiles from Hawaii (2 m vertical resolution) show that small amplitude and vertical scale variations can also lead to splitting and spreading of beam energy. Exactly what resolution is needed to accurately describe beam scattering is beyond the scope of this study, but what we do know is that models which do not resolve small vertical scale changes in the stratification are missing fundamental aspects of internal tide beam propagation in the upper ocean. A related issue is the appearance of spurious scattering and

defocusing of the beam due to insufficient resolution ($dz > 20$ m). This is important since the vertical resolution of three-dimensional models is often lower than $dz = 20$ m. For example, the model in Carter et al. (2008) has 61 uniform sigma levels, which means dz is less than 20 m only when the water depth is less than 1220 m, and the transit of an internal tide beam through the pycnocline often occurs when the water depth is greater than 1220 m.

The nonlinear experiments discussed in Chapter 3 show that TRI can severely disrupt internal tides beams over a larger range of latitudes than what is commonly thought. This could mean that TRI is more important than previously thought, because if TRI/PSI (parametric subharmonic instability) is only important for a narrow band of latitudes around 29°, then it is not likely to have a large impact on global mixing. However, if TRI can actually transfer energy to f and M_2-f, especially when M_2-f is sub-inertial, then it could be important over a much wider physical extent than just around 29°. Some studies find that the non-progressive sub-inertial waves can be extremely important for mixing because trapped waves can accumulate energy more quickly (Korobov & Lamb, 2008, Richet et al., 2018). Guiles (2009) found evidence of sub-inertial motions at M_2-f poleward of 29°, and interestingly their rotation is cyclonic, in contrast to what is expected of internal waves. It would be interesting to compare our modeling results with these observations.

It is worth noting that there are different models being discussed for how the global stratification is maintained. There is general consensus that diapycnal mixing is caused by the breaking of internal waves and leads to upwelling of the densest water in the ocean (Munk, 1966, Munk & Wunsch, 1998, St. Laurent & Garrett, 2002, Vic et al., 2019). However, Ferrari et al. (2016) propose that because diapycnal diffusivity generally increases with depth, mixing actually leads to a net sinking of abyssal waters in the interior. Upwelling is instead confined to boundary layers near the seafloor where there can be more mixing with a lighter water above than with the denser water below. It has also been suggested that diapycnal mixing may not be required and wind-driven upwelling in the Antarctic Circumpolar Current is able to support the observed overturning rate of approximately 30×10^6 m^{3}s^{-1} (Toggweiler & Samuels, 1998). Another possibility is that dense water sinks at high latitudes and returns back to the surface through a combination of mixing in the lower 2 km of the ocean and

an "uplift" process powered by strong winds around Antarctica for water in the upper 2 km (Ferrari, 2014). Importantly, most of these models require some internal tide energy to penetrate well below the pycnocline. An improved understanding of internal tide energetics could better constrain the feasibility of the various candidates.

While the work presented here has important implications, there are many limitations which need to be addressed before considering using these results to design a field campaign. In the scattering study using LIMM, energy can not be transferred between vertical modes or dissipated. Both are likely to be important in the evolution of internal tide beams in the upper ocean. The MITgcm experiments include viscosity terms, but these are adjusted mainly for numerical stability and are not necessarily representative of realistic values. Another very important limitation is the inclusion of only the M_2 constituent in the forcing. Preliminary experiments including the solar semi-diurnal S_2 constituent show that the spring neap cycle has a large impact on the amplitude of secondary waves and the timescale over which TRI becomes important. Including sub-inertial background flows and three-dimensional effects, especially due to realistic topography, will likely influence the results as well. In spite of these many limitations, the present work offers important insights and outlines many accessible and productive paths for future researchers.

Bibliography

Akylas, T., Grimshaw, R. H., Clarke, S. R., & Tabaei, A. (2007). Reflecting tidal wave beams and local generation of solitary waves in the ocean thermocline. *Journal of Fluid Mechanics*, 593, 297–313.

Alford, M. H., MacKinnon, J. A., Zhao, Z., Pinkel, R., Klymak, J., & Peacock, T. (2007). Internal waves across the pacific. *Geophys. Res. Lett.*, 34, L24601.

Althaus, A. M., Kunze, E., & Sanford, T. B. (2003). Internal tide radiation from mendocino escarpment. *Journal of Physical Oceanography*, 33(7), 1510–1527.

Ansong, J. K., Arbic, B. K., Simmons, H. L., Alford, M. H., Buijsman, M. C., Timko, P. G., Richman, J. G., Shriver, J. F., & Wallcraft, A. J. (2018). Geographical distribution of diurnal and semidiurnal parametric subharmonic instability in a global ocean circulation model. *Journal of Physical Oceanography*, 48(6), 1409–1431.

Apel, J. R. (2002). Oceanic internal waves and solitons. *An atlas of oceanic internal solitary waves*, (pp. 1–40).

Cai, S., Xie, J., & He, J. (2012). An overview of internal solitary waves in the south china sea. *Surveys in Geophysics*, 33(5), 927–943.

Carter, G. S. & Gregg, M. C. (2006). Persistent near-diurnal internal waves observed above a site of m 2 barotropic-to-baroclinic conversion. *Journal of physical oceanography*, 36(6), 1136–1147.

Carter, G. S., Gregg, M. C., & Lien, R.-C. (2005). Internal waves, solitary-like waves, and mixing on the monterey bay shelf. *Continental Shelf Research*, 25(12-13), 1499–1520.

Carter, G. S., Merrifield, M. A., Becker, J. M., Katsumata, K., Gregg, M. C., Luther, D. S., Levine, M. D., Boyd, T. J., & Firing, Y. L. (2008). Energetics of M2 barotropic-to-baroclinic tidal conversion at the Hawaiian islands. *J. Phys. Oceanogr.*, 38, 2205–2223.

Chou, S. (2013). An empirical investigation of energy transfer from the m2 tide to m2 subharmonic wave motions in the kauai channel. Master's thesis.

Chou, S. H., Luther, D. S., Guiles, M. D., Carter, G. S., & Decloedt, T. (2014). An empirical investigation of nonlinear energy transfer from the m2 internal tide to diurnal wave motions in the kauai channel, hawaii. *Geophysical Research Letters*, 41(2), 505–512.

Cole, S., Rudnick, D. L., Hodges, B. A., & Martin, J. P. (2009). Observations of tidal internal wave beams at Kauai Channel, Hawaii. *J. Phys. Oceanogr.*, 39(2), 421–436.

Dauxois, T., Joubaud, S., Odier, P., & Venaille, A. (2018). Instabilities of internal gravity wave beams. *Annual Review of Fluid Mechanics*, 50, 131–156.

Dong, J., Robertson, R., Dong, C., Hartlipp, P. S., Zhou, T., Shao, Z., Lin, W., Zhou, M., & Chen, J. (2019). Impacts of mesoscale currents on the diurnal critical latitude dependence of internal tides: A numerical experiment based on barcoo seamount. *Journal of Geophysical Research: Oceans*.

Dushaw, B. D., Howe, B. M., Cornuelle, B. D., Worcester, P. F., & Luther, D. S. (1995). Barotropic and baroclinic tides in the central north pacific ocean determined from long-range reciprocal acoustic transmissions. *J. Phys. Oceanogr.*, 25, 631–647.

Egbert, G. D. & Ray, R. D. (2000). Significant dissipation of tidal energy in the deep ocean inferred from satellite altimeter data. *Nature*, 405, 775–778.

Egbert, G. D. & Ray, R. D. (2001). Estimates of M2 tidal energy dissipation from TOPEX/Poseidon altimeter data. *J. Geophys. Res.*, 106, 22475–22502.

Ferrari, R. (2014). Oceanography: What goes down must come up. *Nature*, 513(7517), 179–180.

Ferrari, R., Mashayek, A., McDougall, T. J., Nikurashin, M., & Campin, J.-M. (2016). Turning ocean mixing upside down. *Journal of Physical Oceanography*, 46(7), 2239–2261.

Ferrari, R. & Wunsch, C. (2009). Ocean circulation kinetic energy: Reservoirs, sources, and sinks. *Annu. Rev. Fluid Mech.*, 41, 253–282.

Furuichi, N., Hibiya, T., & Niwa, Y. (2005). Bispectral analysis of energy transfer within the two-dimensional oceanic internal wave field. *J. Phys. Oceanogr.*, 35, 2104–2109.

Garrett, C. & Kunze, E. (2007). Internal tide generation in the deep ocean. *Annu. Rev. Fluid Mech.*, 39, 57–87.

Gayen, B. & Sarkar, S. (2013). Degradation of an internal wave beam by parametric subharmonic instability in an upper ocean pycnocline. *Journal of Geophysical Research: Oceans*, 118(9), 4689–4698.

Gayen, B. & Sarkar, S. (2014). Psi to turbulence during internal wave beam refraction through the upper ocean pycnocline. *Geophysical Research Letters*, 41(24), 8953–8960.

Gerkema, T. (2001). Internal and interfacial tides: beam scattering and local generation of solitary waves. *Journal of Marine Research*, 59(2), 227–255.

Gerkema, T. & Shrira, V. I. (2005). Near-inertial waves in the ocean: beyond the 'traditional approximation'. *Journal of Fluid Mechanics*, 529, 195–219.

Gerkema, T., Staquet, C., & Bouruet-Aubertot, P. (2006). Decay of semi-diurnal internal-tide beams due to subharmonic resonance. *Geophys. Res. Lett*, 33, L08604.

Gerkema, T. & van Haren, H. (2012). Absence of internal tidal beams due to non-uniform stratification. *Journal of sea research*, 74, 2–7.

Gill, A. E. (1982). *Atmosphere-Ocean Dynamics*, volume 30. Academic Pr.

Gregg, M. (1987). Diapycnal mixing in the thermocline: A review. *Journal of Geophysical Research: Oceans*, 92(C5), 5249–5286.

Grisouard, N. & Staquet, C. (2010). Numerical simulations of the local generation of internal solitary waves in the bay of biscay. *Nonlinear Processes in Geophysics*, 17(5), 575–584.

Grisouard, N., Staquet, C., & Gerkema, T. (2011). Generation of internal solitary waves in a pycnocline by an internal wave beam: a numerical study. *Journal of Fluid Mechanics*, 676, 491–513.

Guiles, M. (2009). *Energy Redistribution through Tidal and Inertial Wave Interaction*. PhD thesis, University of Hawaii, Manoa.

Hazewinkel, J. & Winters, K. B. (2011). PSI of the internal tide on a beta-plane: Flux divergence and near-inertial wave propagation. *J. Phys. Oceanogr.*, 41, 1673–1682.

Hibiya, T. & Nagasawa, M. (2004). Latitudinal dependence of diapycnal diffusivity in the thermocline estimated using a finescale parameterization. *Geophys. Res. Lett.*, 31, LO1301.

Hibiya, T., Nagasawa, M., & Niwa, Y. (2002). Nonlinear transfer within the oceanic internal wave spectrum at mid and high latitudes. *J. Geophys. Res.*, 107(C11), 3207.

Jackson, C. (2007). Internal wave detection using the moderate resolution imaging spectroradiometer (modis). *Journal of Geophysical Research: Oceans*, 112(C11).

Jackson, C. R. (2009). An empirical model for estimating the geographic location of nonlinear internal solitary waves. *Journal of Atmospheric and Oceanic Technology*, 26(10), 2243–2255.

Jackson, C. R. & Apel, J. (2004). An atlas of internal solitary-like waves and their properties. *Contract*, 14(03-C), 0176.

Johnston, T. M. S., Merrifield, M., & Holloway, P. (2003). Internal tide scattering at the line islands ridge. *J. Geophys. Res.*, 108(C11), 3365.

Johnston, T. M. S. & Merrifield, M. A. (2003). Internal tide scattering at seamounts, ridges, and islands. *J. Geophys. Res.*, 108(C6), 3180.

Johnston, T. M. S., Rudnick, D. L., Carter, G. S., Todd, R. E., & Cole, S. T. (2011). Internal tidal beams and mixing near monterey bay. *Journal of Geophysical Research: Oceans*, 116(C3).

Karl, D. M. & Lukas, R. (1996). The hawaii ocean time-series (hot) program: Background, rationale and field implementation. *Deep Sea Research Part II: Topical Studies in Oceanography*, 43(2-3), 129–156.

Korobov, A. S. & Lamb, K. G. (2008). Interharmonics in internal gravity waves generated by tide-topography interaction. *J. Fluid Mech.*, 611, 61–95.

Koudella, C. R. & Staquet, C. (2006). Instability mechanisms of a two-dimensional progressive internal gravity wave. *J. Fluid Mech.*, 548, 165–196.

Large, W. G., McWilliams, J. C., & Doney, S. C. (1994). Oceanic vertical mixing: A review and a model with a nonlocal boundary layer parameterization. *Reviews of Geophysics*, 32(4), 363–403.

Leaman, K. & Sanford, T. B. (1975). Vertical energy propagation of inertial waves: a vector spectral analysis of velocity profiles. *J. Geophys. Res.*, 80(15), 1975–1978.

Ledwell, J. R., Watson, A. J., & Law, C. S. (1993). Evidence for slow mixing across the pycnocline from an open-ocean tracer-release experiment. *Nature*, 364(6439), 701–703.

Lee, C. M., Sanford, T. B., Kunze, E., Nash, J. D., Merrifield, M. A., & Holloway, P. E. (2006). Internal tides and turbulence along the 3000-m isobath of the Hawaiian Ridge. *J. Phys. Oceanogr.*, 36(6), 1165–1183.

Liao, G., Yuan, Y., Yang, C., Chen, H., Wang, H., & Huang, W. (2012). Current observations of internal tides and parametric subharmonic instability in luzon strait. *Atmosphere-Ocean*, (pp. 1–18).

Lien, R.-C., Henyey, F., Ma, B., & Yang, Y. J. (2014). Large-amplitude internal solitary waves observed in the northern south china sea: properties and energetics. *Journal of Physical Oceanography*, 44(4), 1095–1115.

MacKinnon, J. A., Alford, M. H., Pinkel, R., Klymak, J., & Zhao, Z. (2013a). The Latitudinal Dependence of Shear and Mixing in the Pacific Transiting the Critical Latitude for PSI. *J. Phys. Oceanogr.*, 43, 3–16.

MacKinnon, J. A., Alford, M. H., Sun, O., Pinkel, R., Zhao, Z., & Klymak, J. (2013b). Parametric Subharmonic Instability of the Internal Tide at 29N. *J. Phys. Oceanogr.*, 43, 17–28.

MacKinnon, J. A. & Winters, K. B. (2005). Subtropical catastrophe: Significant loss of low-mode tidal energy at 28.9 degrees. *Geophys. Res. Lett.*, 32, L15605.

MacKinnon, J. A., Zhao, Z., Whalen, C. B., Waterhouse, A. F., Trossman, D. S., Sun, O. M., St. Laurent, L. C., Simmons, H. L., Polzin, K., Pinkel, R., et al. (2017). Climate process team on internal wave–driven ocean mixing. *Bulletin of the American Meteorological Society*, 98(11), 2429–2454.

Marshall, J., Adcroft, A., Hill, C., Perelman, L., & Heisey, C. (1997). A finite-volume, incompressible Navier Stokes model for studies of the ocean on parallel computers. *J. Geophys. Res.*, 102(C3), 5753–5766.

Martin, J. P., Rudnick, D. L., & Pinkel, R. (2006). Spatially broad observations of internal waves in the upper ocean at the Hawaiian Ridge. *J. Phys. Oceanogr.*, 36, 1085–1103.

Mathur, M. & Peacock, T. (2009). Internal wave beam propagation in non-uniform stratifications. *Journal of Fluid Mechanics*, 639, 133–152.

McComas, C. H. & Bretherton, F. P. (1977). Resonant interaction of oceanic internal waves. *J. Geophys. Res.*, 82, 1397–1412.

Mercier, M. J., Mathur, M., Gostiaux, L., Gerkema, T., Magalhães, J. M., Da Silva, J. C., & Dauxois, T. (2012). Soliton generation by internal tidal beams impinging on a pycnocline: laboratory experiments. *Journal of Fluid Mechanics*, 704, 37–60.

Müller, P., Holloway, G., Henyey, F., & Pomphrey, N. (1986). Nonlinear interactions among internal gravity waves. *Rev. Geophys*, 24(3), 493–536.

Munk, W. H. (1966). Abyssal recipes. In *Deep Sea Research and Oceanographic Abstracts*, volume 13 (pp. 707–730).: Citeseer.

Munk, W. H. & Wunsch, C. (1998). Abyssal recipes II: Energetics of tidal and wind mixing. *Deep Sea Research Part I*, 45, 1977–2010.

New, A. & Da Silva, J. (2002). Remote-sensing evidence for the local generation of internal soliton packets in the central bay of biscay. *Deep Sea Research Part I: Oceanographic Research Papers*, 49(5), 915–934.

New, A. & Pingree, R. (1990). Large-amplitude internal soliton packets in the central bay of biscay. *Deep Sea Research Part A. Oceanographic Research Papers*, 37(3), 513–524.

Nikurashin, M. & Legg, S. (2011). A mechanism for local dissipation of internal tides generated at rough topography. *J. Phys. Oceanogr.*, 41, 378–395.

Pearson-Potts, K. (2019). *DEEP NEAR-INERTIAL WAVES IN THE SAMOAN PASSAGE*. PhD thesis, UNIVERSITY OF HAWAI 'I AT MANOA.

Pickering, A. & Alford, M. H. (2012). Velocity Structure of Internal Tide Beams Emanating from Kaena Ridge, Hawaii. *J. Phys. Oceanogr.*, 42, 1039–1044.

Pinkel, R. & Rudnick, D. (2006). Hawaii ocean mixing experiment (home). *Journal of physical oceanography*, 36(6).

Polzin, K. (2004). A heuristic description of internal wave dynamics. *Journal of physical oceanography*, 34(1), 214–230.

Rainville, L., Johnston, T. M. S., Carter, G. S., Merrifield, M. A., Pinkel, R., Worcester, P. F., & Dushaw, B. D. (2010). Interference pattern and propagation of the M2 internal tide south of the Hawaiian Ridge. *J. Phys. Oceanogr.*, 40, 311–325.

Rainville, L. & Pinkel, R. (2006a). Baroclinic energy flux at the Hawaiian Ridge: Observations from the R/P FLIP. *J. Phys. Oceanogr.*, 36, 1104–1122.

Ray, R. D. & Mitchum, G. T. (1996). Surface manifestation of internal tides generated near Hawaii. *Geophys. Res. Lett.*, 23, 2101–2104.

Richet, O., Chomaz, J.-M., & Muller, C. (2018). Internal tide dissipation at topography: triadic resonant instability equatorward and evanescent waves poleward of the critical latitude. *Journal of Geophysical Research: Oceans*, 123(9), 6136–6155.

Richet, O., Muller, C., & Chomaz, J.-M. (2017). Impact of a mean current on the internal tide energy dissipation at the critical latitude. *Journal of Physical Oceanography*, 47(6), 1457–1472.

St. Laurent, L. & Garrett, C. (2002). The role of internal tides in mixing the deep ocean. *J. Phys. Oceanogr.*, 32, 2882–2899.

Staquet, C. & Sommeria, J. (2002). Internal Gravity Waves: From Instabilities to Turbulence. *Annu. Rev. Fluid Mech.*, 34, 559–593.

Sun, O. M. & Pinkel, R. (2013). Subharmonic energy transfer from the semidiurnal internal tide to near-diurnal motions over Kaena Ridge, Hawaii. *J. Phys. Oceanogr.*, (pp. in press).

Sutherland, B. R. (2010). *Internal gravity waves*. Cambridge university press.

Toggweiler, J. & Samuels, B. (1998). On the ocean's large-scale circulation near the limit of no vertical mixing. *Journal of Physical Oceanography*, 28(9), 1832–1852.

Vallis, G. K. (2006). *Atmospheric and Oceanic Fluid Dynamics*. Cambridge, U.K.: Cambridge University Press.

Vic, C., Garabato, A. C. N., Green, J. M., Waterhouse, A. F., Zhao, Z., Mélet, A., De Lavergne, C., Buijsman, M. C., & Stephenson, G. R. (2019). Deep-ocean mixing driven by small-scale internal tides. *Nature communications*, 10(1), 1–9.

Waterhouse, A. F., Kelly, S. M., Zhao, Z., MacKinnon, J. A., Nash, J. D., Simmons, H., Brahznikov, D., Rainville, L., Alford, M., & Pinkel, R. (2018). Observations of the tasman sea internal tide beam. *Journal of Physical Oceanography*, 48(6), 1283–1297.

Waterhouse, A. F., MacKinnon, J. A., Nash, J. D., Alford, M. H., Kunze, E., Simmons, H. L., Polzin, K. L., St. Laurent, L. C., Sun, O. M., Pinkel, R., et al. (2014). Global patterns of diapycnal mixing from measurements of the turbulent dissipation rate. *Journal of Physical Oceanography*, 44(7), 1854–1872.

Wunsch, C. & Ferrari, R. (2004). Vertical mixing, energy, and the general circulation of the ocean. *J. Fluid Mech.*, 36, 281–314.

Xie, X., Shang, X., van Haren, H., & Chen, G. (2013a). Observations of enhanced nonlinear instability in the surface reflection of internal tides. *Geophysical Research Letters*, 40(8), 1580–1586.

Xie, X. H., Cuypers, Y., Bouruet-Aubertot, P., Ferron, B., Pichon, A., Lourenço, A., & Cortes, N. (2013b). Large-amplitude internal tides, solitary waves, and turbulence in the central bay of biscay. *Geophysical Research Letters*, 40(11), 2748–2754.

Xie, X. H., Shang, X. D., van Haren, H., Chen, G. Y., & Zhang, Y. Z. (2011). Observations of parametric subharmonic instability-induced near-inertial waves equatorward of the critical diurnal latitude. *Geophys. Res. Lett.*, 38(5), L05603.

Yang, W., Hibiya, T., Tanaka, Y., Zhao, L., & Wei, H. (2018). Modification of parametric subharmonic instability in the presence of background geostrophic currents. *Geophysical Research Letters*, 45(23), 12–957.

Zaron, E. D. & Egbert, G. D. (2014). Time-variable refraction of the internal tide at the hawaiian ridge. *Journal of physical oceanography*, 44(2), 538–557.

Zhao, Z., Alford, M. H., Girton, J. B., Rainville, L., & Simmons, H. L. (2016). Global observations of open-ocean mode-1 m2 internal tides. *Journal of Physical Oceanography*, 46(6), 1657–1684.